The Thesis Committee for Natchanan Doungkaew
Certifies that this is the approved version of the following thesis:

Fracture Aperture Profiles as Indicators of Fracture Growth Environments: An Integrated Study of Fracture Aperture Growth in the Campito Formation of Eastern California

APPROVED BY
SUPERVISING COMMITTEE:

Supervisor:

Peter Eichhubl

Whitney Behr

William Fisher

Fracture Aperture Profiles as Indicators of Fracture Growth Environments: An Integrated Study of Fracture Aperture Growth in the Campito Formation of Eastern California

by

Natchanan Doungkaew, B.A.

Thesis

Presented to the Faculty of the Graduate School of

The University of Texas at Austin

in Partial Fulfillment

of the Requirements

for the Degree of

Master of Science in Geological Sciences

The University of Texas at Austin

December 2016

Dedication

This thesis is dedicated to my mom. The memories of her always make me smile no matter what is happening in my life. I also want to dedicate it to Ryan J. Marchese, the beloved software engineer who edited this whole thesis.

Acknowledgements

My utmost gratitude goes out to my advisor, Dr. Peter Eichhubl, for his patience, guidance and support. His editorial comments, guidance, and suggestions have significantly improved this research. The knowledge he passed throughout the process of completing this research has shaped me to become a more competent geologist and researcher. I would like to thank my thesis committee members, Dr. William Fisher and Dr. Whitney Behr, for their feedback and time given to review this work.

This work would not have been completed without the help of students and staff at the Fracture Research and Application Consortium. I would like to acknowledge Owen Callahan, my field assistant for his support, help, and valuable suggestions in the White Mountains. I would not have been able to record close to 100 fracture aperture profiles and all hand samples without his aid. I thank Dr. Andras Fall who taught me about fluid inclusion microthermometry, how to prepare thin sections, and how to apply the cycling technique. I'm grateful for the help from Sara Elliot on the SEM-CL analysis. Even though the analysis did not work on my samples, I had an opportunity to learn about how to operate the machine and about the analysis from her. During the process of writing the discussion part of this work, Dr. Zhiqiang Fan had been a great help and always gave me guidance on how to tackle the problems and gave comments on my ideas.

All of the drafts of the thesis and manuscripts have been copy edited by Ryan Marchese before I passed them on to my advisor. I would like to thank him for the long hours of reading and editing this long document, and for the advice, support, and food. I would like to thank all of my friends for their companionship and love. Last, but not least, I would like to thank my family for their endless encouragement.

This project is supported by a Royal Thai Government's Development and Promotion of Science and Technology Talents Project (DPST) scholarship and the GSA Graduate Student Research Grant. Field expenses are supported by the Jackson School of Geosciences' Ronald K. DeFord Field Scholarship Fund and Fracture Research and Application Consortium

.

Abstract

Fracture Aperture Profiles as Indicators of Fracture Growth Environments: An Integrated Study of Fracture Aperture Growth in the Campito Formation of Eastern California

Natchanan Doungkaew, M.S. Geo. Sci.

The University of Texas at Austin, 2016

Supervisor: Peter Eichhubl

Processes of fracture formation control flow of fluid in the subsurface and the mechanical properties of the brittle crust. I investigate whether fracture aperture profiles describing the opening displacement along their height or length reflect fracture growth conditions and mechanisms. I hypothesize that aperture profiles of fractures growing under different environments and by different mechanisms have different ellipticity. I measured fracture profiles for quartz cemented opening-mode fractures in low-grade metamorphic sandstone of the Campito Formation, eastern California, and quantified their ellipticity using curve fitting methods based on the Lamé function. I compare the Lamé parameter n against structural and inferred environmental parameters, including fracture orientation, fracture tip characteristics, locations of fracture tips relative to layer boundaries, texture of fracture cements, and temperature during fracture growth as

determined through fluid inclusion homogenization temperatures. Lamé n values range from 0.72 to 3.20, with the majority falling between 1 and 1.5. Fracture with $n < 2$ correlate with higher fluid inclusion homogenization temperatures between 270°C and 315°C, and are preferentially filled with blocky quartz cement. Fractures with fluid inclusion temperatures in the range of 150°C and 250°C have $n\sim 2$ and preferentially contain crack-seal quartz cement. I observe no correlation between n and fracture orientation, and aperture/length ratio, although fractures with wide apertures have $n<2$.

To explain fractures with $n<2$ we propose a fracture growth mechanism consisting of elastic opening increments followed by stages of stress dissipation in the fracture tip regions. Kinematic models suggest that rapid length or height growth with slow aperture growth results in fracture aperture profiles with $n\sim1$. Fracture aperture profiles with $n>2$ require opening increments with blunt tips and slow length or height growth relative to aperture growth. Our model is consistent with faster length growth resulting from reduced fracture toughness with increasing temperature, leading to low n at higher temperatures. The absence of crack-seal cement in fractures with low n may relate to overall fast fracture growth at higher temperatures, with aperture growth exceeding rates of synkinematic crack-seal quartz cementation. Fractures with $n>2$ require tip blunting that I attribute to enhanced solution-precipitation creep by stress concentration at the fracture tip.

Table of Contents

List of Tables

List of Figures

CHAPTER 1: INTRODUCTION

As an abundant structure in the Earth, fractures and faults composed of fractures control mechanical properties of the brittle crust and fluid flow in the subsurface (National Research Council, 1996). In this study, we focus on opening-mode fractures, also referred to as Mode I, extension, or tension fractures. The opening displacement of this type of fracture is perpendicular to the fracture plane. Opening mode fractures can form isolated structures, clusters, or systems of connected fractures. Various studies have quantified aperture, length, and spatial arrangement of opening-mode fractures (Snow, 1970; Vermilye and Scholz, 1995; Olson, 2003; Olson, 2007; Gomez, 2007; Sakaguchi et al., 2008). Aperture refers to the maximum width of a fracture. Aperture size and size distribution have been quantified in several studies (Bonnet et al., 2001; Gale et al., 2007; Hooker et al., 2009; Hooker et al., 2013) because they govern flow of fluids in the subsurface. Specifically, a volumetric flux of fluid that flows through an open fracture is a function of the cube of the aperture of the open fracture (Walsh, 1981; Tsang and Witherspoon, 1981; Klimczak et al., 2010). Among the various studies on aperture size and size distribution of sets of fractures, few studies have investigated the aperture distribution or aperture profile along single fractures (Pollard and Segall,1987; Gudmundsson, 1987; Vermilye and Scholz,1995; Gudmundsson et al.,2012).

An aperture profile is a plot of the width or opening-displacement of a fracture in two dimensions along a fracture length or height transect. According to linear elastic fracture mechanics, an aperture profile of a fracture in a homogeneous, linearly elastic and isotropic material subject to a constant fluid pressure and a constant external driving stress is elliptical in shape (Sneddon, 1946; Geertsma and Klerk, 1969; Engelder et al., 1993; Gudmundsson, 2011). Specifically, since displacement along the length or height of a fracture is a linear function of

stress, and stress along the length or height of a fracture follows an elliptical function (Sneddon, 1946; Irwin, 1957), the displacement of the fracture walls or the aperture of the fracture is also an elliptical function, and can be described by an equation:

$$u(x) = \pm\Delta\sigma_I \frac{(1-\nu)}{\mu}\sqrt{a^2 - x^2} + \Delta\sigma_{II}\frac{(1-2\nu)x}{2\mu}$$

(Equation 8.34 in Pollard and Segall, 1987), where u(x) is the displacement at position x along the length of fracture, $\Delta\sigma_I$ and $\Delta\sigma_{II}$ are the driving stress in mode I and mode II, respectively, a is half the fracture length or, for a vertical fracture, height, ν is Poisson's ratio, and μ is Young's modulus. The ± sign with the first term refers to the upper wall at $x_1 = 0^+$ and the lower wall at $x_1 = 0^-$. The linear elastic fracture mechanics section in Chapter 3 provides a detailed explanation of the above equation.

Multiple studies based on field observations and numerical models have shown that the shapes of aperture profiles are approximately elliptical. Pollard and Segall (1987) demonstrated that the shape of a dilation profile of a basaltic dike segment near Ship Rock can be adequately described by the elliptical displacement equation mentioned above. Gudmundsson (2011) similarly showed that displacements of many fractures along their length can be roughly described by an elliptical function. The author gave examples of elliptical aperture profiles along mineral-filled vein in gneiss in West Norway (p.389). Analytical solutions for fracture apertures affected by overpressure variations given by Gudmundsson et al. (2012) and Kusumoto et al. (2013) show that aperture profiles are elliptical when the pressure within a fracture is uniform.

However, deviations of aperture profiles of natural fractures from the theoretical elliptical shape were also reported in multiple studies. Pollard and Segall (1987) noticed the departures from a perfect ellipse of the aperture profiles of dikes and attributed these departures to the wall rock brecciation and erosion and elastic interaction with closely spaced neighboring dike

segments. Delaney and Pollard (1981) demonstrated that interaction between the tips of two parallel but offset and partially overlapping fractures causes the sides of the fractures closest to one another to show a deficit in opening displacement compared to isolated fractures leading to more tapered aperture profiles. The tip regions of two collinear closely spaced fractures, on the other hand, experience a slightly greater dilation compared to isolated fractures, resulting in relative blunting of tips. Studies of geometry of tectonic fractures on the Reykjanes Peninsula in southwest Iceland (Gudmundsson, 1987), and in West Norway Gudmundsson et al. (2012) showed variations in fracture aperture along fracture lengths that the authors attributed to variations of overpressure. Vermilye and Scholz (1995) presented aperture profiles of fractures from Culpeper Quarry and Florence Lake with linear tapers toward the fracture tips. They claimed the linearly tapered tips represent zones of inelastic deformation.

Various factors, including temperature, chemical reactions, material anisotropy across layer interfaces, and fluid pressure variation can control how fractures propagate (Atkinson, 1984; Atkinson and Meredith, 1989; Helgeson, and Aydin, 1991; Cooke and Underwood, 2001; Nara et al., 2006). Non elastic fracture growth can cause deviation of fracture shapes from those of elastic fractures. Eichhubl and Aydin (2003) and Eichhubl (2004) observed fractures with high aperture to length ratios in reactive combustion-metamorphic diagenetic environments, suggesting that inelastic fracture growth could occur due to solution mass transfer. A recent study on cemented fractures in deeply buried sandstone in East Texas has also identified non-linear fracture growth, in which a period of fast fracture growth in length relative to aperture growth is followed by a period of a slow propagation and faster aperture growth accommodated by solution-precipitation creep (Alzayer et al., 2015). Even though the previous studies demonstrated how various factors affect fracture shapes, aperture profiles were not measured in

these studies to verify if non-elastic fracture growth processes can result in non-elliptical fracture profiles.

In this study, I measured aperture profiles of cemented opening-mode fractures or veins in low-grade metamorphic silt- and sandstone of the Campito Formation, White Mountains, CA, to test if aperture profiles reflect fracture growth conditions and mechanisms. I hypothesize that aperture profiles of fractures growing in different environments and following different mechanisms will have a different degree of ellipticity as quantified by the Lamé parameter n. I applied a nonlinear least squares fitting method to find the best superellipse or Lamé curve that best fit each aperture profile. To quantify the ellipticity of aperture profiles, I compared the parameter n of the superellipse against structural and inferred environmental parameters that may control fracture growth. I determined relative ages of fractures based on their cross-cutting relationships observed in the field and in hand samples, and compared aperture profile ellipticity of young and old fractures to investigate if structural evolution affected aperture profiles. I also investigated the effects of fracture interactions by comparing ellipticity of fractures with isolated tips, branching tips, and the tips that are located close to other fracture tips. To study the effect of material heterogeneity across layer interfaces on fracture shape, I compared aperture profiles of fractures with tips located at various distances from layer boundaries. In addition, I compared the ellipticity of aperture profiles of different fracture cement textural characteristics to investigate effects of opening kinematics on aperture profile. The curve fitting method also contains values of fracture half-height and maximum aperture which I used to investigate the correlation between the size and ellipticity of the fracture. Additionally, I conducted fluid inclusion microthermometry to relate temperature of fracture formation to fracture shape.

Chapter 2 provides the geologic background of the White-Inyo Mountains. Chapter 3 provides a background information on fracture mechanics including approaches of fracture initiation problems using the strength of material approach, the linear elastic fracture mechanics (LEFM) approach, the elastic plastic fracture mechanics (EPFM) approach, and the viscoelastic approach and their theoretical aperture profiles from the latter three approaches. Chapter 3 also provide a schematic map of fracture mechanisms and a deformation mechanisms map for quartz. Chapter 4 details the methods and procedures employed in this study. Chapter 5 is a self-contained journal-article-styled version of this thesis, which I plan to submit to the Journal of Structural Geology. I discuss the findings and propose conceptual models that demonstrate how fractures with different types of aperture profiles grow in Chapter 6. In Chapter 7, I present the summary of the results and conclusions.

TERMINOLOGY

The term rock fracture refers to any mechanical discontinuity in rock which the rock failed, creating two parallel free surfaces (Twiss and Moores, 2007). The two surfaces are referred to as fracture walls. Fractures in rocks have three basic characteristics: 1) the fracture walls meet at the fracture front or tip line, 2) the fracture walls are approximately planar, and 3) the relative displacement of originally adjacent points across the fracture is small compared to the length of the fracture (Pollard and Segall, 1987). In two dimensions, the point where fracture walls intersect is the fracture tip. The distance perpendicular to two fracture walls is the aperture, or the width, of the fracture. For vertical or near-vertical fractures, describing the majority of fractures in this study, the height is the long dimension of the fracture measured in the vertical direction, the length the long dimension in the horizontal distance (Figure 1.1).

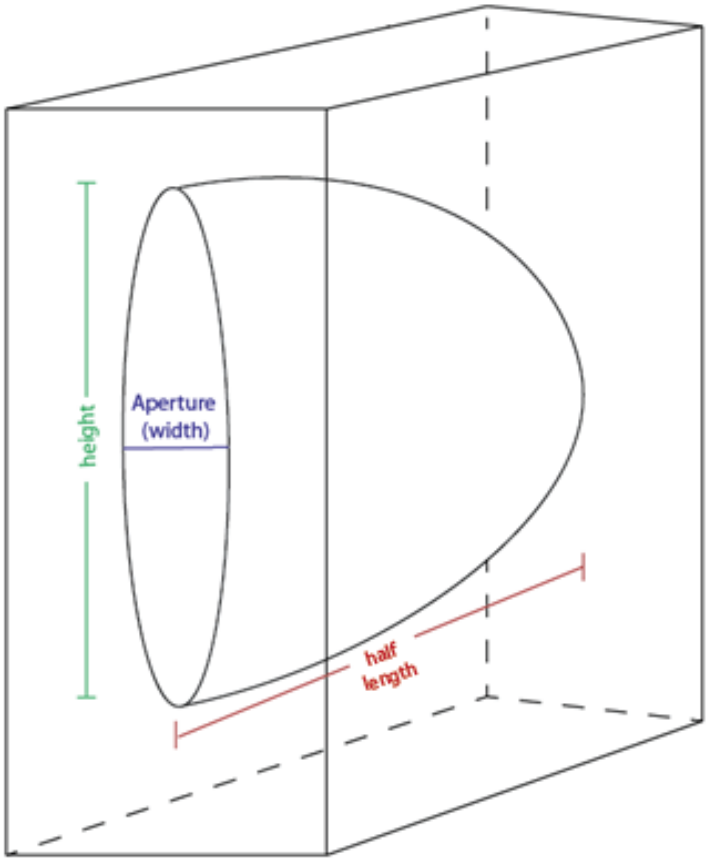

Figure 1.1: Aperture (width), half-length, and height of a fracture.

Fracture mechanics distinguishes three modes of loading based on geometry of fracture opening displacement relative to the orientation of the fracture and the fracture tip line (Sibson, 1997; Bons et al., 2012; Twiss and Moores, 2007):

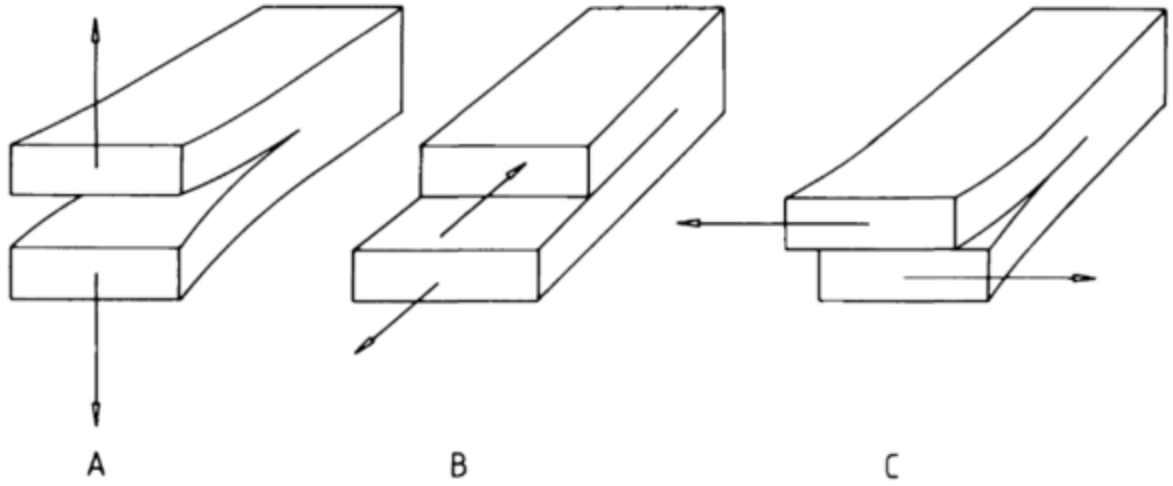

Figure 1.2: Three fundamental modes of fracture -- A: mode I, tensile or opening mode; B: mode II, in-plane shear or sliding mode; C: mode III, anti-plane shear or tearing mode (from Atkinson, 1987).

Mode I (tensile or opening mode): the displacement vector of the fracture is perpendicular to the fracture plane (Figure 1.2). Stresses applied on x, y and z surfaces are greater than zero ($\sigma_x \neq 0$, $\sigma_y \neq \sigma_z \neq 0$), while shear stress is not present ($\tau_{xy} = 0$) (Figure 1.3Figure 1.3).

Mode II (in-plane shear or sliding mode): the displacement vector of the fracture is parallel to the fracture plane and perpendicular to the tip line (Figure 1.2). Stresses are only applied on two of the axes, while shear stress is not equal to zero ($\tau_{xy} \neq 0$ and $\sigma_y = 0$).

Mode III (anti-plane shear or tearing mode): the displacement vector of the fracture is parallel to the fracture plane and to the tip line of the fracture (Figure 1.2). Shear stress is greater than zero in this case. ($\tau_{yz} \neq 0$, $\tau_{xy} = 0$ and $\sigma_y = 0$).

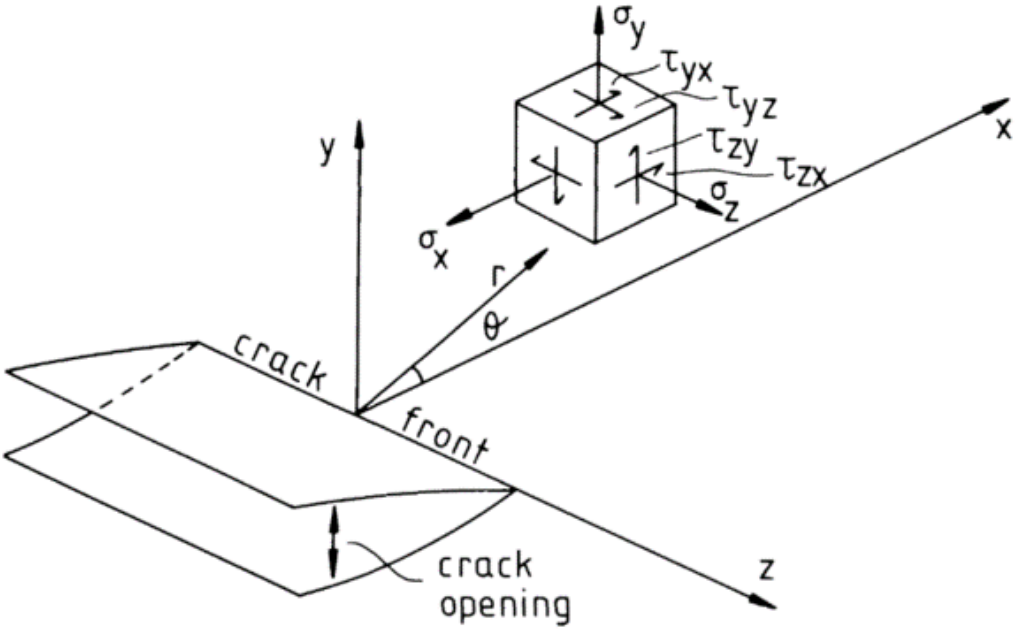

Figure 1.3: Mode I fracture in coordinate frames of analyses of linear elastic crack tip stress field. In this mode, stresses applied on x,y and z surfaces are greater than zero, while shear stress is not present ($\sigma_x \neq 0$, $\sigma_y \neq \sigma_z \neq 0$ and $\tau_{xy} = 0$) (modified from Atkinson,1987).

In this study, fractures are largely or completely filled with mineral cement and may thus be considered veins. Joint refers to barren fractures that are not filled with any cement. Uncemented fractures may change their aperture after they form, for instance during exhumation, and are thus not conducive for studies of fracture aperture distribution at the time of fracture formation. We thus selected cemented fractures or veins for this study.

CHAPTER 2: GEOLOGIC BACKGROUND

The White-Inyo Mountain Range lies along the eastern border of California and extends into Nevada (Figure 2.1). It represents the westernmost range of the Basin and Range physiographic province, and extends for 175 km from Montgomery Pass in the north to Malpais Mesa in the south (Nelson et al., 1991).

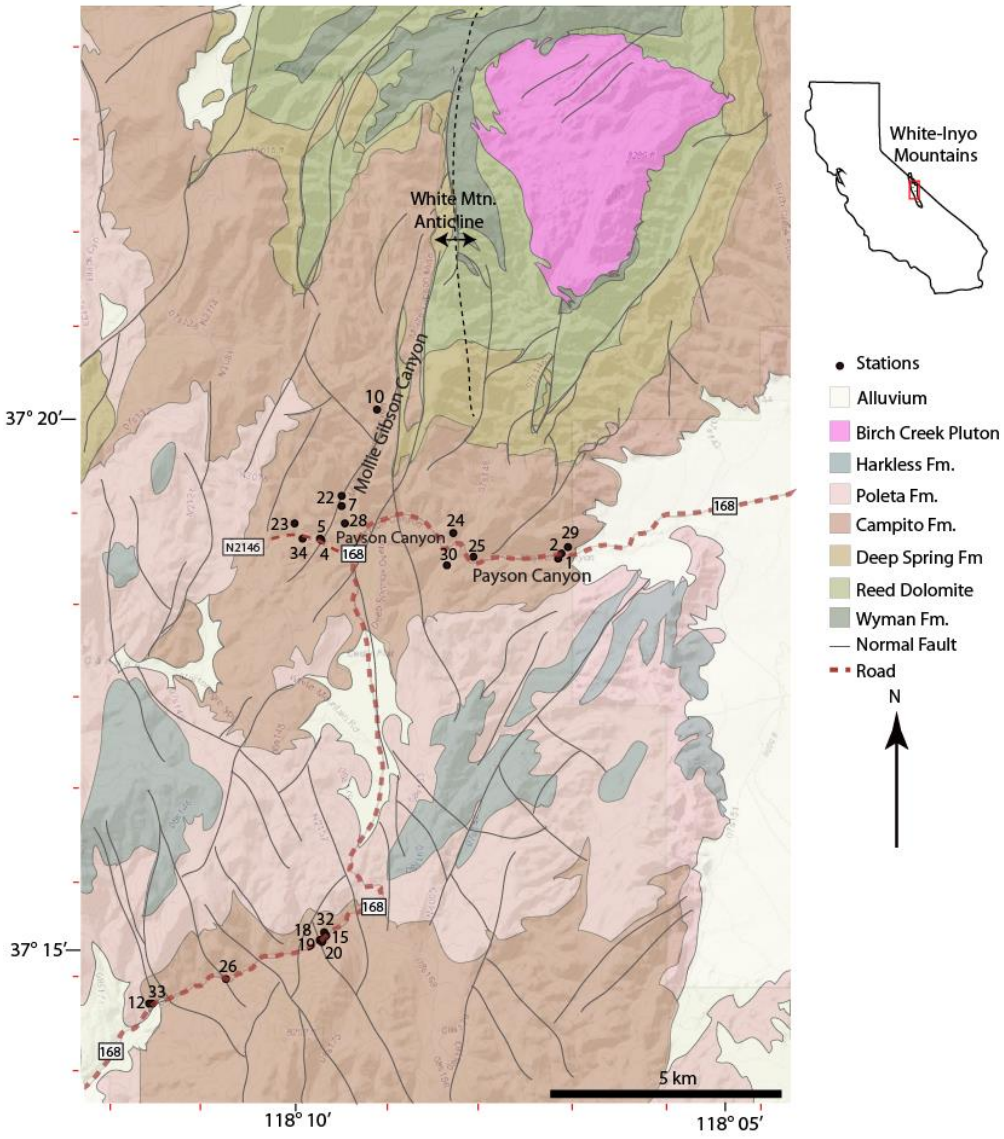

Figure 2.1: Locations of the field stations. The northern stations are closer to the White Mountain Anticline, while the southern stations are located along the CA-168 highway.

The age of the rock units in the White-Inyo Mountains range in age from late Precambrian to Holocene. From the Neoproterozoic Era to the end of the Devonian Period, westward-flowing streams deposited sediments in a marine basin called the Cordilleran miogeocline at the western edge of the North American continent (Nelson et al., 1991; Stevens et al., 1997; Barton, 2000) (Figure 2.2). The thickness of the sediment accumulated in the miogeocline from the upper Precambrian through Lower Jurassic exceeded 7 km in the White-Inyo region. The siltstone and metamorphosed sandstone of the Campito Formation were deposited on a shallow continental shelf (Nelson et al., 1991 and Moore and Fritsche, 1976) in a tidal environment.

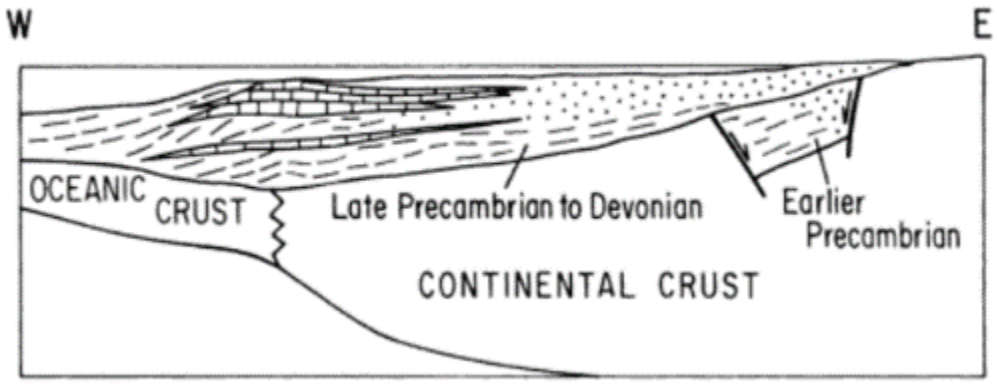

Figure 2.2: Schematic cross section of the western margin of North American plate during late Precambrian (700 Ma) to Devonian (345 Ma). Rocks formed in this interval resulted from sediment accumulation in the Cordilleran geosyncline. (From Nelson et al., 1991)

The central White-Inyo Range contains stratigraphic sections of upper Precambrian to middle Paleozoic rocks (Figure 2.3). The oldest rocks from the Precambrian Eon are the Wyman Formation, which comprises thin bedded brown to dark-gray argillite, fine-grained brown quartzitic sandstone and gray-brown siltstone. Lenticular gray-blue oolitic limestone, which is locally transformed to coarse-grained buff-gray dolomite, is also found in this formation (Nelson,

1966). Most fossils found are animal tracks and trails. It also contains the oldest trilobite faunas in the Americas (Nelson et al., 1991).

Overlying the Wyman Formation is the Reed Dolomite, with the two formations separated by an unconformity. The formation is comprised mostly of dolomite with a small percentage of fine-to-medium grained quartzite and calcareous sandstone (Nelson, 1966). The Reed Dolomite underlies the Deep Spring Formation. The lower member of the Deep Spring Formation includes Cambrian rocks that are similar to those of the Reed dolomite, while its upper member is comprised of gray to black quarzitic sandstone and siltstone overlain by massive gray fine-grained dolomite (Nelson, 1966). The upper member of the Reed Dolomite and the basal part of the Deep Spring Formation contain a small mollusk-like fossil called *Wyattia* (Nelson and Durham, 1966; Signor et al., 1987), which marks the beginning of the Paleozoic Era (Nelson and Durham, 1966).

The Campito Formation, which is the main focus of this study, overlies the Deep Spring Formation. The formation consists of the Andrews Mountain member and the Montenegro member. The older Andrew member comprises massively bedded, cross-stratified gray to black fine-grained quarzitic sandstone and interbedded gray siltstone and shale. Lowest Olenellid fauna fossils are found in the middle member. The Montenegro member contains gray shale and interbedded fine-grained quarzitic siltstone and quarzitic sandstone (Nelson, 1966).

Overlying the Campito Formation are the lower Cambrian Poleta and Harkless Formations. The older Poleta Formation is comprised mostly of limestone. The Harkless Formation is composed of brown platy silty shale with thin beds of fine-grained quartzite. The formation is locally transformed to siliceous hornfels near Beer Creek and Joshua Flat plutons (Nelson, 1966).

The succession from the upper Wyman to the Poleta Formation represents rocks that deposited in tidal environments and carbonate bank and shoal environments (Nelson et al., 1991; Stevens and Greene, 1999). The terrigenous strata, which include shale, siltstone, and quartzite, were deposited on a shallow continental. The strata also contain abundant shallow water indicators such as sedimentary rocks with crossbeds, current and wave ripple marks, mud cracks, and highly bioturbated beds. (Nelson et al., 1991; Moore and Fritsche, 1976).

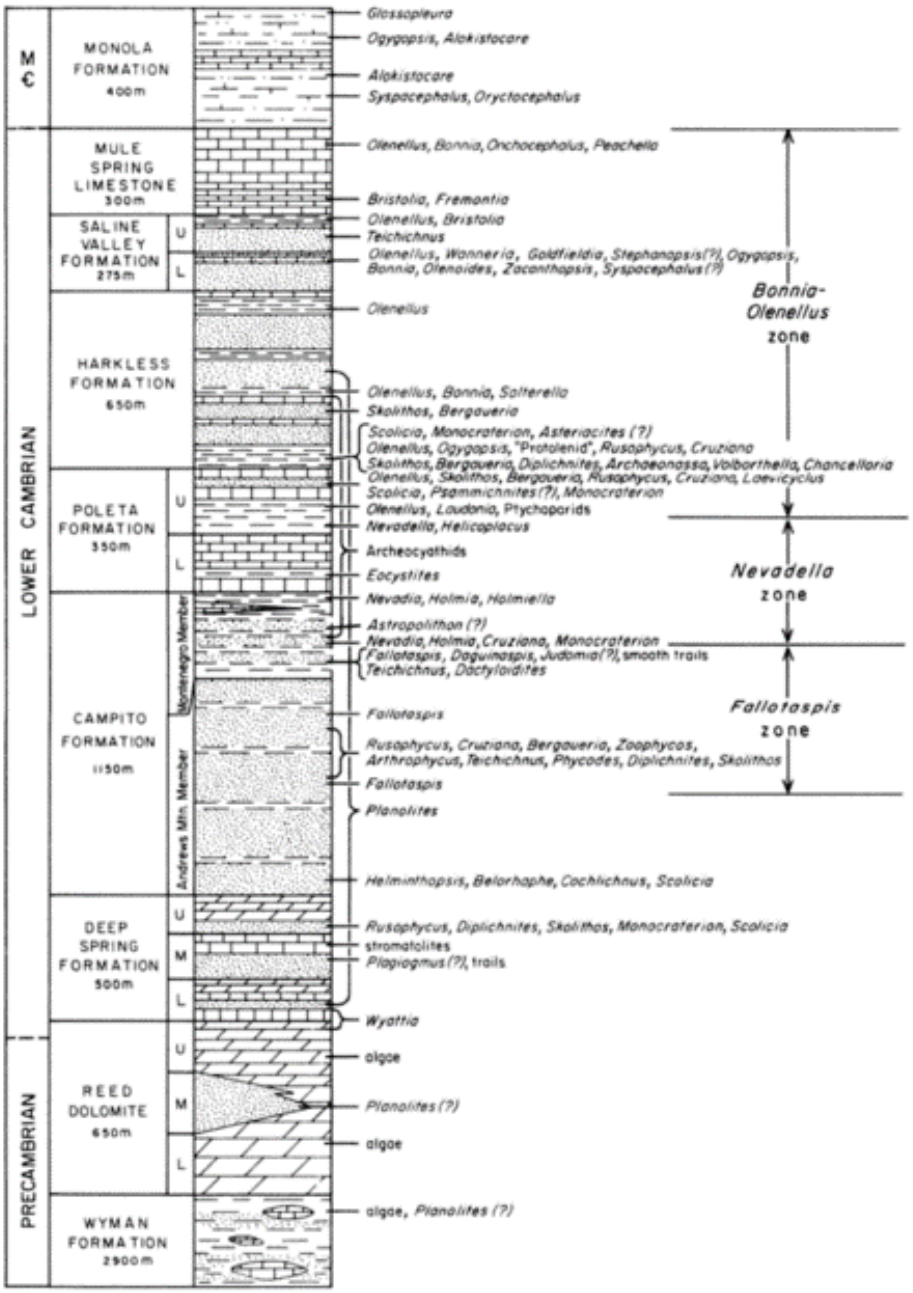

Figure 2.3: Precambrian to Middle Cambrian stratigraphy of the White-Inyo Range. Fossils include trilobites, acheocyathans, trace fossils, and Wyattia. (Nelson et al., 1991)

From Precambrian until present day, the rocks of the White-Inyo Range have experienced five deformational episodes: 1) Devonian-Mississippian deformation, 2) Permian-Triassic deformation, 3) Late Triassic-Jurassic deformation, 4) Mesozoic magmatism, and 5) Cenozoic

exhumation and volcanic eruption (Nelson et al., 1991; Coleman et al., 2003; Stockli et al., 2003).

DEVONIAN- MISSISSIPPIAN DEFORMATION

During the Devonian to Mississippian Antler orogeny, lower Paleozoic oceanic strata were thrust onto the western edge of the continental shelf, forming a marginal uplifted belt (Burchfiel and Davis, 1975). This tectonic event deformed the Neoproterozoic to Upper Cambrian sedimentary rocks into a series of NE-trending folds (Bateman, 1992; Stevens et al., 1997 and Morgan and Law, 1998). The correlation between the NE-trending folds and the Antler orogeny is based on the similarity in orientation of the folds in the White-Inyo Mountains with folds in Nevada and in the eastern Sierra Nevada.

PERMIAN-TRIASSIC DEFORMATION

Corbett et al. (1988) and Morgan and Law (1998) suggested that the regional scale N-to NW-trending folds in the White and Inyo Mountains are associated with movement on the underlying Last Chance thrust. This correlation is based on similarities in the orientation of structures in the footwall of the fault and the anticlines. The Last Chance thrust is a system of low angle reverse faults that have been active in the Early Permian (Stevens and Stone, 2002).

LATE TRIASSIC-JURASSIC DEFORMATION

The deformation at the White-Inyo Mountains that occurred in this period is associated with an episode of eastward contraction known as the East Sierran thrust system (Coleman et al., 2003). Based on geometric arguments Dunne and Walker (2004) suggested that some of the folds in the White Mountains that are Middle Triassic to Jurassic in age may geometrically correlate with the East Sierran thrust system. They also concluded that the development of brittle conjugate strike-slip faults in the southern Inyo Mountains, which accommodate minor NE-SW

contraction, marks the last episode of contraction in the East Sierran thrust system. Morgan and Law (1998) also correlated intense deformation on the western margin of the White Mountains with the East Sierran thrust system. However, Welch (2000) regarded the same deformation as a result of either the Antler orogeny or Early Permian Last Chance thrust system.

MESOZOIC MAGMATISM

The uppermost Precambrian to middle Mesozoic strata of the central White-Inyo Range are disrupted by middle-to-late Mesozoic intrusive rocks that resulted from large scale subduction of an ancient Pacific plate beneath the North American plate during the Nevadan orogeny (Nelson et al., 1991) (Figure 2.4). The period of plutonism started with the intrusion of the Beer Creek Pluton at approximately 175 Ma in the Early Jurassic, and ended with the intrusion of the Papoose Flat pluton at 83 Ma in the Late Cretaceous (McKee and Conrad, 1996; Miller, 1996). The plutons metamorphosed the sedimentary strata to slate, schist, and quartzite. The Birch Creek pluton, which formed in the Late Cretaceous (Barton, 2000), is the closest pluton to the study area. It lies on the east flank of the central portion of the White Mountains anticline. The pluton was episodically emplaced with alternating pulses from at least two distinct magma sources (Barton, 2000).

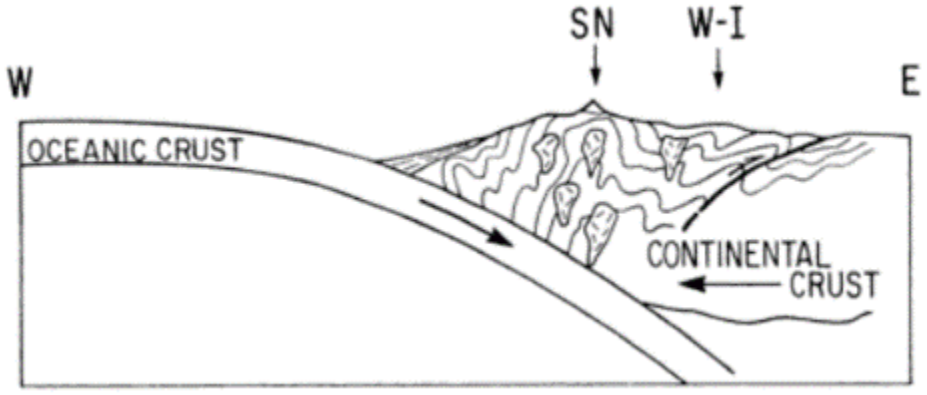

Figure 2.4: Schematic cross section of the western margin of North American during the convergent episode of the Nevadan orogeny. (From Nelson et al.,1991)

CENOZOIC EXHUMATION AND VOLCANIC ACTIVITY

The Cenozoic history of the White-Inyo Range is marked by uplift, basaltic volcanism, and alluvial-fan sedimentation related to Basin and Range extensional tectonism (Nelson et al., 1991; Snow and Wernicke, 2000; Stockli et al., 2003). The White Mountains underwent rapid exhumation and eastward tilting in the middle Miocene, starting at approximately 12 Ma (Stockli et al., 2003). At approximately 10 Ma, volcanic eruptions also occurred in the eastern White Mountains (Nelson et al., 1991).

CHAPTER 3: FRACTURE INITIATION AND PROPAGATION

FIELD AND EXPERIMENTAL OBSERVATIONS OF FRACTURE PROPAGATION

Formation of fractures involves nucleation, growth by propagation, and possibly coalescence with nearby fractures (Pollard and Aydin, 1988; National Research Council, 1996). Field and experimental observations indicate that nucleation of a fracture is associated with a preexisting heterogeneity or weak planes such as bedding planes or earlier formed fractures. Studies of fractures in layered siltstone and shales of the Appalachian Plateau, central New York, showed that fractures generally initiate from flaws such as fossil inclusions, concretions, cavities, and preexisting fractures along bedding interfaces (Bahat and Endelder, 1984; Helgeson and Aydin, 1991; Lacazetta and Engelder, 1992; McConaughy and Engelder, 2001). Defects such as air bubbles can initiate growth of mud cracks in wet soil (Corte and Higashi, 1964). In dolomite of the Judea Group, central Israel, spherical cavities serve as an initiation points for fractures (Weinberger, 2001). Fractures in granite deformed in a triaxial compression test nucleate in the intensively microcracked regions, and microcracks coalescence into fractures (Yukutake, 1992).

The process of fracture propagation is recorded in fracture surface markings such as hackles and rib marks or arrest lines that record the direction and velocity changes of fracture propagation. Hackle marks are curvilinear boundaries with differential relief between adjacent surfaces. Hackles either radiate from the origin or fan away from a curvilinear axis (Pollard and Aydin, 1988). A plumose structure is the collection of an origin, axis, and hackles. By drawing lines perpendicular to the hackles of a plumose structure, one can trace lines of fracture tips (Figure 3.1). Plumose structures are observed in both natural fractures and experimentally induced hydraulic fractures (Daneshy, 1973; Bahat et al., 2004; Savalli and Engelder 2005).

Change in remote stress orientation or magnitude can reactivate existing fractures and result in the formation of new fractures with different orientation. Engelder and Geiser (1980)

observed two cross-strike joint sets propagated during the development of the Appalachian Plateau in New York. Each set was formed by two different stress fields. Delaney et al. (1986) showed that tensile stress generated by magmatic pressure is sufficient to fracture host rock beyond the tip of dikes. Petit and Mattauer (1995) explained the heterogeneity in principal stress directions inferred in the Matelles exposure in France by the presence of nearby fault that disturbed the preexisting homogeneous stress field, leading to formation of a new set of fractures.

Cross-cutting relationships among fractures may allow determination of relative timing and sequence of structural events. Examples of field-based studies of regional fracture systems using cross-cutting relationships include Bergerat et al. (1992) who determined sequences of geologic events in the Colorado Plateau using cross-cutting faults and cross-cutting slickenside lineations. Peacock (2001) determined relative ages between joints and faults based on their cross-cutting relationship. Davatzes and Aydin (2003) inferred relative ages of components of a normal fault in the Jurassic Wingate and Navajo Sandstone at the Waterpocket monocline in Utah, using cross-cutting relationships. Flodin and Aydin (2004) and Myers and Aydin (2004) used cross-cutting relationships to determine relative ages of fractures of different sets associated with faults formed by shearing along joint zones in Aztec sandstone in Nevada. Ellis et al.(2012) created opening mode fracturing sequences in the Torridon Group Applecross Formation in Scotland based on cross-cutting relationships between fractures.

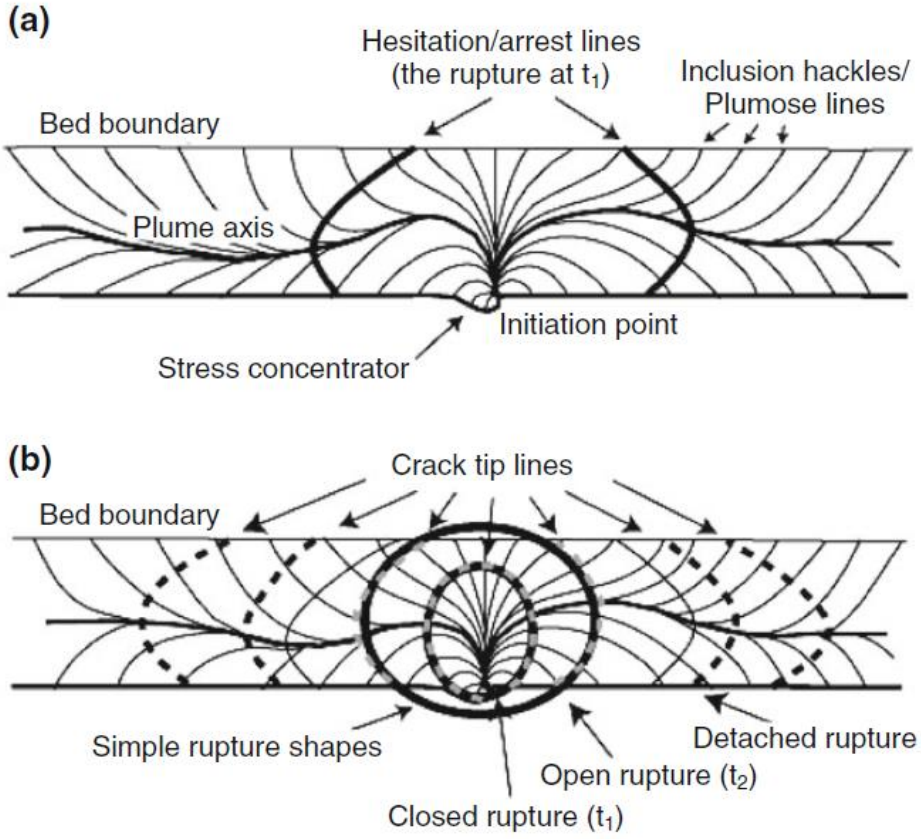

Figure 3.1: a) Features on fracture surfaces. A fracture initiates at a stress concentration point and propagates away from it. Plumose structures include an initiation point, hackles, and a plume axis. The plume diverges from the initiation point in the propagation direction. b) Fracture tip lines are the dashed curves drawn perpendicularly to the hackles (from Savalli and Engelder 2005).

MECHANICS OF FRACTURE FORMATION

There are multiple approaches for fracture initiation problems. In this review, I cover 1) the strength of materials approach, 2) the linear elastic fracture mechanics (LEFM) approach, 3) the elastic plastic fracture mechanics (EPFM) approach, and 4) the viscoelastic fracture mechanics approach.

The strength of material approach

This global approach to rock failure assumes rock to be elastic-brittle, which allows failure initiation to be instantaneous as the material exceeds a limit stress state. This approach provides information about the orientation of the failure surface but does not provide information regarding the length of the fracture (Ingraffea, 1989). The Mohr-Coulomb failure criterion is commonly used to describe the boundary of traction that a rock can sustain, and the stress conditions under different modes of fracture may occur (Jaeger et al., 2007). It also allows the graphical evaluation of the failure stress in terms of the applied effective principal stresses (σ_1 and σ_3) in a diagram of shear stress (τ) against effective normal stress (σ_n). The tractions on the failure surface can be calculated from:

$$\tau = \frac{1}{2}(\sigma_1 - \sigma_3) sin2\beta$$

$$\sigma_n = \tfrac{1}{2}(\sigma_1 + \sigma_3) + \tfrac{1}{2}(\sigma_1 - \sigma_3) cos2\beta \quad \text{(Zoback, 2010)}$$

where β is the angle between the shear fracture and the maximum compressive principal stress σ_1. σ_3 is the minimum compressive stress.

The Mohr-Coulomb failure envelope describes the shear stress a rock can sustain as a function of confining stress (Zoback, 2010). Rock fails when the Mohr-Coulomb circle is tangent to the failure envelope with the σ_n and τ values of the stress circle defining the normal and shear traction on the failure surface (Figure 3.2a). It is also possible to consider the change of strength with confining pressure in terms of a linearized Mohr-Coulomb failure envelope defined by μ_i, the slope of the failure line, and the unconfined compressive strength (UCS). The linearized Mohr failure can be described by

$$\tau = \text{UCS} + \sigma_n \mu_i \quad \text{(Zoback, 2010)}$$

The maximum tensional stress that a rock can sustain is called the tensile strength (T), which is the value on the failure envelope where $\tau = 0$. (Bons et al., 2012) Any τ-σ_n combination outside the failure envelope is impossible, as the rock cannot sustain such a state and would have failed.

Tension fractures occur when the Mohr circle touches the UCS. The failure plane will experience zero shear stress and an effective tensional stress. Faults or shear fractures will form when the Mohr circle touches the failure envelope (Figure 3.2c).

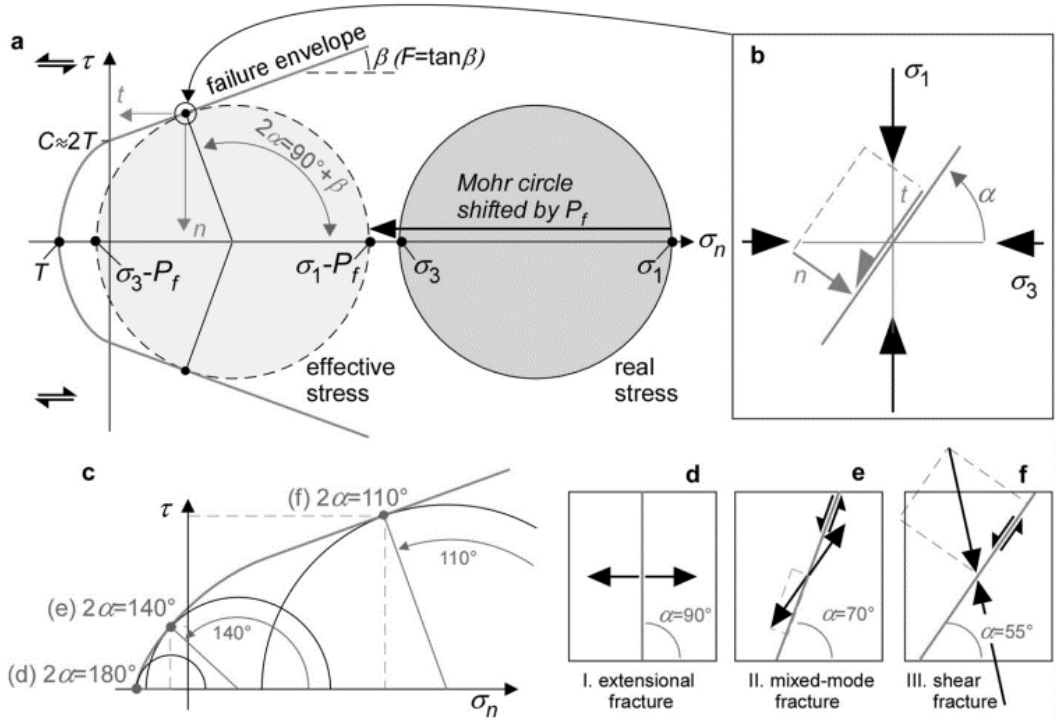

Figure 3.2: a) Mohr diagram that shows the shear stress (τ) and effective stress (σ_n) as a function of maximum effective stress (σ_1) and lease effective principle stress(σ_3) and its failure envelope. When pore pressure increases, the Mohr circle is shifted to the left since both of the effective stress values decreases. b) Example of normal (n) and shear stress (τ) on a plane at angle α to lease effective principle stress (σ_3). c) Example of the positions of the Mohr circle when the mode I(d), mode II (e) and mode III (f) fractures occur. d), e) and f are examples of extensional fracture, mixed mode fracture, and shear fracture, respectively (Bons et al., 2012).

The linear elastic fracture mechanics (LEFM) approach

A linear elastic material deforms by an amount proportional to the applied stress (Figure 3.3). When the stress is released, the material returns to its original undeformed state. The relationship between stress and strain can be described by a linear equation:

$\sigma_n = E e_n$, where σ_n is a normal stress, E is a Young's modulus, and e_n is the amount of extension, or strain (Twiss and Moores, 2007). The equation is identical to Hooke's law that describes the behavior of a spring that returns to its original shape after being compressed.

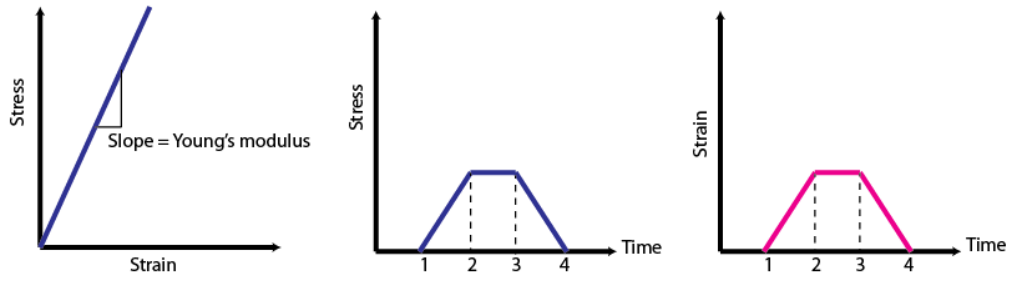

Figure 3.3: Characteristic of a linear elastic solid. Strain is a linear of function of stress. The stress increases from t=1 to t=2, stays constant from t=2 to t=3, and decreases from t=3 to t=4. The strain linearly follows the same trend. The material is recoverable, which means the material returns to its original state after the stress is released. (Adapted from Figure 16.1 in Twiss and Moores (2007)).

The basic assumptions of the LEFM approach are: 1) Stress intensity factor (K_I for opening mode fracture) is associated with a crack tip in a loaded structure. 2) each material has a critical stress intensity factor (K_{IC}), which can be compared to a critical tensile stress capacity; 3) Material behavior in the region near the front of the crack can be inelastic and non-linear. A crack forms when $K_I = K_{IC}$ when the region of inelastic deformation near the front of the crack is smaller in comparison to the other characteristic dimensions of the fracture; 4) The length of a

crack extension is controlled by the condition expressed in 3) and the crack will continue to propagate as long as the third criterion is satisfied, and will stop when $K_I<K_{IC}$. (Ingraffea, 1989; Anderson, 1995; Atkinson, 1984). K_{IC} represents the fracture toughness, which quantifies the stress required to propagate a fracture (Anderson, 1995).

Griffith Energy Balance

Griffith (1921) based his analysis of fracture propagation on the change in potential energy of a body that contains a crack. He stated that a crack can form only if there is a process which causes the total energy of a system to decrease or remain constant. The critical conditions for fracture can be defined as the point where crack growth occurs under equilibrium conditions, with no net change in total energy.

Consider a plate subjected to a constant stress,σ, which contains a crack of length 2a; the plate's width is much greater than the length of fracture (2a), and plane stress conditions prevail. In order for the crack to increase in length, sufficient potential energy must be available in the plate to overcome the surface energy of the material (γ_s). The stress necessary for the fracture to propagate (σ_f) is

$\sigma_f = \sqrt{\frac{2E\gamma_s}{\pi a}}$, where E is total energy. (Wei, 2010 and Anderson, 1995)

For a penny-shaped flaw embedded in a material, the fracture stress can be calculated from $\sigma_f = \sqrt{\frac{2E\gamma_s}{2(1-\nu^2)a}}$, where a is the crack radius and ν is Poisson's ratio. (Wei, 2010 and Anderson, 1995)

Shape of an aperture profile predicted by LEFM

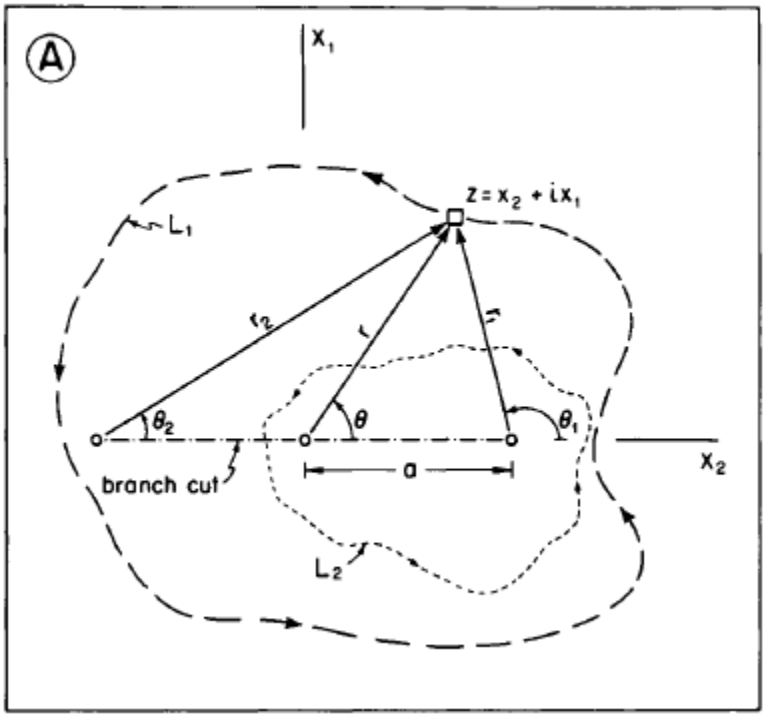

Figure 3.4: A tri-polar coordinate system includes r,θ which originated from the center of fracture; r1, θ1 with originated at the right had of the fracture, and r2 , θ2 with origin at the left-hand fracture tip. The line |x2| < a is a branch cut corresponding to fracture. The stress function is single-valued for the path L1, but not for path L2

Before considering the shape of an opening-mode fracture as predicted by linear elastic fracture mechanics, it is necessary to consider the stress along a fracture. For mode I fractures, the stress along the length of a fracture (fracture stress function – $\phi_I(z)$ where z is a function of the complex variable $z = x_2+ix_1$) can be written as

$$\phi_I(z) = (\sigma_{11}^r - \sigma_{11}^c)\left[\sqrt{(z^2 - a^2)} - z\right] + \frac{\sigma_{11}^r+\sigma_{22}^r}{2} z$$ (Equation 8.28 in Pollard and Segall, 1987)

The first term comes from the fracture itself, while the second term comes from remote loads in absence of the fracture. 2a is the width of the fracture. The displacement and stress fields around a fracture are defined by the real (Re) and imaginary parts of the $\phi_I(z)$ function. The displacement in Mode I fractures can be written as

$2\mu u_1 = 2(1-v)Im(\phi_1) + (1-2v)Im(\phi_2) - x_1 Re(\phi_1' + \phi_2')$ (Equation 8.25 in Pollard and Segall, 1987)

To transform the mathematical equations above into the physical interpretation, one can use the transformation equations $z = re^{i\theta}, z - a = r_1 e^{i\theta_1},$ and $z + a = r_2 e^{i\theta_2}$

So, the fracture stress function becomes

$$\phi_I(z) = (\sigma_{11}^r - \sigma_{11}^c)\left[\sqrt{r_1 r_2} e^{i(\theta_1+\theta_2)/2} - re^{i\theta}\right] + \frac{\sigma_{11}^r + \sigma_{22}^r}{2} re^{i\theta}$$

(Equation 8.30 in Pollard and Segall, 1987)

It is convenient to define $R = \sqrt{r_1 r_2}$ and $\Theta = (\theta_1 + \theta_2)/2$. Figure 3.4 illustrates the tri-polar coordinate system includes the variables r and θ.

In the case where a fracture only grows in length, $x_1 = 0^{\pm}$ and $|x_2| \leq a$ (Figure 3.4). The polar coordinates of the terms mentioned above will be $r = |x_2|;\ \ \theta = 0, \pi;\ \ r_1 = a - x_2;\ \theta_1 = \pi, -\pi;\ r_2 = a + x_2$ and $\theta_1 = 0, 2\pi$. Then $R = \sqrt{(a^2 - x_2^2)}$ and $\Theta = \frac{\pi}{2}$ and $\frac{3\pi}{2}$. Substituting equation 8.28 and 8.25 above by the r, θ, R and Θ values, provides the displacement along the length of the fracture as

$$\begin{Bmatrix} u_1 \\ u_2 \\ u_3 \end{Bmatrix} = \pm \begin{Bmatrix} \Delta\sigma_I \\ \Delta\sigma_{II} \\ \frac{\Delta\sigma_{III}}{1-\nu} \end{Bmatrix} \frac{(1-\nu)}{\mu} \sqrt{a^2 - x_2^2} + \begin{Bmatrix} \Delta\sigma_{II} \\ -\Delta\sigma_I \\ 0 \end{Bmatrix} \frac{(1-2\nu)x_2}{2\mu}$$ (Equation 8.34 in Pollard and Segall, 1987)

where the ± signs in the first term refer to the upper wall at $x_1 = 0^+$ and the lower wall at $x_1 = 0^-$.

The displacement components are a linear function of stress. The stress along the fractures causes the displacement in the x_2 direction (Figure 3.4) to have an elliptical distribution. The maximum value occurs at the center of the fracture, where $x_2 = 0$, and is proportional to the fracture length (a) and driving stress (the difference between remote normal stress and normal

stress on the crack). The displacement field goes to zero at $|x_2| = a$, the location of the fracture tip.

Both field observations and numerical models demonstrate that the elliptical equation above predicts the shapes of aperture profiles of natural fractures relatively well. Pollard and Segall (1987) asserted that the shape of a dilation profile of a basaltic dike segment near Ship Rock can be adequately described by the elliptical displacement equation (Figure 3.5).

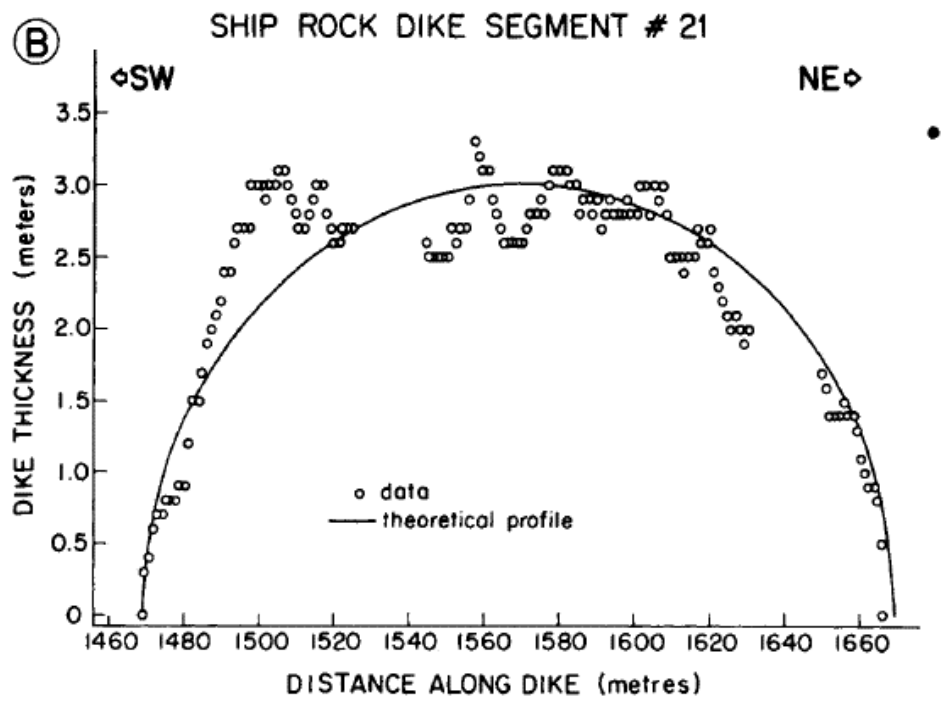

Figure 3.5: Aperture profile of a mafic dike near Ship Rock, New Mexico from Pollard and Segall (1987). The theoretical profile curve is plotted based on their equation 8.34.

Gudmundsson (2011) confirmed that displacements of many fractures along their length can be roughly described by an elliptical function. The author also gave examples of mineral-filled vein in gneiss in West Norway (p.389). Analytical solutions for fracture apertures affected

by overpressure variations given by Gudmundsson et al. (2012) and Kusumoto et al. (2013) show that aperture profiles are elliptical when the fluid pressure in the fracture is uniform (Figure 3.6).

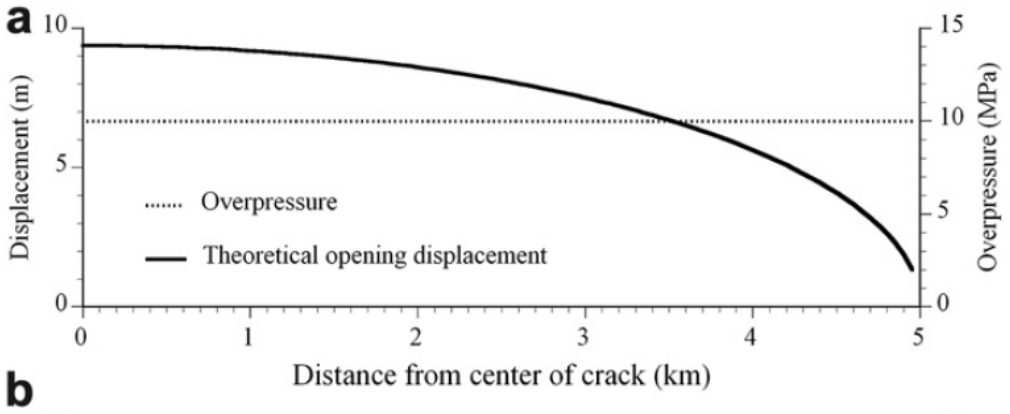

Figure 3.6: Example of an inverse model of an aperture profile of a fracture with a constant overpressure presented in Kusumoto et al. (2013). The dashed line indicates the assumed overpressure distribution, which is constant. The solid line illustrates the calculated displacement along the length of the fracture.

The elastic plastic fracture mechanics (EPFM) approach

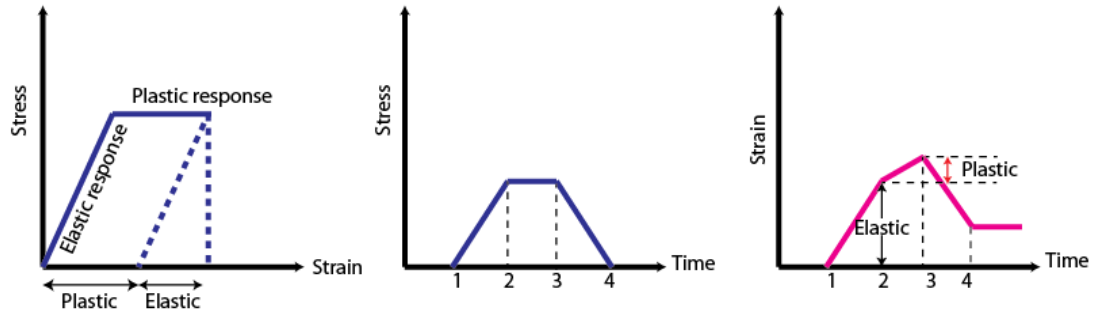

Figure 3.7: Characteristics of an elastic-plastic solid. The material responds in an elastic fashion below the yield stress, and later responds in plastic fashion. At t=2, the stress is equal to the yield stress, and the plastic deformation starts to occur. When the stress decreases at t=3, the elastic portion of the strain recovers, but the strain due to plastic deformation remains. At t=4, the material is permanently deformed and does not return to its original state like the linear elastic material does. (Adapt from Figure 16.8 in Twiss and Moores (2007)).

An elastic plastic material deforms in both recoverable elastic and permanent plastic manners (Figure 3.7). The permanent plastic deformation does not occur until the yield stress is reached (Twiss and Moores, 2007). It is analogous to a system of a box connected to a spring with the box sitting on a surface that has friction. When one applies force on the spring, the spring deforms in elastic manner. When the force exceeds the fictional force, the box starts to move (analogous to plastic formation). When the stress decreases, the elastic part of the deformation recovers but the plastic part remains.

Linear elastic fracture mechanics is valid when the plastic zone at the crack tip is small compared to the size of the K-dominant region. However, materials that have high fracture toughness or low strength can undergo extensive plastic deformation and fracture tip blunting prior to fracture growth (Kanninen and Popelar, 1985).

Dagdale (1960) observed yielding zones close to fracture tips in steel, which behave in an elastic plastic fashion. Figure 3.8 illustrates the Dugdale model, in which the yield zones (shaded in gray) are under a uniform tensile yield stress. The yield zones can be regarded at cohesive zones (Jin and Sun, 2005). The arrows in the figure represent remote tension. The material outside of the zones is elastic and is bounded by an ellipse of length 2a, where 2a = 2(l+s). The variable l represents half of fracture length, and the variable s represents the length of the yield zone at one tip. There is also no stress singularity at the fracture tip (Brison, 1970). Jin and Sun (2005) asserted that the stress singularity at fracture tips cannot be zero unless the cohesive law has a nonzero traction at the initial zero-opening displacement.

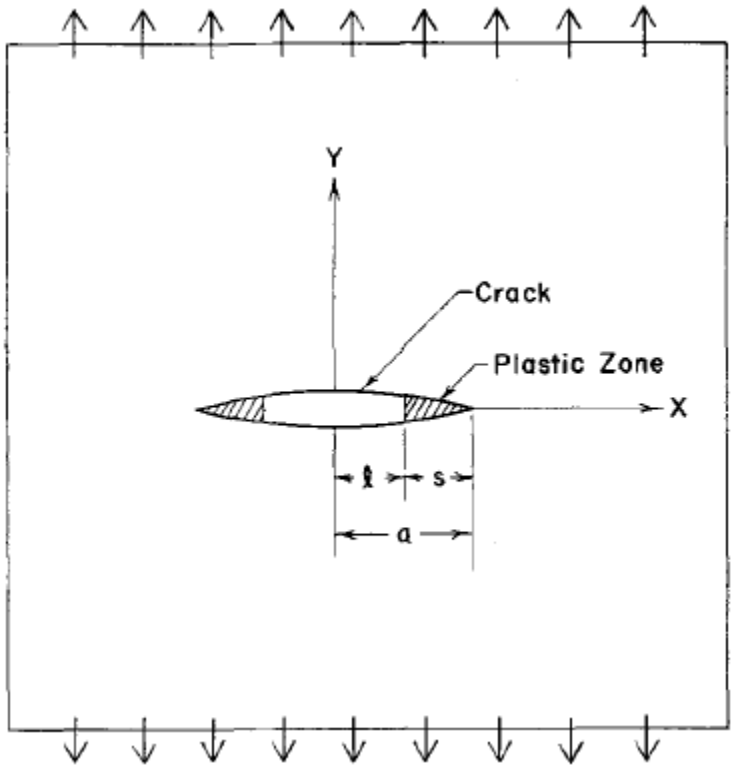

Figure 3.8: The Dugdale model presented in Brinson, 1969

Two parameters that describe fracture toughness in elastic-plastic materials are the crack opening displacement (CTOD) and the J contour integral (Kanninen and Popelar, 1985; Anderson, 1995). Both parameters can also be used as a fracture criterion. The CTOD is the opening displacement at the tip at the end of the cohesive zone. The J integral can be compared to the K-value in the LEFM case. The relationship between the K-value, J integral and CTOD can be described by

$$J = \frac{K^2}{E} = m\sigma_{ys}CTOD ,$$

where E is Young's modulus, m is a dimensionless constant that depends on the material properties and the stress state, and σ_{ys} is the small-scale yielding stress (Anderson, 1995). In the basic EPFM analysis, the J integral should not exceed the critical J integral, and the CTOD should not exceed the critical CTOD.

Shape of an aperture profile predicted by EPFM

Kanninen et al. (1969) present an analytical solution for displacement along fracture length as

$$u(x) = \frac{2a\sigma_y}{E}\left\{log\left|\frac{\sqrt{c^2-a^2}+\sqrt{c^2-x^2}}{\sqrt{c^2-a^2}-\sqrt{c^2-x^2}}\right| + \frac{x}{a}log\left|\frac{\sqrt{c^2-a^2}-\sqrt{c^2-x^2}}{\sqrt{c^2-a^2}+\sqrt{c^2-x^2}}\right|\right\},$$

where u(x) is the displacement at distance x from the center of fracture, c is half of fracture length, σ_y is a yield stress, and a is the non-cohesive zone. According to the model, the linear elastic portion of the fracture has an elliptical shape, while the elastic-plastic parts are sigmoidal (Figure 3.9).

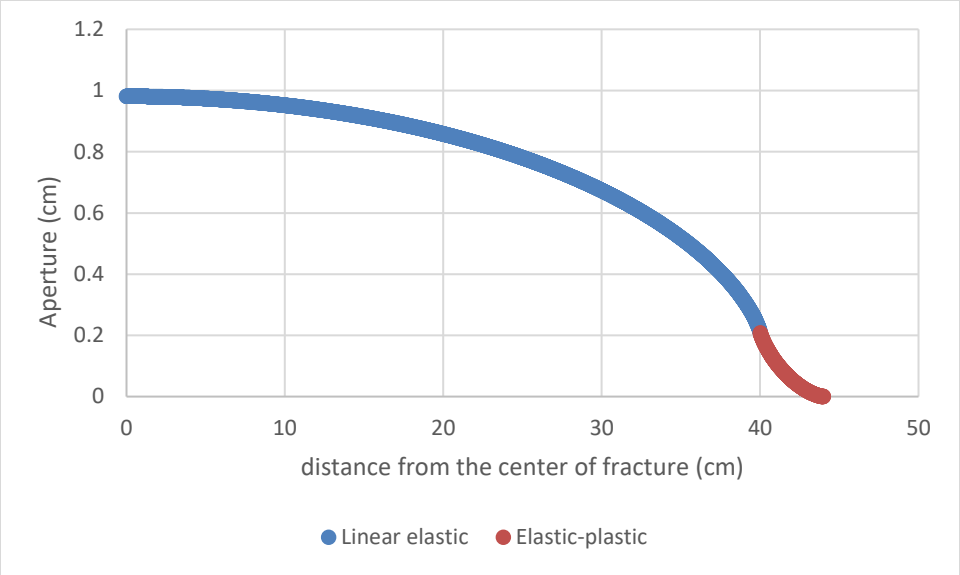

Figure 3.9: Shape of half of an aperture profile predicted by Kanninen et al.(1969) model. Half of fracture length is 44 cm, and non-cohesive zone is 40 cm,

Goodier and Field (1963) discovered that, based on Dugdale's model, the displacements along the length of fractures tend to have tapered profiles. They propose the following equation for the fracture opening displacement u(x) along the fracture:

$$u(x) = \frac{\sigma y l}{\pi E}\left[cos\theta \log\frac{\sin^2(\theta_2-\theta)}{\sin^2(\theta_2+\theta)} + cos\theta_2 log\frac{(sin\theta_2+sin\theta)^2}{(sin\theta_2-sin\theta)^2}\right],$$

Where σ is an applied stress, y is a yield stress, l is the length of fracture,

$$cos\theta_2 = \frac{a}{l}, \cos\theta = \frac{x}{l}\ for\ |x| < l, -\pi < \theta < \pi\ and\ \theta_2 = \frac{\pi\sigma}{2\sigma y}.$$

Schaeffer et al. (1971) used the equation above to calculate the displacement along the length of a fracture in a steel sheet and compared it against the result of their measurement of the relative displacement between the fracture surfaces and between the upper and lower boundaries of the strip necking regions at fracture tips. The strip necking regions are the areas with extensive strain concentration caused by the necking of the material. Both the measured and the calculated values show that the fracture tips and the necking zones have a sigmoidal shape. Both

the calculated and measured curves in Figure 3.10 are similar to the analytical solution proposed by Kanninen et al. (1969) shown in Figure 3.9.

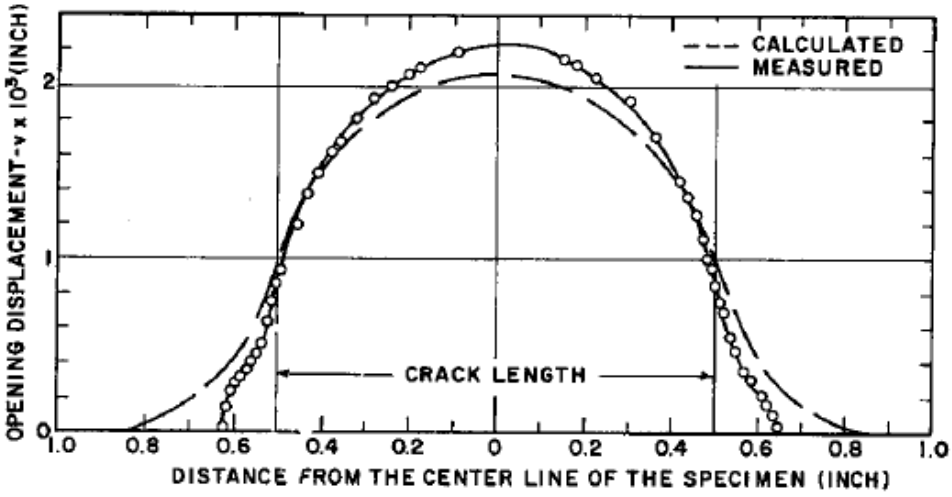

Figure 3.10: Opening displacement along fracture in a thin cracked steel plate in Schaeffer et al. (1971). The areas beyond crack length are the area the strip necking regions.

Brinson (1970) presents the photoelastic photographs of the Dugdale yield zones in polycarbonate. The examples of the photographs are shown in Figure 3.11 below. The cracks are elliptical holes in the center of the photos. As the ratio of T (tensile stress) to Y (yield stress) increases, the yield zones become more prominent. At T/Y = 0.704, the yield zones are cone-shaped. The fracture tips are almost triangular, while the fracture shape is an elongated hexagon.

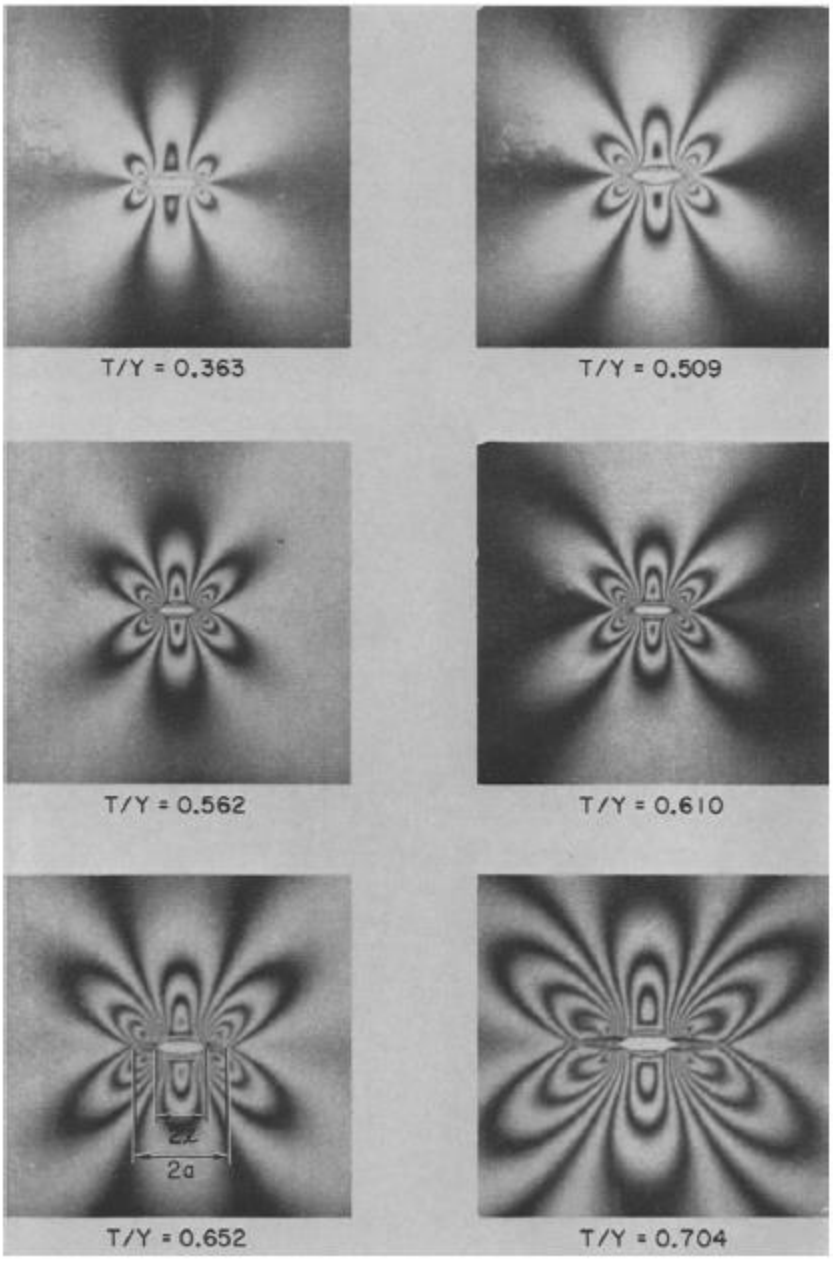

Figure 3.11: Dugdale yield zones in polycarbonate presented in Brinson (1970).

Vermilye and Scholz (1995) presented aperture profiles of fractures from Culpeper Quarry and Florence Lake with tapered displacement gradients at the tips. They claim the tapered displacement gradients are consistent with Dugdale's (1960) elastic plastic model, and the tapered tips represent regions of inelastic deformation. The examples of the fracture aperture profiles from Calpeper Quarry in their study are shown in Figure 3.12 below.

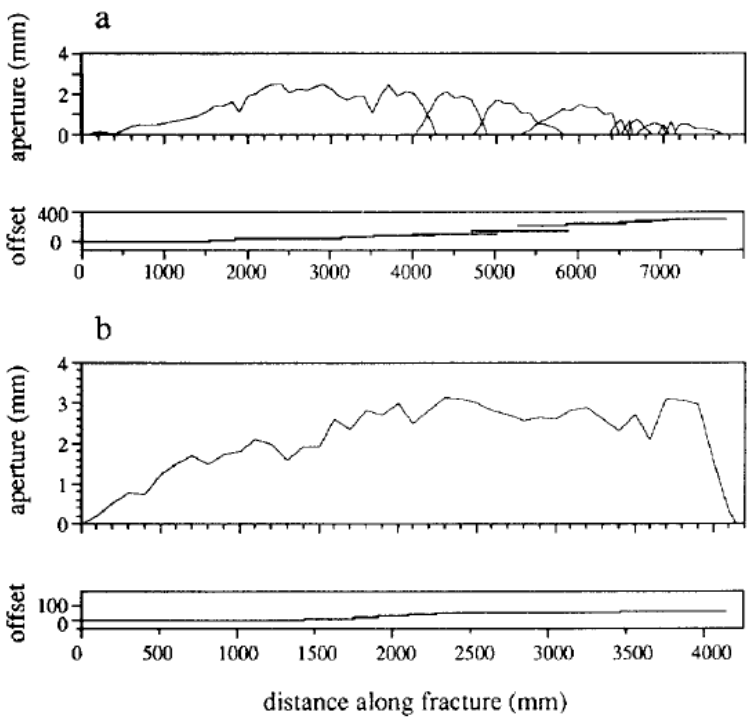

Figure 3.12: The plots of apertures along fractures from Culpeper Quarry presented in Vermilye and Scholz (1995). Both fractures with non-connected segments and well-connected segments display tapered tips.

The viscoelastic fracture mechanics approach

Viscoelastic material exhibits both viscous and elastic properties (Broberg, 1999; Twiss and Moores, 2007). The permanent viscous strain starts as soon as the material experiences stress (Figure 3.13). The viscous part implies that the material does not respond reversibly to unloading after loading. The elastic component implies partial reversibility.

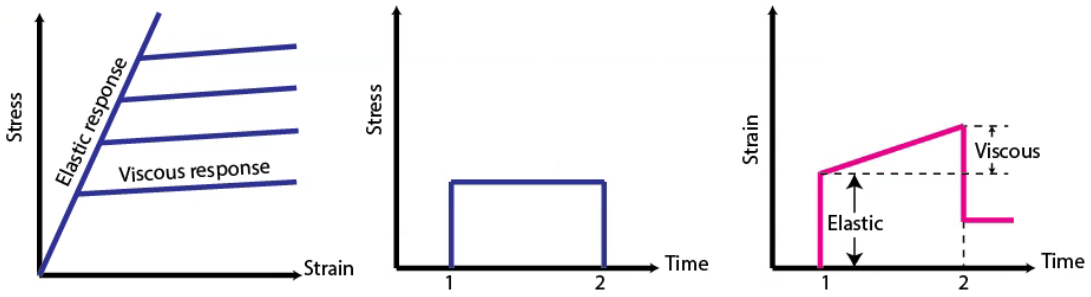

Figure 3.13: Characteristics of a viscoelastic material. In the first graph on the left, the magnitude of the elastic response depends on the magnitude of the stress applied. The stress is instantly imposed at t=1, and then stays constant until t=2. The response to the imposed stress includes an instantaneous recoverable elastic deformation and a permanent viscous deformation. (Adapted from Figure 16.5 in Twiss and Moores (2007)).

When the material is linearly viscous, μ(t), the modulus of rigidity or shear modulus at time t, and κ(t) , the modulus of compression or Bulk modulus at time t, can be written as

$$\mu(t) = \left[\mu_\infty + (\mu_0 - \mu_\infty)e^{\frac{-t}{t_0}}\right]U(t)$$

$$\kappa(t) = \left[\kappa_\infty + (\kappa_0 - \kappa_\infty)e^{\frac{-t}{t_0}}\right]U(t)$$

(Equation 4.15.3 in Broberg, 1999), where U(t) is the unit step function, μ_0 is the initial shear modulus, μ_∞ is the shear modulus as time approaches infinity, κ_0 is the initial bulk modulus, and κ_∞ is the shear modulus as time approaches infinity. If a material displays the power law

relationship between stress and strain, μ(t) and κ(t) can be expressed as

$\mu(t) = \mu_p \left(\frac{t}{t_0}\right)^{-\alpha} U(t)$ and $\kappa(t) = \kappa_p \left(\frac{t}{t_0}\right)^{-\alpha} U(t)$ (Equation 4.15.6 in Broberg, 1999), where $0<\alpha<1$, and μ_p and κ_p are the initial shear modulus and bulk modulus of the power law material, respectively. The behavior of the power law model is best suited for the case where the time range of interest is long. The μ(t) and κ(t) values are non-negative, and the change in μ(t) and κ(t) are non-positive because the material's memory is fading, or at least not improving, over time. Also, note that $\mu(t) > \mu(\infty)$ and $\kappa(t) > \kappa(\infty)$.

A viscoelastic material subjected to a suddenly-applied constant stress exhibits creep or an increase in strain with time. In this case, the displacement along the fracture in the linear viscoelastic material is

$(x) = \frac{\sigma_y^\infty (\frac{1}{\mu_\infty} - (\frac{1}{\mu_\infty} - \frac{1}{\mu_0}) e^{-\frac{\mu_\infty t}{\mu_0 t}} U(t) \sqrt{a^2 - x^2}}{4\mu(t)} \times (3\kappa(t) + 4\mu(t))$ (Equation 4.15.18 in Broberg, 1999)

for $|x|<a$, and in the power law viscoelastic material the displacement is

$(x) = \frac{\sigma_y^\infty \sin \alpha\pi \left(\frac{t}{t_0}\right)^\alpha U(t) \sqrt{a^2 - x^2}}{4\pi\mu_p \alpha \mu(t)} \times 3\kappa(t) + 4\mu(t)$ (Equation 4.15.20 in Broberg, 1999)

The shapes of the aperture profiles of a fracture in a linear viscoelastic material and a power law viscoelastic material are elliptical, as they have been governed by the $\sqrt{a^2 - x^2}$ terms in both equations (Figure 3.14).

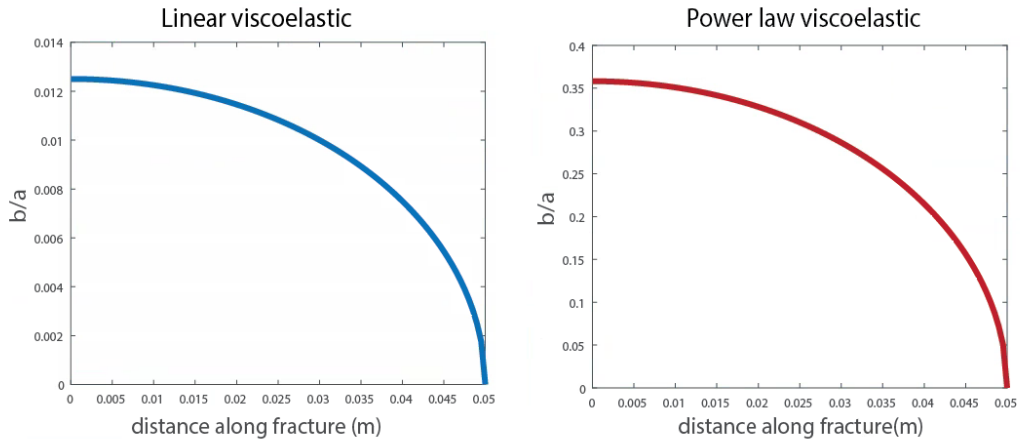

Figure 3.14: Shapes of aperture profiles of fractures in linear viscoelastic (left) and power law viscoelastic (right) material. The aperture profiles are results of the analytical solutions in Broberg (1999). The time interval is 10^6 years. The initial shear modulus at time t=0 is 35 MPa, and the final shear modulus is 10 MPa. The initial bulk modulus is 66 MPa, while the final bulk modulus is 30 MPa. The terms $\frac{\sigma_y^\infty}{4}$ and $\frac{\sigma_y^\infty}{4\pi}$ are assumed to be 0.5, and α = 0.1.

DEFORMATION MECHANISM MAP

Riedel (1987) proposes a fracture mechanism map of materials such as steel and alloys (Figure 3.15). Each region of the fracture mechanism map represents a prevailing mechanism at a certain temperature and pressure. Note that the location of the boundaries between the different mechanisms varies among different materials, and the map does not include effects of chemical reactions.

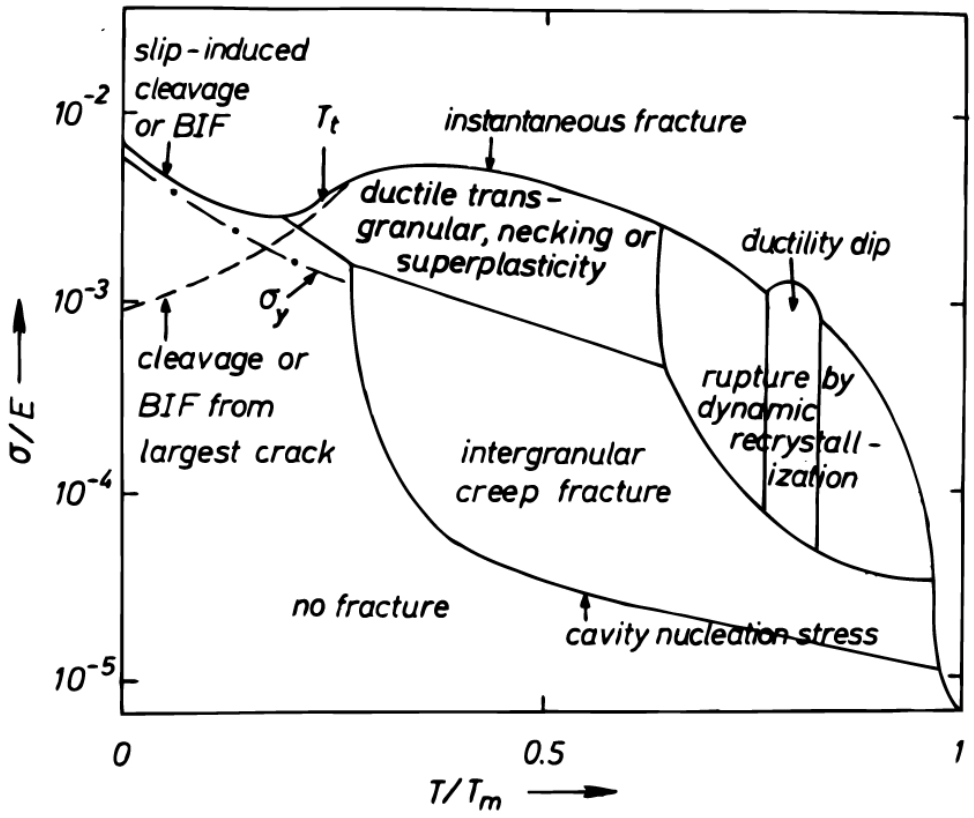

Figure 3.15: Schematic map of fracture mechanisms in Riedel (1987)

The cleavage and brittle intergranular fractures (BIFs) form by formation of fractures along weak planes in the material, such as micro-cracks or impurities. High stress can cause slip or shear fractures at low temperature (Riedel, 1987). Above the brittle-ductile temperature, the deformation changes to a ductile transgranular mode. Fractures can form by coalescence of small

cracks if the stress is high. However, when the stress is low, fractures may form slowly by creep flow. Necking occurs when materials behave in an elastic plastic manner (see section Shape of an aperture profile predicted by the EPFM above). Superplasticity occurs when crystal grains slide past one another. The sliding of the grains is accommodated by diffusion at grain boundaries (Twiss and Moores, 2007). At very high temperature and high stress, the mechanism shifts to dynamic recrystallization, which includes migration of grain boundaries. At this state, the formation of new grains in heavily deformed regions is more favored than the recovery processes operating in the creep regime. Ductility dip occurs when the materials become molten due to melting at grain boundaries (Riedel, 1987; Twiss and Moores, 2007).

Rutter (1976) created deformation mechanism maps of rock based on a theoretical models and experimental data. Figure 3.16 is an example of a deformation mechanism map for quartz published in his paper. Pressure solution is diffusion in a thin fluid film along grain boundaries (Knipe, 1988). Dislocation glide is slip motion of a lattice plane. The strain is confined to slip planes (Knipe, 1988; Lloyd and Knipe, 1992). Dislocation creep takes place by the migration of atoms of the material from areas of high compressive stress to areas of low compressive stress. Diffusion creep can result from the diffusion of point defects though a crystal lattice, the diffusion of atoms or ions along grain boundaries, or the diffusion of dissolved components in a fluid along the grain boundaries (Twiss and Moores, 2007). Nabarro-Herring Creep describes deformation resulting from movements of atoms away from a high-stressed face through pathways in the crystal structure of the grain with the atoms accumulating on a low stress face. The creep causes shortening of the crystal in the direction parallel to the maximum compressive stress and elongation in the direction parallel to the minimum compressive stress (Knipe, 1988; Twiss and Moores, 2007).

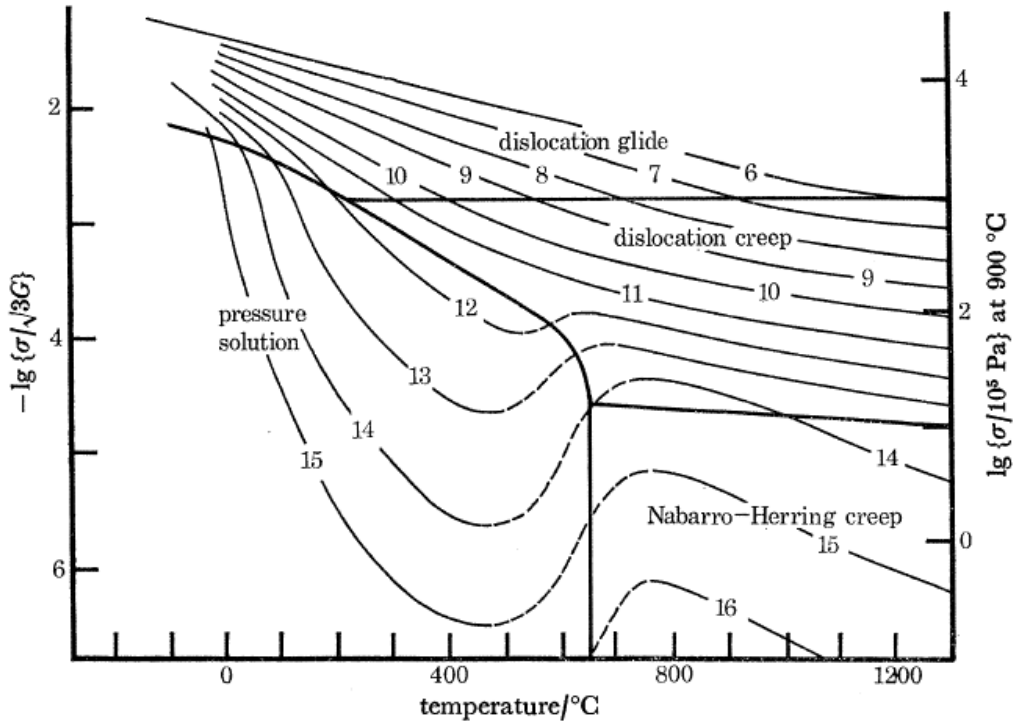

Figure 3.16: Deformation mechanism map for quartz from Rutter (1976)

FRACTURE GROWTH IN THE VICINITY OF OTHER FRACTURES

Delaney and Pollard (1981) demonstrated that interaction between two fractures tips could cause the fracture tips to warp toward each other and become tapered (Figure 3.17B). In the example presented by Pollard and Segall (1987), the linear aperture profile in the southwest section of one of the Ship rock dike segments is believed to have resulted from elastic interaction with neighboring dike segments. Shen et al. (1995) showed that two parallel fractures located at various angles curve toward each other and coalesce due to shear failure. The curved fracture propagation is observed in multiple studies, including analogue experiments, field observation, and numerical studies (glass: Swain and Hagan, 1978; quartz-feldspar veins in the Cottonwood stock, Utah: Lawton, 1980).

Delaney and Pollard (1981) also showed that two closely spaced collinear dike segments propagate preferentially toward each other. The small separation also causes a slightly greater dilation of adjacent ends, resulting in relative blunting of tips (Figure 3.17A).

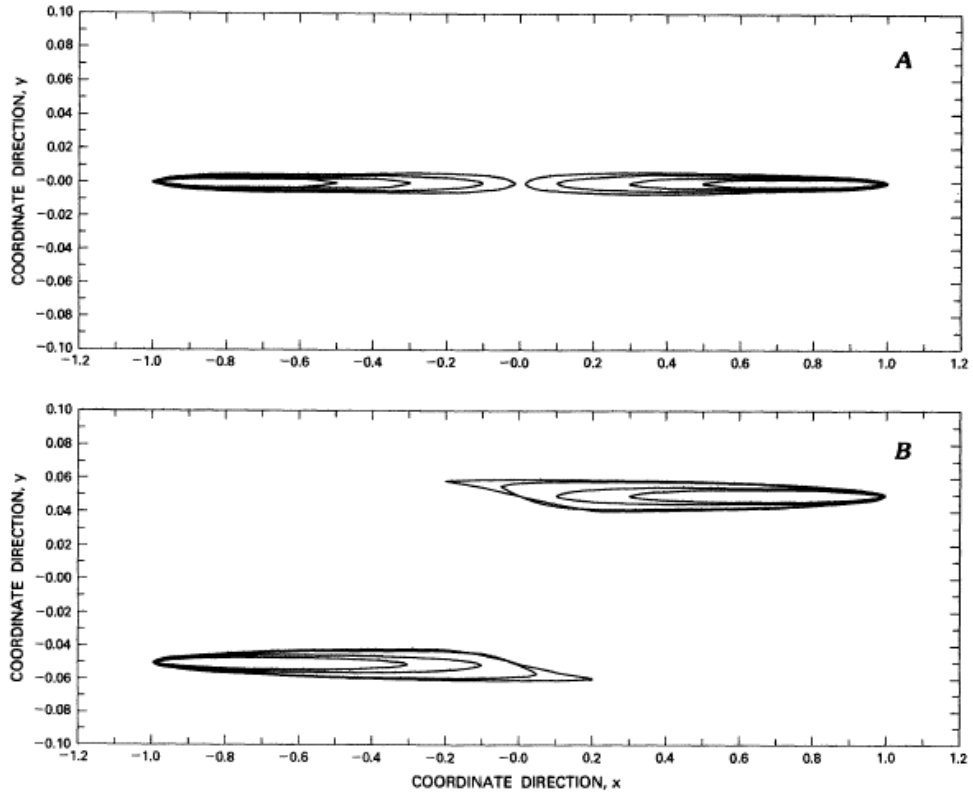

Figure 3.17: Models of pairs of collinear and offset fractures presented in Pollard and Delaney (1981). A) the adjacent tips of two collinear fractures have slightly greater dilation, resulting in relative blunting of tips. B) The adjacent tips of offsetting fractures warp toward each other, resulting in asymmetry and sharpening of the tips.

SUBCRITICAL FRACTURE GROWTH

In systems subjected to long-term loading, especially when high temperatures or reactive environments are present, the classical fracture mechanics approach fails to predict fractures propagation (Atkinson and Meredith, 1987). Subcritical fracture growth occurs when a significant rate of fracture extension occurs at a value of stress intensity factor (K_I) below K_{IC} (Atkinson, 1984). Subcritical crack growth involves several competing mechanisms, such as stress corrosion, diffusion, ion exchange, and microplasticity (Nara et al., 2006)

Stress corrosion involves weakening of strained bonds at crack tips by the chemical reaction of an environmental agent, such as water, thereby facilitating crack growth. Under low homogeneous temperatures and atmospheric pressure, stress corrosion is the dominant mechanism of subcritical growth. (Nara et al., 2006; Atkinson and Meredith, 1987).

Michalske and Freiman (1982, 1983) proposed that mechanical strength of vitreous glasses and ceramics decreases with time due to slow growth of pre-existing surface flaws caused by stress corrosion. In silicates, strained Si-O bonds at crack tips can react more readily with water than unstrained bonds because of a strain-induced reduction in overlap of atomic orbitals. The chemical interaction between the intrusive water molecule and strained siloxane bonds is a three-step sequence: adsorption, reaction, and separation. For silicate glasses and quartz in water environments, a general expression for weakening of silicate is

H-O-H + [ΞSi-O-SiΞ] ↔ ΞSi-OH.HO-SiΞ ↔ 2[ΞSi-OHΞ] (Atkinson, 1980).

This chemical reaction shows the hydrolysis of strong Si-O bonds to weaker hydrogen-bonded hydroxyl groups linking the silicon atoms, which is a first-order chemical reaction.

Another possible reaction is

ΞSi-O-SiΞ + OH^- ↔ ΞSi-O^- + ΞOH^- (Charles, 1958 and Nara et al., 2006).

In this chemical reaction, stress corrosion of Si-O-Si bonds has been attributed to both ionized water and to molecular water. Atkinson and Meredith (1981) also asserted that high hydroxyl ion concentration results in an increasing rate of crack growth.

Effect of temperature on fracture growth

In addition to stress corrosion, at high homologous temperatures fractures can form due to mass transport or diffusion. Meredith and Atkinson (1985) showed that higher temperatures raise the activity of water species, which accelerates stress corrosion reactions at crack tips. High temperature also changes the thermal micro-crack characteristics, and lowers the K_{IC} values.

In addition, at high temperature, cracks can grow by diffusion of vacancies to crack tips or by diffusional cavity (Atkinson and Meredith, 1985). Karunaratne and Lewis (1980) observed diffusional crack growth in Si-Al-O-N ceramics at high temperature.

CRACK-SEAL GROWTH MECHANISM

Crack-seal cement is indicative of multiple stages of brittle fracture opening, alternating with stages of cementation (Figure 3.18). After a fracture opens, cement precipitates from fluid that flows through fractures and seals or connects the opening gap, and the cycle repeats. The crack-seal texture is primarily observed in fractures in low-grade metamorphic rocks (Knipe, 1977; Ramsay, 1980; Anders and Wiltschko, 1994). Crack-seal textrures have also been observed in sandstone (Laubach et al., 2004a; Laubach et al., 2004b), and in carbonate (Gale et al, 2010; Holland and Urai, 2010; Ukar and Laubach, 2016) where crack-seal quartz cement can precipitate in the form of isolated cement bridges.

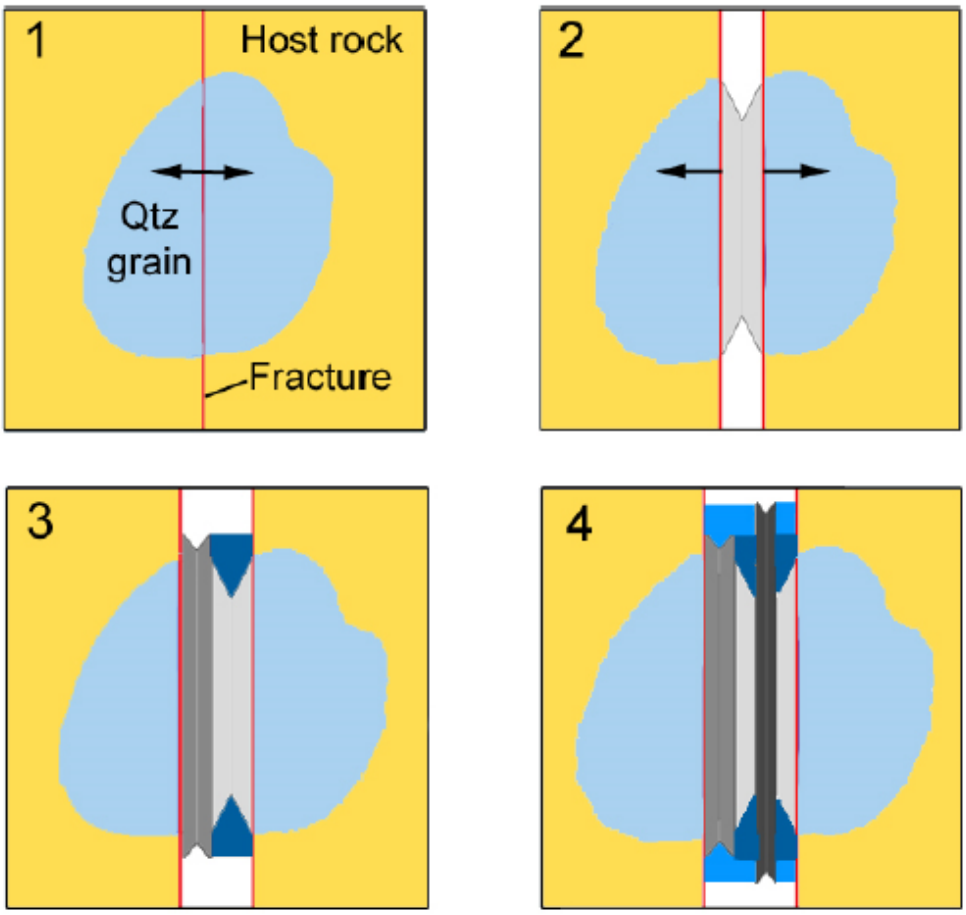

Figure 3.18: A model of crack-seal bridge formation from Alzayer(2014): 1) A fracture separates a quartz grain into two parts. 2) The first generation of quartz cement (light gray) precipitates, connecting the fracture walls. 3) Another opening occurs, the second generation of quartz cement (dark gray) precipitates simultaneously with euhedral quartz cement (dark blue). 4) Another opening event separates the first-generation cement, and another phase of euhedral quartz cement (light blue) precipitates at the same time.

Lander and Laubach (2014) proposed that the isolated quartz cement bridge occurs when the rate of opening is between the slowest and fastest growth rates of the cement in the fractures (Figure 3.19). The quart cement bridge can occur due to quartz cement growing along the c-

crystallographic axis of a quartz grain that is orientated approximately perpendicular to fracture walls (Laubach et al., 2004a; Becker et al., 2010).

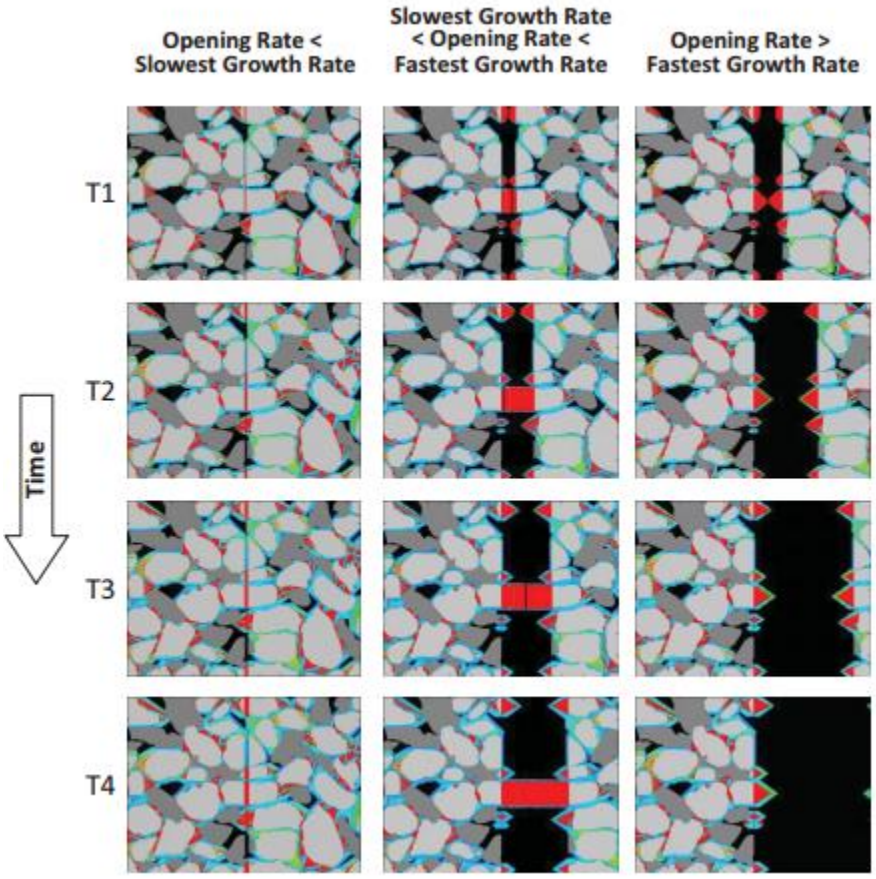

Figure 3.19: Simulations of grain packs with three distinct ratios of fracture opening to crystal growth presented in Lander and Laubach (2014). The red and green indicate fast growth along non-euhedral surfaces, while the cyan indicates growth on euhedral surfaces. Black is porosity, gray is non-quartz grain. The rate of fracture opening in the left column is lower than the rate of growth on the euhedral face. The middle column shows the intermediate case where some, but not all, quartz cement growths are able to keep up with micro-fracturing events. The right column shows results where the fracture opening rate is faster than the fastest growth rate of cement, not allowing cement bridges to form.

CHAPTER 4: METHODS

FRACTURE APERTURE PROFILE DATA COLLECTION

I collected 38 fracture aperture profiles and 27 hand samples at 34 field locations. The field locations are divided into northern and southern stations. The northern stations are approximately 5 km east of the White Mountains anticline and south of the Birch Creek pluton, and they are in various locations including 1) along Hwy CA-168 in Payson Canyon east of Westgard Pass, 2) in Mollie Gibson Canyon, and 3) along National Forest Road N2121. The southern locations are located on the western limb of the anticline along Hwy CA-168 (Figure 2.1).

Figure 4.1: Position of the caliper is perpendicular to the width of the fracture. I collected data at a 1 mm interval for approximately 20 mm from each fracture tip, and at 2 mm and 5 mm intervals after 20 mm and 50 mm from the tip, respectively.

Aperture profiles were collected in the field for fractures that expose at least one, but preferentially both tips using a hand lens, a caliper, and a measuring tape. The caliper was placed perpendicular to the fracture wall to obtain the true opening displacement for fractures oriented

obliquely to the exposure (Figure 4.1). The caliper allowed measurements of apertures as small as 1 mm with the precision of 0.1mm. Exposures were selected to provide profiles of fractures oriented roughly perpendicular to the outcrop face. I chose fractures that are partially or completely filled with cement to investigate the correlation between textures of cement and ellipticity of fractures. To capture the change in aperture close to the fracture tips, I collected data at a 1 mm interval for approximately 20 mm from each fracture tip, and at 2 mm and 5 mm intervals after 20 mm and 50 mm from the tip, respectively. For all measured fractures I documented 1) orientation, 2) textural characteristics and compositions of fracture cement, 3) shape of fracture tips, 4) locations of fracture tips relative to layer boundaries, and 5) shapes of fracture tips. Fracture tips were assigned to one of two categories: fracture tips that end within 1 cm of a layer boundary, and fracture tips that end more than 1 cm away from a layer boundary. Because lithologic layer boundaries can be gradational and fracture tips are difficult to define with a precision of <1-5 mm, we chose 1 cm from a layer boundary as our classification distance.

Samples were collected for fracture aperture analysis in the lab with at least one preserved tip. Aperture profiles on fractures were collected using the same method as in the field. The same fractures were analyzed in thin section using transmitted light microscopy to determine textural characteristics and mineral compositions of fracture cement and host rock. I also measured micro-scale aperture profiles of the fractures from thin section images using the measuring tool in Adobe Photoshop. Overall, I collected an additional nine from hand samples and 12 aperture profiles thin sections.

.

ENERGY-DISPERSIVE X-RAY SPECTROSCOPY (EDS) STUDY OF THE HOST ROCK

I utilized SEM-based energy-dispersive X-ray spectroscopy (EDS) to identify the mineral composition of the Campito Formation. Two thin sections were prepared from the hand samples. The samples were double-polished for later fluid inclusion study and carbon-coated. I used a JEOL JSM-6490LV Scanning Electron Microscope (SEM) with the setting of 20 kV accelerating voltage, Hi Vac mode, 10 mm working distance, 50 µm spot size, and an aperture of 2.

The spectra of all of the minerals were collected in Backscattered Electron (BSE) Shadow Mode images in the EDEX Genesis program. After mineral identification was completed, I collected maps of 11 elements including Al, Ca, Fe, K, Mg, Mn, Na, O, P, Si, and Ti for an area of 2.5 mm x 2.0 mm on each thin section (Figure 4.2). The settings were the following: spectral, 1024x800 resolution, 200 µs dwell time, and 64 frames. In addition, I used these spectral maps to create multiple overlay maps, and then used all of them to conduct point-counting in JMicrovision to determine percentages of all minerals found in the thin sections. I used a point-count grid of n=500 points. The point-count categories were 1) quartz, 2) apatite, 3) chlorite, 4) mica, 5) ilmenite, 6) orthoclase, 7) rutile, and 8) magnetite. The software also has a function to overlay images on top of a base image, which allows me to use Ti-Fe maps to distinguish ilmenite from magnetite and rutile.

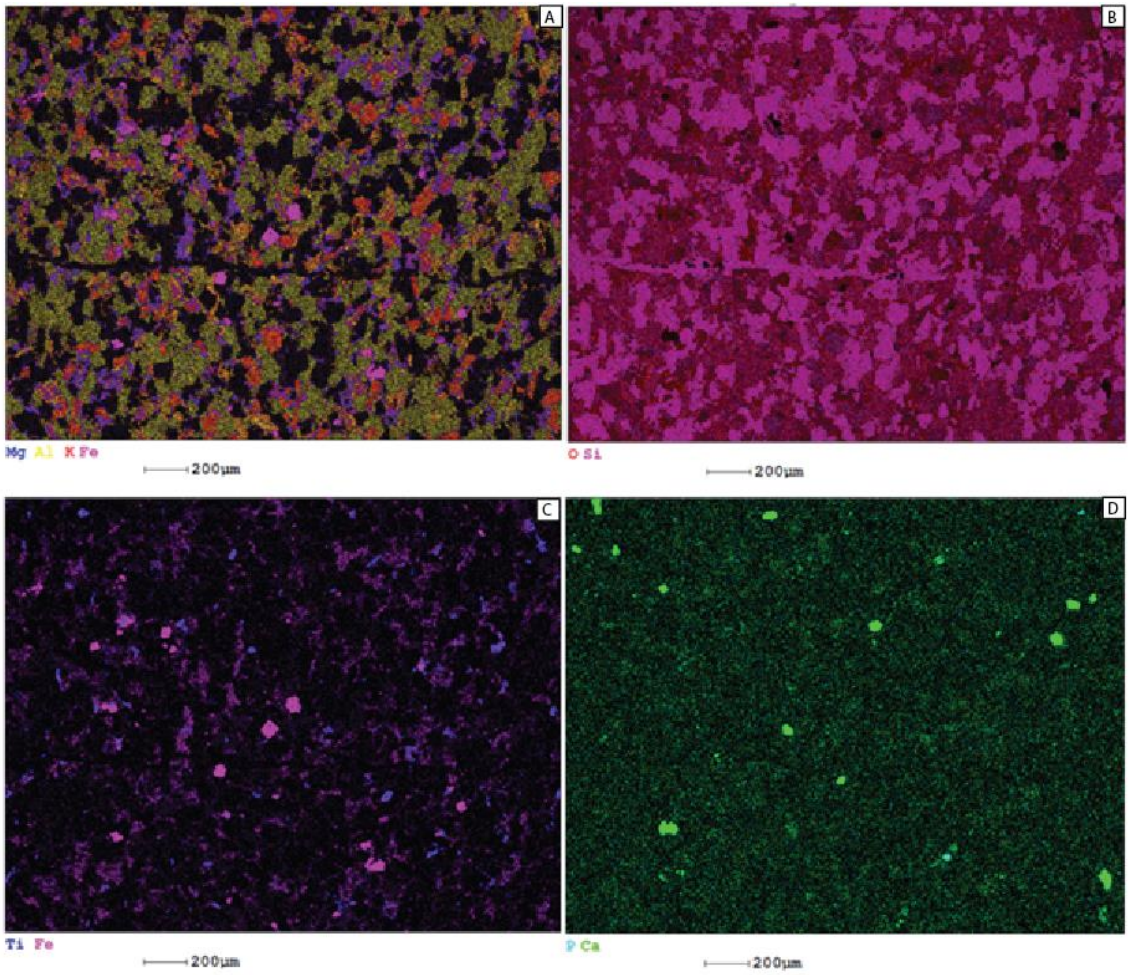

Figure 4.2: Examples of overlay maps used for point-counting. Note that Mg-Al-K-Fe maps (A) are used for identifying chlorite, mica, and orthoclase. The bright areas in Si-O maps (B) represent quartz. Ti-Fe maps(C) are used for distinguishing ilmenite from magnetite and rutile. P-Ca (D) maps represent areas that contain apatite.

CURVE FITTING

To describe and categorize the shapes of aperture profiles, I utilized a nonlinear least squares fit to solve for the equation that best fits each aperture profile. The basic equation for the solver was the superellipse or Lamé curve equation, which has the form

$$\left|\frac{x}{a}\right|^n + \left|\frac{y}{b}\right|^n = 1\,, where\ 0 < b \leq a\,, n > 0 \quad \text{(Weisstein, 2016)}$$

The variable a is half the fracture height in vertical fracture aperture transects, or half the fracture length in horizontal transects, b is half the maximum kinematic fracture aperture measured perpendicular to the fracture medial plane of symmetry from wall rock-cement interface to the same interface of the opposing fracture face, x is the distance along the height or length transect, and y is half the kinematic aperture of the fracture at position x. The shape of the Lamé curve or the aperture profile is controlled by the n-value. When n < 1, the Lamé function has a concave or inward-curved shape. The function has a linear shape when n = 1, and an elliptical shape when the n = 2. For n > 2, the curve becomes more convex, giving the fracture the shape of a rectangle with rounded corners at large n (Figure 4.3).

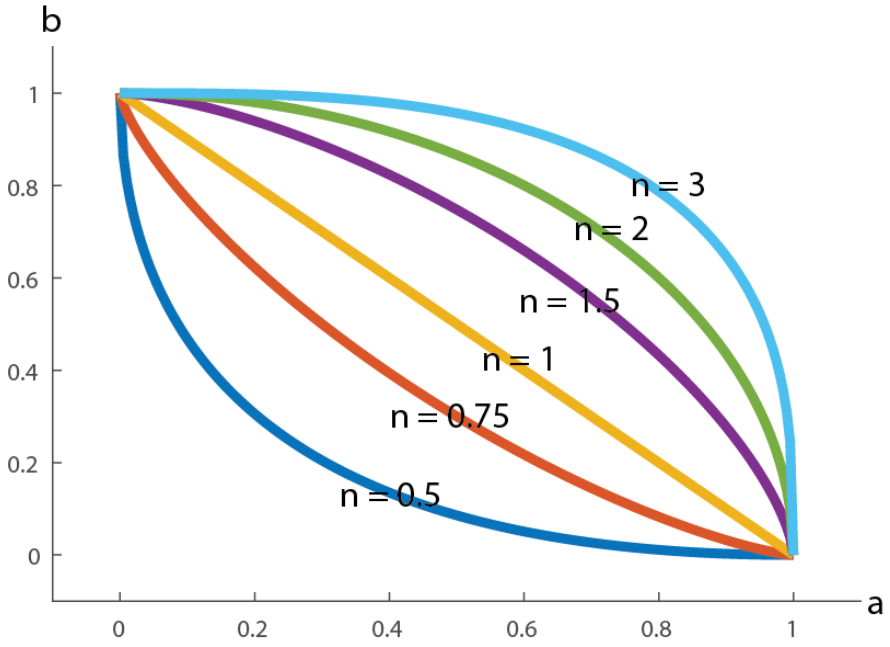

Figure 4.3: Shapes of the Lamé function at various n-values with a = 1 and b = 1.

The analysis was performed for the entire aperture profile from tip to tip, and separately for the two tip regions because fractures are not symmetric in shape. The two tip regions are 1) the portion of the fracture where the aperture displays an increasing trend (top tip), and 2) where the aperture displays a decreasing trend (bottom tip). I used a moving average analysis to determine the location of maximum aperture along the aperture profiles prior to separating each fracture. The separation of the top and bottom regions results in 82 half-fracture aperture profiles, including 56 from field measurements, 14 from hand samples, and 12 from thin sections. I solved for the values of a, b and n that yielded the lowest R^2 values in Matlab on the unsmoothed aperture data using the built-in nonlinear least-squares solver with the Trust-Region-Reflective algorithm.

FLUID INCLUSION MICROTHERMOMETRY

Fluid Inclusion Microthermometry Background

Origins of Fluid Inclusions

The crystals that precipitate from fluids tend to trap fluids inside vacuoles that form from growth imperfections (Goldstein and Reynold, 1994). Fluids trapped at the time of mineral precipitation are primary fluid inclusions, which record temperature, pressure, and composition of the fluids during cementation. In quartz, primary fluid inclusions within quartz cement usually align along concentric growth zones due to increments of quartz precipitations or growth defects (Guscott and Burley, 1993).

Assumptions of the technique

Fluid inclusion microthermometry assumes that the host mineral, quartz in this study, is impermeable to chemical changes after inclusion entrapment, and that an inclusion represents a chemically closed system. The volume and density of each inclusion are also constant representing an isochoric system.

The phase changes of a unary system of pure H_2O, where fluid inclusion volume is constant throughout its history, are shown in Figure 4.4.

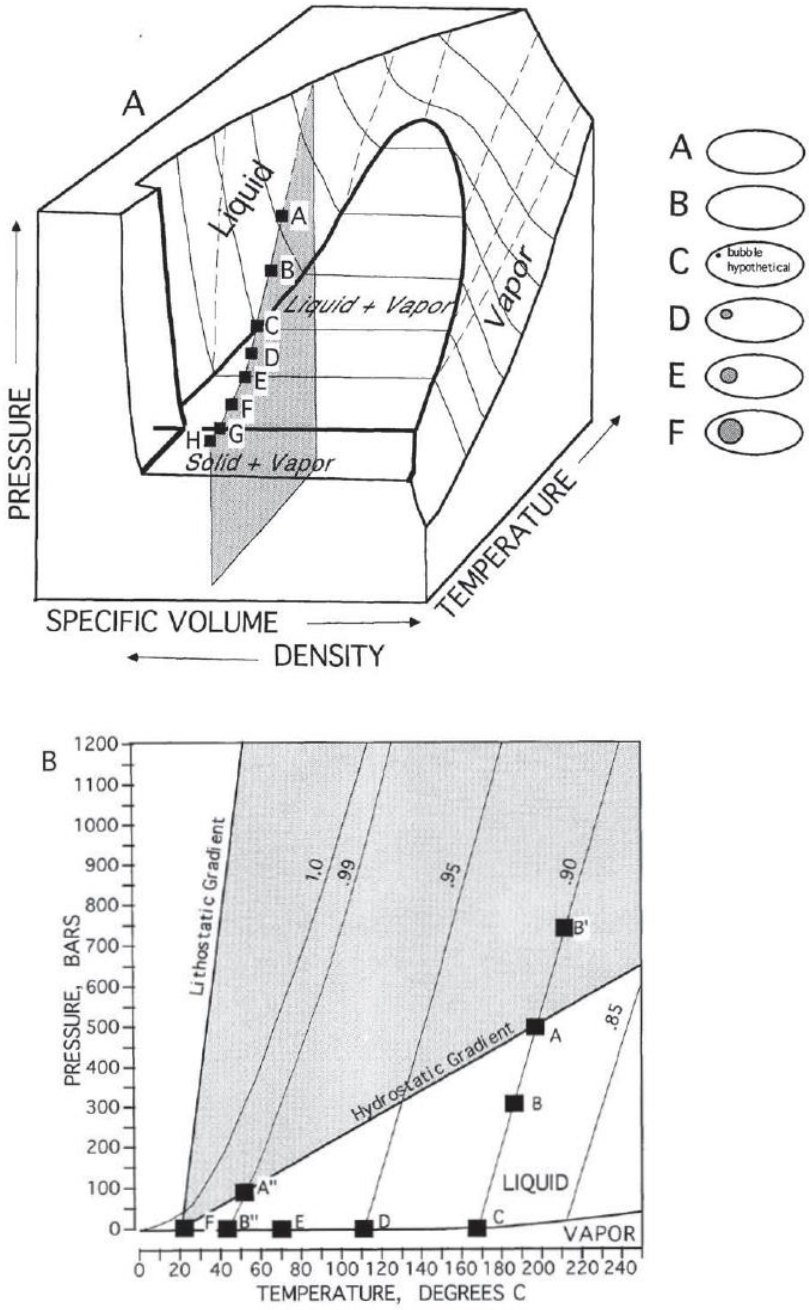

Figure 4.4: A) The P-T-V diagram of the unary system H_2O, showing an example of an inclusion with a constant volume (shaded in gray and shown in B), which originally contains a single phase fluid (liquid). As the temperature decreases to the liquid-vapor point, a small bubble forms. The bubble increases in size with decreasing temperature.

The pressure within the inclusion depends on the density and temperature of the inclusion. Since the density is constant, the pressure inside an inclusion is controlled by temperature. The temperature of an inclusion is externally controlled. When the temperature is high (at point A and B in Figure 4.4) the pressure is also high, and the inclusion is only in liquid phase. When temperature decreases during exhumation to point C, the system intersects the liquid-vapor curve and a minuscule vapor bubble forms in the inclusion. As the cooling continues, the inclusion cools from point C to F, the volume of vapor grows in proportion to the volume of liquid, and the internal pressure gradually falls.

If the temperature is increased again, for instance in the heating stage of the fluid inclusion microscope, the system will move back along the same line from point F, and when it reaches point C the bubble will disappear. The temperature at which the bubble disappears, or the temperature at which the inclusions becomes a single-phase fluid, is called the homogenization temperature. The homogenization temperature, measured by fluid inclusion microthermometry, provides a minimal estimate of temperature of trapping.

The technique of cycling

The technique of cycling employs the inherent metastability of homogenized liquid. Fluid inclusion temperatures generally have to be several tens of degrees below the homogenization temperature to instigate bubble nucleation (Goldstein and Reynold, 1994; Fall et al., 2012). When the temperature is lower than the homogenization temperature, its internal pressure would follow a metastable isochore line to a point below the liquid-vapor field boundary. The liquid is under tension (stretched liquid), and the inclusion's internal pressure at this point is less than zero. As the fluid inclusion continues to cool to point B in Figure 4.5, the drive for the stretched liquid to separate from the wall of the inclusion is high enough that the

stretch liquid finally detaches from the wall to form a spherical bubble. If one were viewing an inclusion at the instant this happens, one would see a vapor bubble instantly pop into view. At this point, the inclusion conditions return to the liquid-vapor phase (Point C in Figure 4.5), which is an equilibrium point.

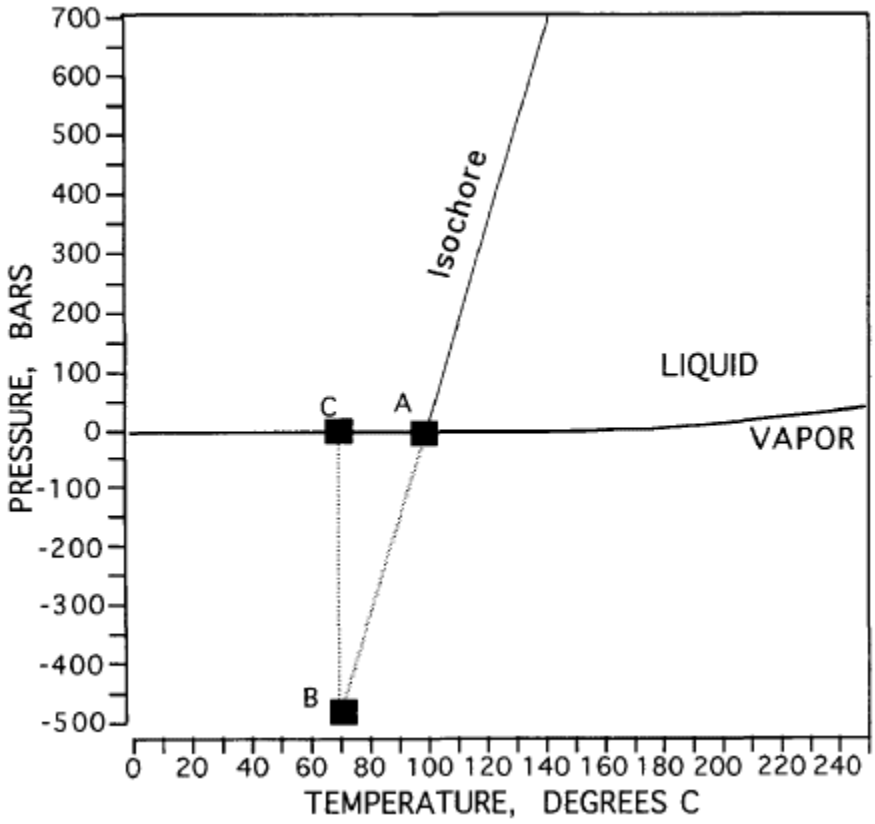

Figure 4.5: Pressure-temperature phase diagram of pure water showing the undercooling required for a bubble to reappear. At point A, the inclusion is homogenized. Then, it has been cooled, and the bubble will not nucleate immediately. At point B, the pressure in the inclusion drops to a negative value. When the inclusion has been cooled enough, the stretch liquid finally detaches from the wall to form a spherical bubble, and the inclusion returns to the equilibrium point on the liquid-vapor curve at point C. (From Goldstein and Reynold, 1994)

For aqueous inclusions that require undercooling by tens of degrees, the cycling technique provides an effective and accurate method for determining homogenization temperatures. Figure 4.6 demonstrates how the cycling technique is done. The bubble gradually

becomes smaller after it has been heated up from room temperature. The small bubble is still present at 125°C. At 130°C, it appears to an observer that the bubble has completely disappeared. The observer then stops heating the stage. When the temperature drops to 125°C, the bubble immediately reappears, suggesting that undercooling was not required to generate the vapor. This indicates that the bubble was still present, but not visible, to the observer at 130°C. The observer then heats up the stage to a higher temperature again and lets the stage cool down until the bubble doesn't appear at 125°C. In this example, the homogenization temperature is between 135°C and 140°C since the bubble appears at 125°C after it has been cooled down from 135°C, but does not appear after it has been cooled down from 140°C. The metastable phenomenon does not occur when the inclusion has not yet been homogenized. However, when the homogenization temperature is reached, the inclusion has to be undercooled (to 80°C in this example) to overcome fluid metastability in order for the bubble to renucleate. The cycling technique is usually applied as explained above, but with smaller intervals.

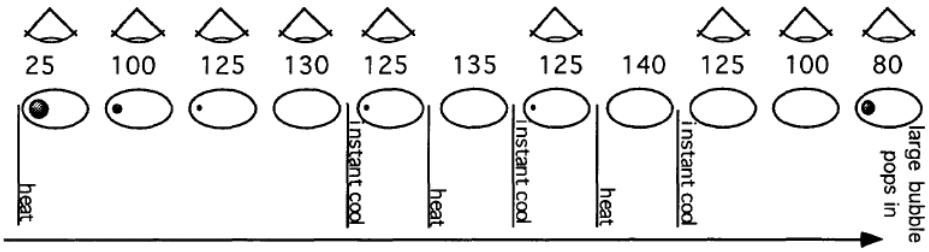

Figure 4.6: Schematic example of behavior of an inclusion during cycling. The inclusion is homogenized at 140°C, indicated by the absence of a bubble after the inclusion has been cooled. When the temperature dropped to 80°C, which is much lower than the temperature of 125°C that the bubble used to present at, the bubble renucleated. In this example, the homogenization temperate is between 135 and 140°C. (From Goldstein and Reynold, 1994)

DETAILS ON THE APPLIED FLUID INCLUSION MICROTHERMOMETRY IN THIS STUDY

To test for variation of fracture aperture profile as a function of temperature at the time of fracture formation, I determined fluid inclusion homogenization temperatures of fracture cement. Samples for analysis were impregnated with blue epoxy, and doubly polished to 50 – 60 μm-thick thin sections under a temperature less than 60°C. I studied inclusions in quartz-cement, preferably on cement bridges with crack-seal texture. Bridges are isolated areas of cement that connect fracture walls. Most of them resulted from quartz cement growing along the c-crystallographic axis of a quartz grain that is orientated approximately perpendicular to fracture walls (Laubach et al., 2004; Becker et al., 2010). Crack-seal texture is indicative of multiple stages alternating between brittle fracture opening and cementation and indicates that the fracture cement formed during and synkinematically with fracture opening. Fluid inclusion temperatures measured of crack-seal cement thus reflect the temperature conditions during fracture opening.

Along the bridges, I looked for fluid inclusion assemblages (FIAs), which are trails of primary inclusions that are parallel to the fracture walls. Each FIA is a group of fluid that has been trapped when the cement growing from each wall into the fracture gap connects, preserving a record of the composition, temperature, and pressure of the mineralizing environment (Goldstein and Reynolds, 1994). I determined liquid-vapor homogenization temperatures (the minimal estimate of temperature of trapping) using the thermal cycling technique with a temperature step of 1°C. Homogenization temperatures were collected for at least five different primary inclusions within a single FIA. The analysis was done on a Fluid, Inc.–adapted, USGS–type gas-flow heating-freezing stage that was connected to an Olympus BX51 microscope with a 40× objective lens and 15× oculars (Figure 4.7).

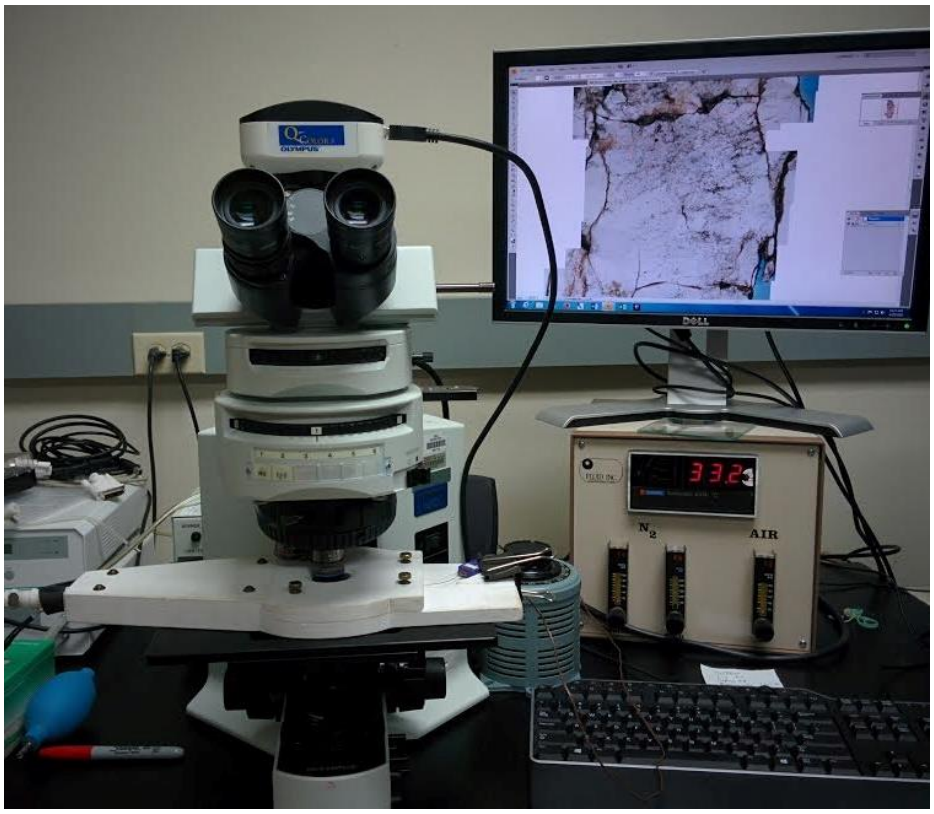

Figure 4.7: The Fluid, Inc.–adapted, USGS–type gas-flow heating-freezing stage with the Olympus BX51 microscope with a 40× objective lens and 15× oculars.

CHAPTER 5: FRACTURE APERTURE PROFILES AS INDICATORS OF FRACTURE GROWTH ENVIRONMENTS: AN INTEGRATED STUDY OF FRACTURE APERTURE GROWTH IN THE CAMPITO FORMATION OF EASTERN CALIFORNIA

INTRODUCTION

Processes of fracture formation control mechanical properties of the brittle crust and fluid flow in the subsurface (National Research Council, 1996). Opening-mode fractures, also referred to as extension or tension fractures, are observed as either barren joints or as partially or completely cemented veins that form isolated structures, clusters, or connected fracture and fault systems. Numerous studies have quantified aperture, length, and spatial arrangement of opening-mode fractures (Snow, 1970; Olson, 2003; Olson, 2007; Gomez, 2007; Sakaguchi et al., 2008). Because volumetric flux is a function of the cube of aperture for open fractures (Walsh, 1981; Tsang and Witherspoon, 1981; Klimczak et al., 2010), aperture size and size distribution have been quantified in several studies (Bonnet et al., 2001; Gale et al.,2007; Hooker et al., 2009; Hooker et al., 2013). Few studies, however, have investigated the aperture distribution or aperture profile along the trace of single fractures (Pollard and Segall, 1987; Gudmundsson, 1987; Vermilye and Scholz, 1995; Gudmundsson et al., 2012). An aperture profile describes the width or opening displacement of a fracture in two dimensions along a fracture length or height transect. Aperture profiles of opening mode fractures in homogeneous, linearly elastic, and isotropic materials subject to a uniform fluid pressure and a uniform external driving stress are elliptical in shape and are given by

$$u(x) = \pm\Delta\sigma_I \frac{(1-\nu)}{\mu}\sqrt{a^2 - x^2} + \Delta\sigma_{II}\frac{(1-2\nu)x}{2\mu}$$

(Equation 8.34 in Pollard and Segall, 1987), where u(x) is the displacement at position x along the length of fracture, $\Delta\sigma_I$ and $\Delta\sigma_{II}$ are the driving stress in mode I and mode II fractures, respectively, a is half the fracture length or, for a vertical fracture, height, ν is Poisson's ratio, and μ is Young's modulus. The $\pm$ sign with the first term refers to the upper wall at $x_1 = 0^+$ and the lower wall at $x_1 = 0^-$. The elliptical aperture profile thus reflects the correspondence between displacement and stress following an elliptical function along the length or height of a fracture (Sneddon, 1946; Geertsma and Klerk, 1969; Engelder et al., 1993; Gudmundsson, 2011). Similar aperture profiles are expected for fractures in viscoelastic materials under small-scale yielding conditions (Bradley et al., 1998; Broberg, 1999).

Both field observations and numerical models have shown that the shapes of aperture profiles are approximately elliptical. Pollard and Segall (1987) asserted that the shape of a dilation profile of a basaltic dike segment near Ship Rock can be adequately described by the elliptical displacement equation mentioned above. Gudmundsson (2011, p. 389) concluded that displacements of many fractures along their length can be approximated by an elliptical function based on aperture profiles for mineral-filled vein in gneiss in West Norway.

However, multiples studies have also shown deviations of aperture profiles of natural fractures from the theoretical elliptical shape. Pollard and Segall (1987) observed departures in aperture profile from a perfect ellipse for a basaltic dike and attributed this departure to wall rock brecciation, wall rock erosion, and the elastic interaction with neighboring dike segments. Delaney and Pollard (1981) demonstrated that interaction between two closely spaced parallel en-echelon fractures causes local deficits in opening displacement in the tip region whereas the opening displacement of two collinear closely spaced fractures causes a slightly larger opening

displacements in the tip regions, resulting in blunting of fracture tips relative to isolated fractures in the same material. Deviations from elliptical aperture profiles observed in dikes and veins were attributed to heterogeneous fluid pressure distributions within the fractures or variation in hostrock elastic properties along the fracture trace (Gudmundsson et al., 2012; Kusumoto et al., 2013). Vermilye and Scholz (1995) presented aperture profiles of fractures from Culpeper Quarry and Florence Lake with linearly tapered tips that they attributed to inelastic deformation.

Temperature, chemical reactions, material anisotropy across layer interfaces, and fluid pressure variation can affect fracture propagation (Atkinson, 1984; Atkinson and Meredith, 1981; Helgeson, and Aydin, 1991; Cooke and Underwood, 2001; Nara et al., 2006; Gudmundsson et al., 2012). Non elastic fracture growth can cause deviation of fracture shapes from those of elastic fractures. Eichhubl and Aydin (2003) and Eichhubl (2004) observed fractures of high aperture to length ratios in reactive combustion-metamorphic diagenetic environments, suggesting that solution mass transfer allows fracture growth through inelastic deformation mechanisms. A recent study on cemented fractures in deeply buried sandstone in East Texas has also identified non-linear fracture growth, in which a period of fast fracture growth in length relative to aperture growth is followed by a period of a slow propagation and faster aperture growth accommodated by solution-precipitation creep (Alzayer et al., 2015). Although the previous studies demonstrated that various factors affect fracture shapes, aperture profiles were not measured in these studies to assess if non-elastic fracture growth processes affect fracture aperture profiles.

In this study, I measured aperture profiles of cemented opening-mode fractures or veins in low-grade metamorphic silt- and sandstone of the Campito Formation, White Mountains, CA, to test if aperture profiles reflect fracture growth conditions and mechanisms. Specifically, I

tested the hypothesis that aperture profiles of fractures growing in different environments and following different mechanisms will have different degrees of ellipticity in opening displacement. I applied a nonlinear least squares fitting method to fit a superellipse or Lamé curve to each aperture profile. I then compared the Lamé parameter n of the fracture profile against structural and inferred environmental parameters that may control fracture growth.

I will present data of fractures, with the Lamé parameter n varying between 0.7 and 3.2, indicating that the shapes of aperture profiles vary from close to triangular to box-shaped. Based on a new conceptual model of incremental fracture growth, I will demonstrate that the range of observed n values reflects the effect of temperature on fracture properties and solution-precipitation creep suggesting that fracture aperture profiles are diagnostic of fracture growth conditions and mechanisms.

GEOLOGIC BACKGROUND

The Cambrian Campito Formation exposed in the White-Inyo Range along the border of California and Nevada (Figure 5.1) is composed of low-grade metamorphic siltstone and sandstone deposited in a tidal environment (Nelson et al., 1991 and Moore and Fritsche, 1976). It is part of a succession of Neoproterozoic to Upper Cambrian sedimentary rocks that have been deformed into a series of NE-trending folds as a result of the Devonian to Mississippian Antler orogeny (Bateman, 1992; Stevens et al., 1997 and Morgan and Law, 1998). During the Permian-Triassic period, movement on the Last Chance thrust formed the large-scale N-trending and NW-trending anticlines that define the White and Inyo Mountains (Corbett et al., 1988; Morgan and Law, 1998). Middle-to-Late Mesozoic intrusive rocks metamorphosed the sedimentary rocks to the slate, schist, and quartzite that I observed in this study (Nelson et al., 1991). The Late Cretaceous Birch Creek pluton (Barton, 2000), located approximately 5 km NE of the study site on the east flank of the White Mountains anticline was episodically emplaced from at least two distinct magma sources (Barton, 2000).

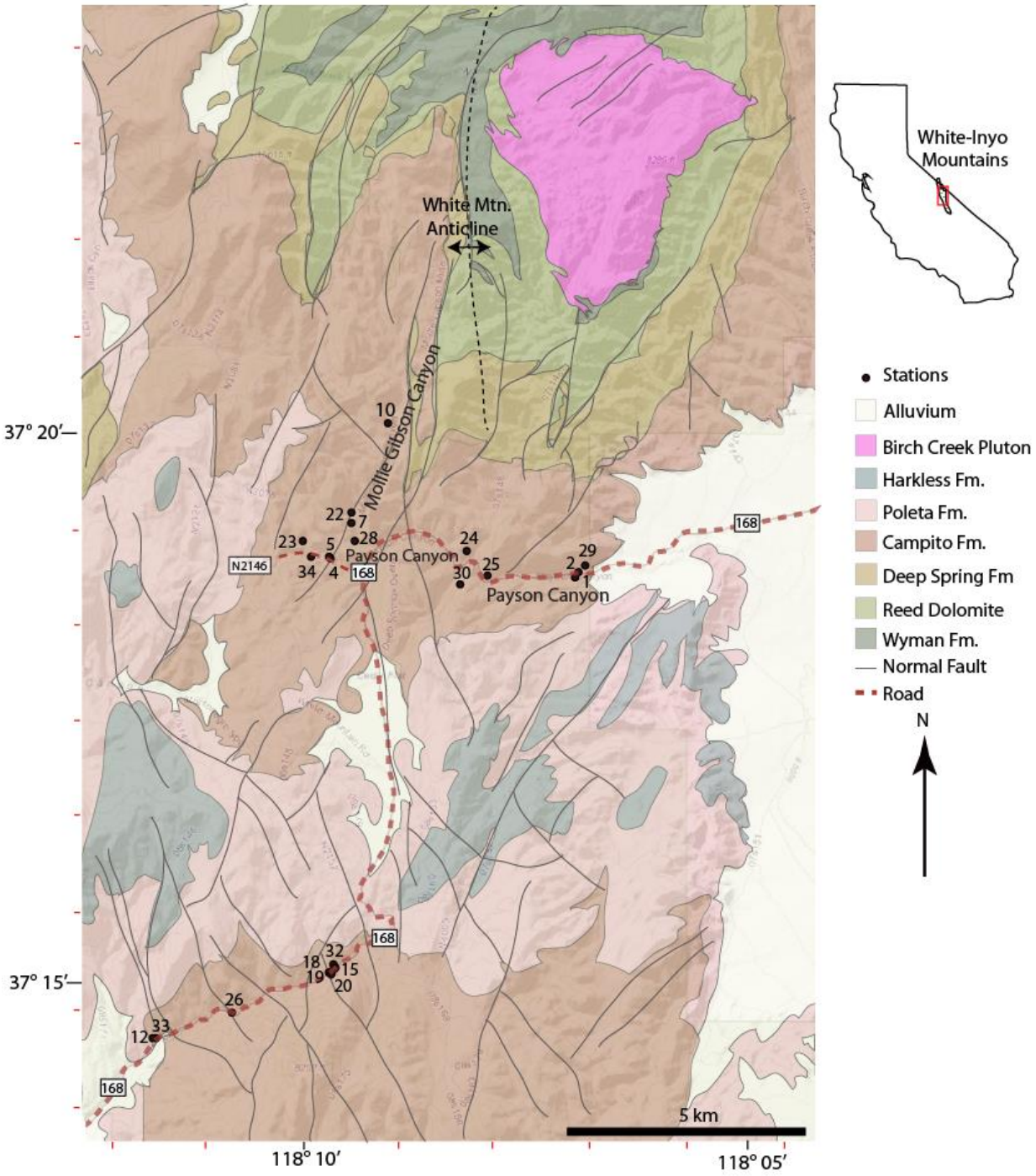

Figure 5.1: Locations of the field stations. The northern stations are closer to the White Mountain Anticline, while the southern stations are further south along the CA-168 highway.

METHODS

Fracture Aperture Profile Data Collection

I collected 38 fracture aperture profiles and 27 hand samples at 34 field locations. The field locations are divided into northern and southern stations. The northern stations are approximately 5 km east of the White Mountains anticline and south of the Birch Creek pluton, and they are in various locations including 1) along Hwy CA-168 in Payson Canyon east of Westgard Pass, 2) in Mollie Gibson Canyon, and 3) along National Forest Road N2121. The southern locations are located on the western limb of the anticline along Hwy CA-168 (Figure 5.1).

Aperture profiles were collected in the field for fractures that expose at least one, but preferentially both tips using a hand lens, a caliper, and measuring tape. All but three fractures were exposed on near-vertical rock faces providing aperture profiles along the fracture height, with exposure conditions limiting the number of profiles along fracture length. The caliper was placed perpendicular to the fracture wall to obtain true opening displacement for fractures oriented obliquely to the exposure. Taking measurements with caliper and handlens allowed measurements of apertures as small as 1 mm with a precision of 0.1 mm. Exposures were selected to provide profiles of fractures oriented roughly perpendicular to the outcrop face. I chose fractures that are partially or completely filled with cement to investigate the correlation between textures of cement and fracture ellipticity. To capture the change in aperture close to the fracture tips, I collected data at a 1 mm interval for approximately 20 mm from each fracture tip, and at 2 mm and 5 mm intervals after 20 mm and 50 mm from the tip, respectively. For all measured fractures I documented 1) orientation, 2) textural characteristics and compositions of fracture cement, 3) shape of fracture tips, 4) locations of fracture tips relative to layer boundaries, and 5) shapes of fracture tips. I also noted the presence of nearby fractures. To evaluate if

fracture shape is affected by lithologic boundaries I distinguished fracture tips that are located within 1 cm of a layer boundary from fracture tips located more than 1 cm away from a layer boundary. Because lithologic layer boundaries can be gradational and fracture tips are difficult to define with a precision of <1-5 mm, I chose 1 cm from a layer boundary as our classification distance. I also recorded if fractures are contained within one layer or cross lithologic layer boundaries.

Samples were collected for fracture aperture analysis in the lab with at least one preserved tip. 14 fracture aperture profiles were collected from nine hand samples using the same method as in the field. In addition, the same fractures were analyzed in thin section using transmitted light microscopy to determine textural characteristics and mineral compositions of fracture cement and host rock. I also measured an additional twelve micro-scale aperture profiles for fracture tips from thin section images using the measuring tool in Adobe Photoshop.

PETROGRAPHIC AND ENERGY-DISPERSIVE X-RAY SPECTROSCOPY (EDS) STUDY OF THE HOST ROCK

I determined textural characteristics and compositions of fracture cement and host rock in all of the thin sections using a petrographic microscope under plain and cross-polarized light. In addition, I performed energy-dispersive X-ray spectroscopy (EDS) analysis on a JEOL JSM-6490LV Scanning Electron Microscope to identify the mineral composition of the host rock. The spectral maps of the minerals in two thin sections made from the Campito Formation host rocks from two different outcrops were collected in Backscattered Electron (BSE) Shadow Mode in the EDEX Genesis program. I used these spectral maps to create multiple overlay maps, which I later used to conduct point-counting in JMicrovision to determine percentages of all minerals found in the thin sections.

CURVE FITTING

To describe and categorize the shapes of aperture profiles, I utilized a nonlinear least squares fit to solve for the equation that best fit each aperture profile. The basic equation for the solver was the superellipse or Lamé curve equation, which has the form

$$\left|\frac{x}{a}\right|^n + \left|\frac{y}{b}\right|^n = 1 \text{ , where } 0 < b \leq a \text{ , } n > 0 \text{ (Weisstein, 2016).}$$

The variable a is half the fracture height in vertical fracture aperture transects, or half the fracture length in horizontal transects, b is half the maximum kinematic fracture aperture measured perpendicular to the fracture medial plane of symmetry from the wall rock-cement interface to the same interface of the opposing fracture face, x is the distance along the height or length transect, and y is half the kinematic aperture of the fracture at position x. The shape of the Lamé curve or the aperture profile is controlled by the n-value. For n < 1, the Lamé function has a concave or inward-curved shape. The function has a linear shape when n = 1, and an elliptical shape when the n = 2. For n > 2, the curve becomes more convex, giving the fracture the shape of a rectangle with rounded corners at large n (Figure 5.2).

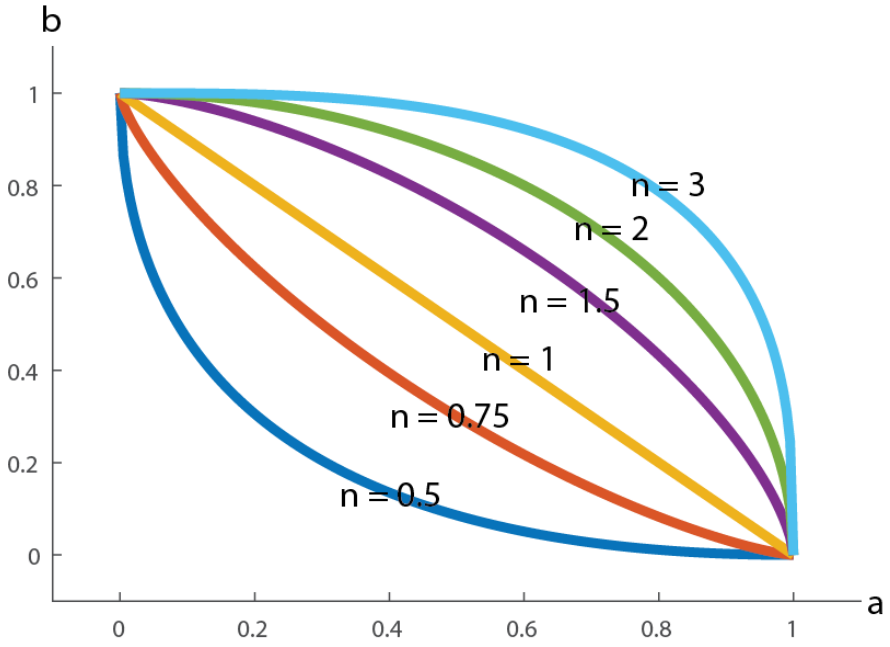

Figure 5.2: Shapes of the Lamé function at various n-values with a = 1 and b = 1

I solved for the values of a, b and n that yielded the lowest R^2 values in Matlab using the built-in nonlinear least-squares solver with the Trust-Region-Reflective algorithm. The analysis was performed for the entire aperture profile from tip to tip, and separately for the two tip regions to account for the asymmetry in fracture shape. The two tip regions were defined from the tip to the first aperture maximum after applying a moving average analysis to the aperture profiles. The separation of the tip regions resulted in 82 half-fracture aperture profiles, including 56 from field measurements, 14 from hand samples, and 12 from thin sections.

FLUID INCLUSION MICROTHERMOMETRY

To test for variation of fracture aperture profile as a function of temperature at the time of fracture formation, I determined fluid inclusion homogenization temperatures of fracture cement. Samples for analysis were impregnated with blue epoxy without exposing the sample to a temperature in excess of 60 °C and doubly polished to 50 – 60 mm-thick thin sections. I studied inclusions in quartz-cement, preferably on cement bridges with crack-seal texture. Bridges are isolated areas of cement that connect fracture walls (Figure 5.3A). Crack-seal texture is indicative of multiple stages alternating between brittle fracture opening and cementation. Along the bridges, I looked for fluid inclusion assemblages (FIAs), which are trails of primary inclusions that are parallel to the fracture walls (Figure 5.3B). Each FIA is a group of fluid that has been trapped when the cement growing from each wall into the fracture gap connects, preserving a record of the composition, temperature, and pressure of the mineralizing environment (Goldstein and Reynolds, 1994). I determined liquid-vapor homogenization temperatures (the minimal estimate of temperature of trapping) using the thermal cycling technique with a temperature step of 1°C. The cycling technique employs the metastability property of a homogenized fluid. An inclusion needs to be cooled down tens of degrees before the liquid detaches from the inclusion wall to form a spherical bubble after being heated up to homogenization temperature. Details on the technique are in Becker et al. (2010) and Fall et al. (2012). Homogenization temperatures were collected for at least five different primary inclusions within a single FIA. The analysis was done on a Fluid, Inc.–adapted, USGS–type gas-flow heating-freezing stage that was connected to an Olympus BX51 microscope with a 40× objective lens and 15× oculars.

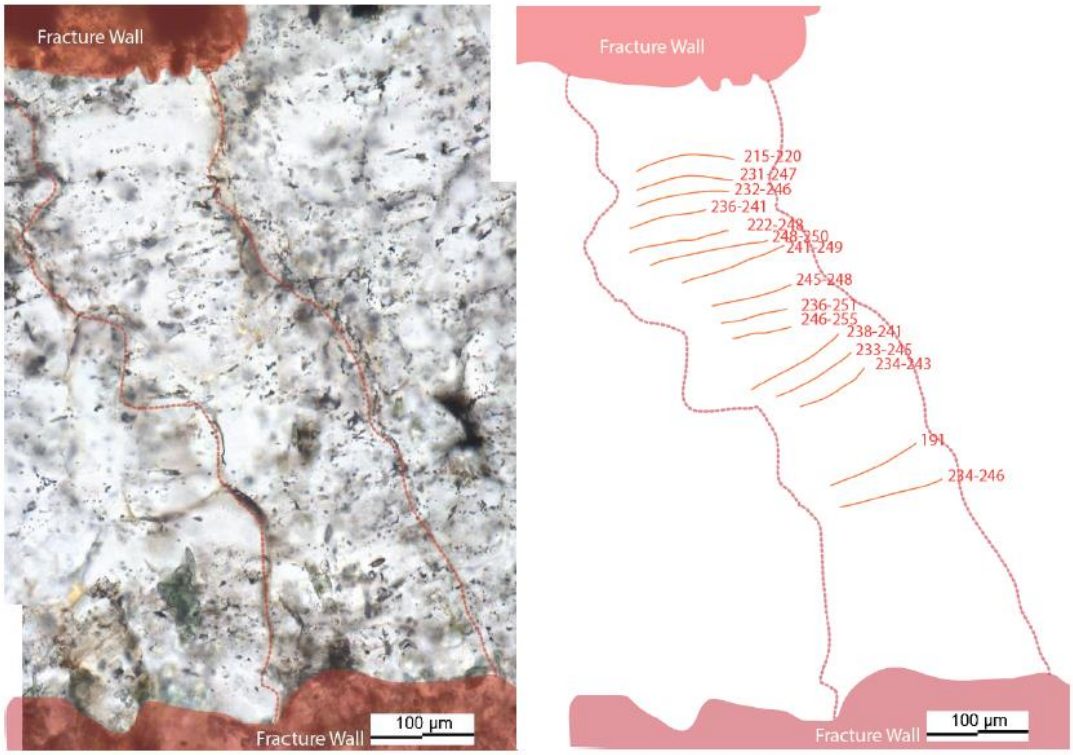

Figure 5.3: A. Transmitted-light photomicrograph of quartz fracture cement of fracture at station 4. Cement bridge is outlined. B. Tracing of bridge in A. with fluid inclusion assemblages (FIAs) indicated. Ranges of fluid inclusions homogenization temperatures given in degrees Centigrade.

RESULTS

Field observations of fracture aperture

The Campito Formation consists of fine-grained beige-to-gray low-grade metamorphic sandstone interbedded with gray siltstone (Figure 5.4A). All fractures analyzed in this study formed dominantly in opening mode as determined by the absence of discernible shear offset and linear trace in outcrop (Figure 5.4B). Fractures that are in close proximity to faults were not included in this analysis. Based on petrographic and EDS analysis, the sandstone is composed of 35% quartz, 27% chlorite, 27% mica, 6% orthoclase, 1% rutile, 1% magnetite, and less than 1% apatite and ilmenite.

The fractures are filled predominantly with quartz cement with small amounts of chlorite, calcite and trace amounts of rutile, magnetite, and ilmenite. Two prominent textural characteristics of the cement are blocky and crack-seal. The crack-seal texture resulted from episodes of fracture opening and cementation. Blocky cement, on the other hand, is post-kinematic. Both types of cement are present in both macro-scale fractures in the field and in hand samples, and in micro-scale fractures in thin sections (Figure 5.4C and Figure 5.4D). The textural characteristic of the cement of each fracture is carefully documented for later investigation of the relationship between the type of cement and the ellipticity of an aperture profile of the fracture. Overall, 58 aperture profiles belong to fractures with blocky cement, while only 24 of them belong to fractures with crack-seal cement.

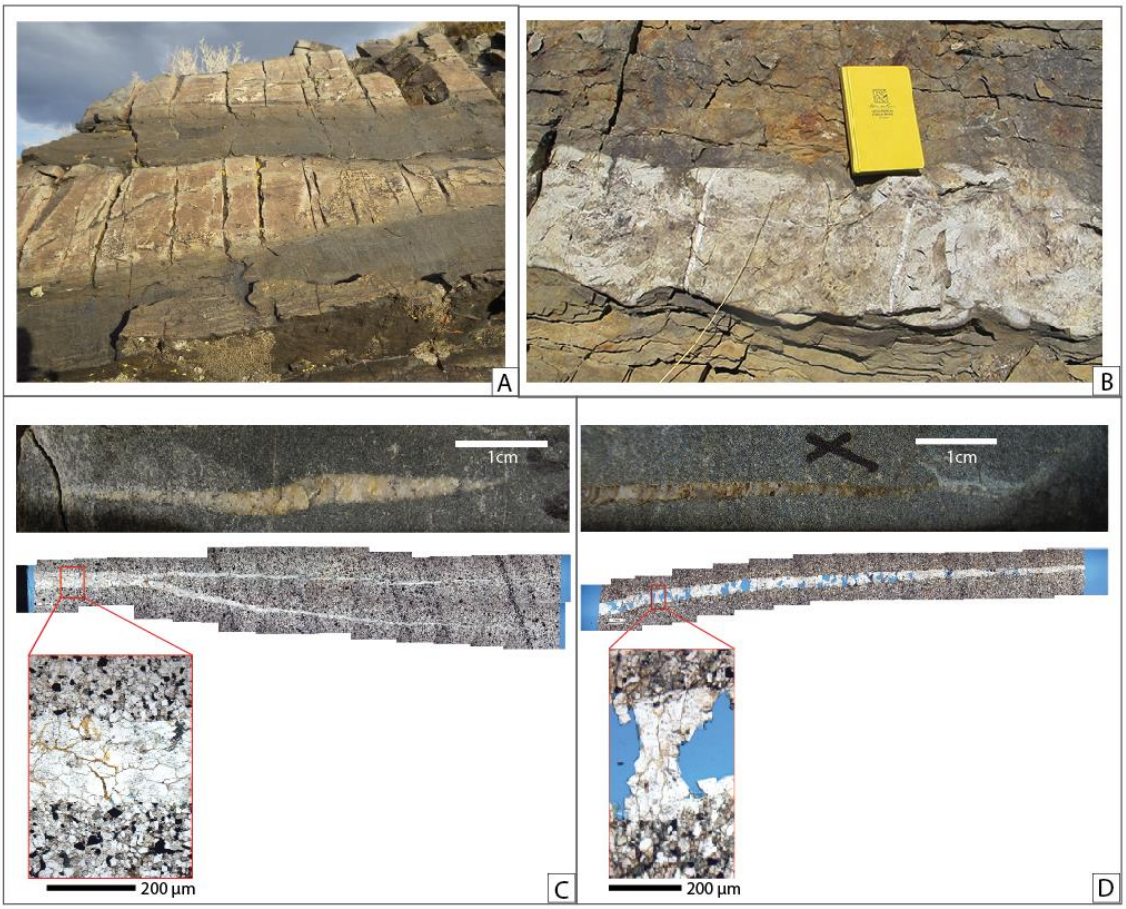

Figure 5.4: A) Campito Fm. outcrop next to Hwy 168 consists of fine-grained beige-to-gray low-grade metamorphic sandstone interbedded with gray siltstone; B) Example of fractures in this study. The fractures are all located in the metamorphosed sandstone. Two types of cement textural characteristics are blocky (C) and crack-seal (D), which I observed in both the macro scale and micro scale fractures.

I divided the fractures into three sets based on their strike orientations: Set 1 fractures strike in the NE-SW orientation, Set 2 fractures strike in the ENE-WSW direction, and Set 3 fractures strike in the SE-NW direction (Figure 5.5A and Figure 5.5B). 41 aperture profiles belong to the first set, while 24 and 17 aperture profiles belong to the second and the third sets, respectively. Set 2 fractures consistently cut and offset Set 1 fractures, indicating that Set 2

fractures are younger. I did not observe cross-cutting relationships between Set 3 fractures and fractures of the other sets.

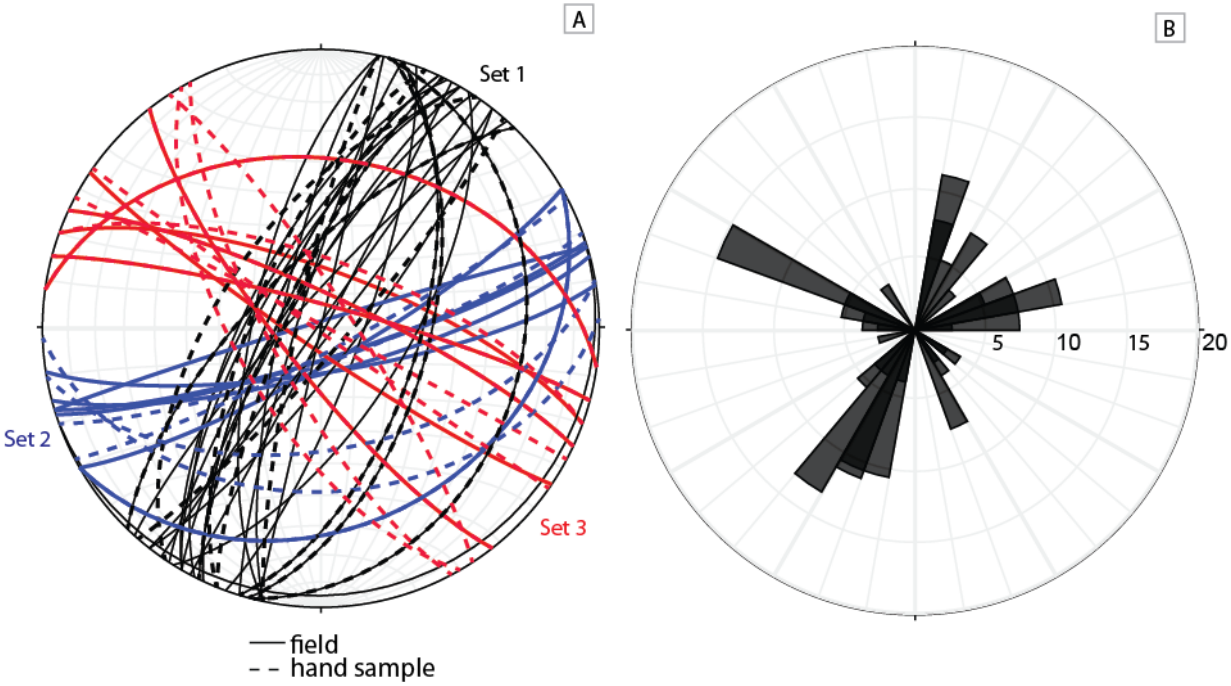

Figure 5.5: A) Stereonet (lower hemisphere) and B) Rose diagram representing orientations of the fractures studied in the field and on hand samples. Fractures are grouped into three principal sets based on their strike orientation: 1. NE-SW (black), 2) ENE-WSW direction (blue), and 3) SE-NW (red)

To study the effect of material discrepancies across layer interfaces on the shapes of aperture profiles, I compared aperture profiles of fractures with tips located at various distances from layer boundaries. I divided fracture tips into three groups based on their distances from layer boundaries. The tips of the first group end at less than 1 cm from layer boundaries. These tips are considered bed-bounded. The second group comprises tips that cut across layer boundaries, while the third group comprises fractures tips that end more than 1 cm away from

layer boundaries. Among the 56 fracture tips studied in the field, 20 are bed-bounded, 13 cut across layer boundaries, and 23 ended more than 1 cm from layer boundaries.

In order to investigate effects of interactions between fractures at fractures tips on the shapes of aperture profiles, I assigned fracture tips observed in outcrops and on hand samples into three groups: 1.) Isolated, single tips that are located more than half of their length away from other fracture tips (Figure 5.6A), 2.) Branching fractures: Their tips are separated into multiple smaller tips (Figure 5.6B), and 3.) Fracture tips that are in close proximity to another fracture (Figure 5.6C). Overall, 51 tips are isolated, 6 are branching, and 12 are located close to other fracture tips.

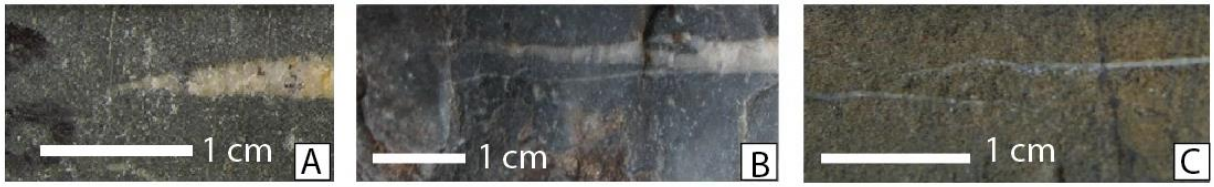

Figure 5.6: Three main characteristics of fracture tips: A) a sharp single tip, B) one tip branching into multiple smaller tips, and 3) a tip that is located close to another fracture

Fracture ellipticity analysis

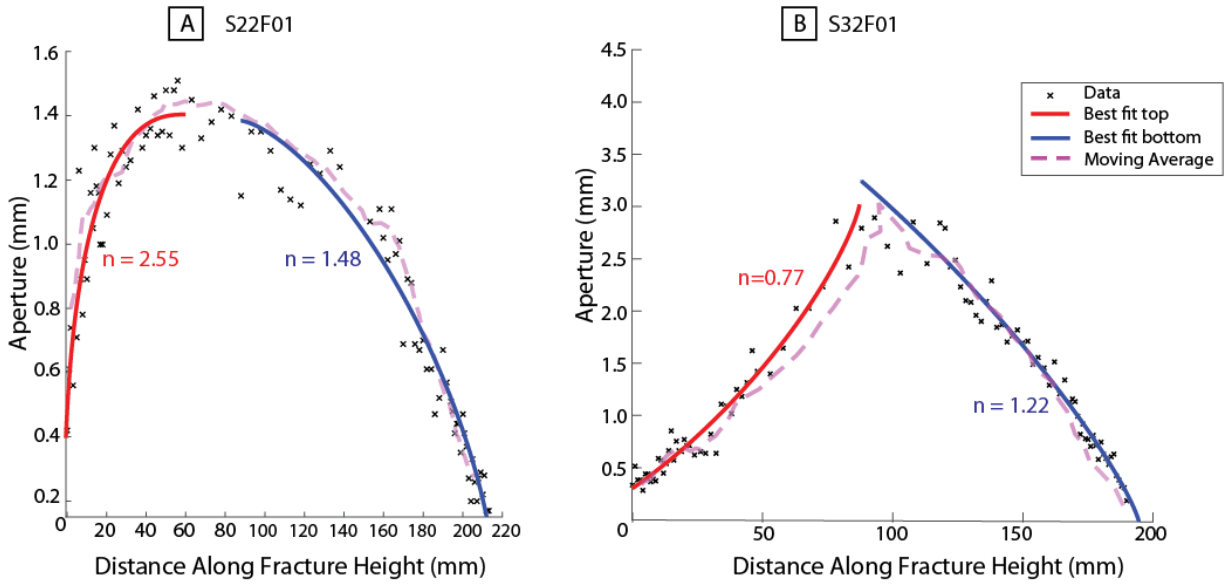

Figure 5.7: Aperture profiles of fracture S22F01 (A) and S32F01 (B). Trend lines are shown separately for the top and the bottom parts of the aperture profiles as separated by the maximum apertures in the smoothed aperture profile. The n-values of the top tip and the bottom tip of fracture S22F01 are 2.55, and 1.48, respectively. Fracture S32F01 has values of 0.77 and 1.22 for the top tip and the bottom tip, respectively. Distance is measured from the top to the bottom of the fracture trace.

The n-values of half of the fracture aperture profiles range from 0.72 to 3.20. N-values of the two tips can be different for the same fracture (Figure 5.7). For example, the n-value of the top of the aperture profile of fracture S22F01 (red segment of Figure 5.7A) is 2.55, while the n-value of the bottom aperture profile is 1.48 (blue segment).

A-values, which represent half of the fractures height, range from 14.14 mm to 528.11 mm (Figure 5.8A and Figure 5.14A). B-values, which represent maximum aperture, range between 0.611 mm to 25.62 mm (Figure 5.8B and Figure 5.14B). The ratio of b/a, which measures the flatness of an ellipse, scatters between 0.0048 and 0.93(Figure 5.8C and Figure 5.14C).

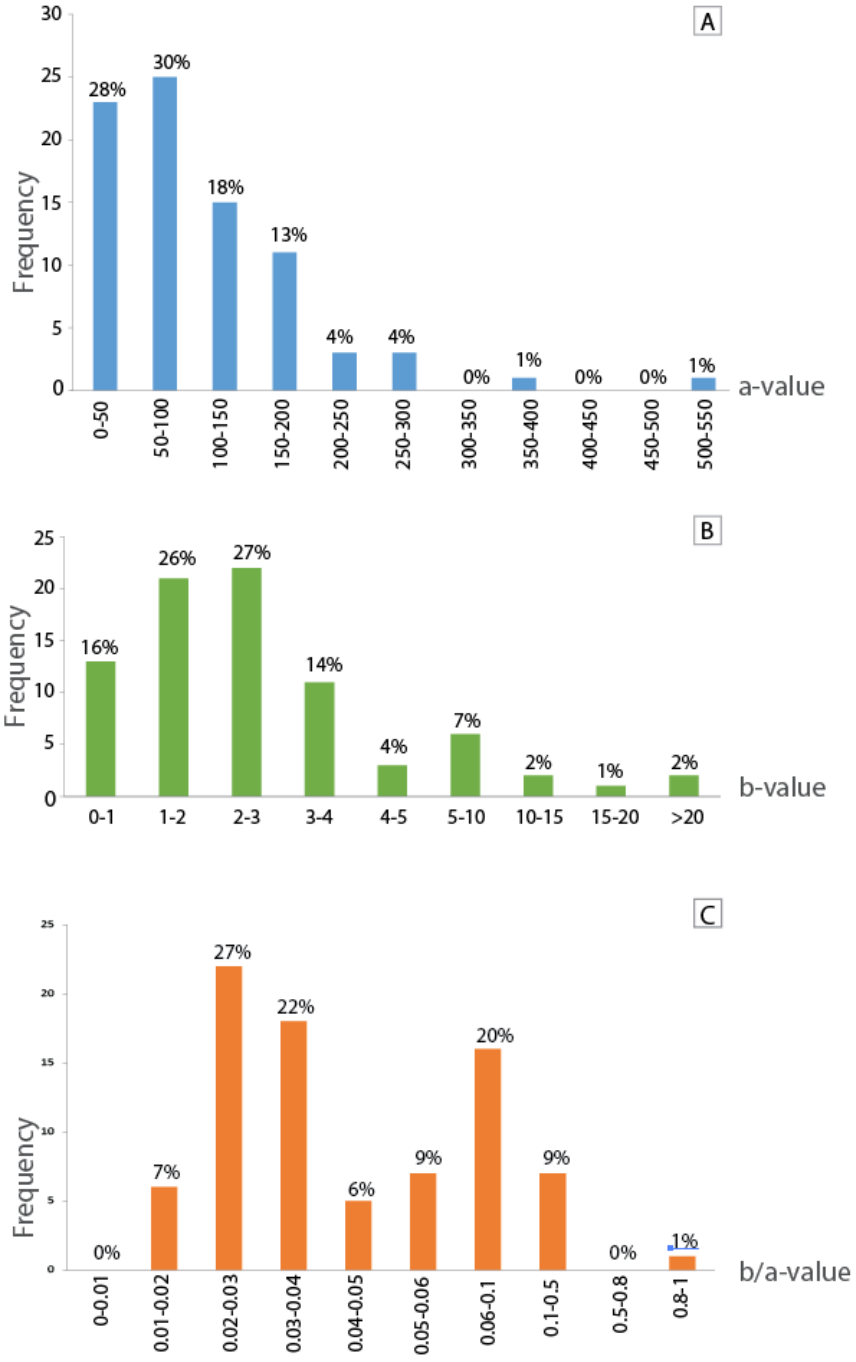

Figure 5.8: A) frequency and cumulative percentage of a-values (half of fracture height in mm); B) frequency and cumulative percentage of b-values (maximum aperture of fracture in mm); C) Frequency and cumulative percentage of b/a values.

Fluid inclusion microthermometry

Fluid inclusion homogenization temperatures were collected for quartz cement in six fractures, with at least two cement bridges from each fracture set to test for a correlation between fracture orientation, ellipticity, and homogenization temperature. Temperatures range between 148 and 315°C (Table 5.1).

Sample ID	Fracture set	a (mm)	b (mm)	n hand sample	n thin section	Temperature (°C)	
						min	max
ND05311522L	1	113.23	2.16	0.76	0.97	269	315
ND06031501T	1	112.37	1.80	1.39	1.50	191	268
cND0531151	2	56.31	3.11	1.98	2.01	198	262
ND05311521E	2	110.18	3.99	1.84	1.94	180	258
ND0608153M	3	248.19	1.92	2.08	2.07	148	254
cND06081506	3	102.73	2.53	1.44	1.33	270	314

Table 5.1: Summary of fluid inclusion microthermometric results

Each set of fractures contains temperatures from approximately 150°C to 300°C, which shows no correlation between temperature and fracture set. Set 1 fractures contain n-values ranging from 0.97 to 1.50, with the temperature ranging from 191 to 315°C. Set 2 fractures have n-values between 1.94 to 2.01, with the temperature between 180 and 262°C, while Set 3 fractures have n-values between 1.33 and 2.07, with the temperature between 148 and 314°C.

DISCUSSION

Correlation between Lamé parameter n and fracture properties

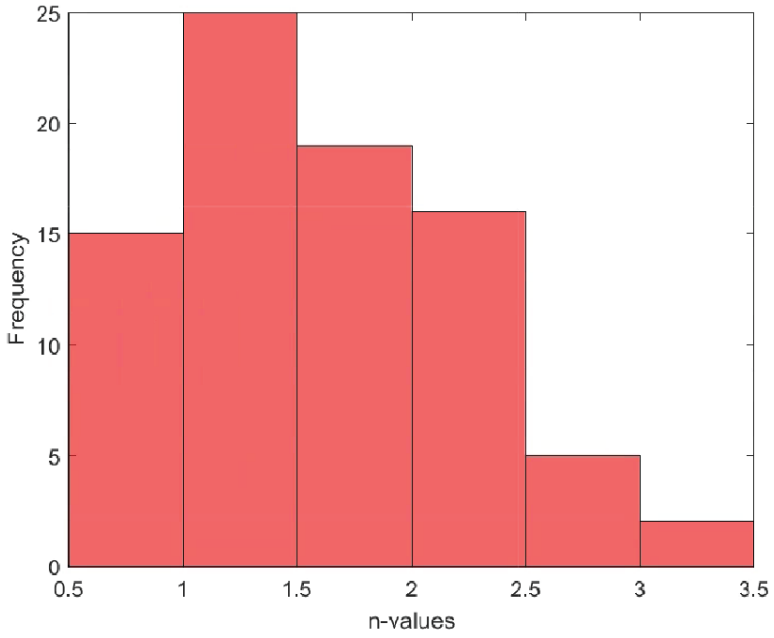

Figure 5.9: Histogram showing the distribution of Lamé parameter n of all of the aperture profiles

The Lamé parameters for the entire dataset extend over a large range from less than 1 to more than 3, corresponding to aperture profiles that range triangular-shaped to close to rectangular, with the majority of n-values falling between n = 1 and 1.5 (Figure 5.9). The range of the n-values, with the highest frequency in the $0.75 < n \leq 1.25$ interval, is similar for all three fracture sets (Figure 5.10**Error! Reference source not found.**). Because set 2 fractures predate set 1 fractures, these results indicate that ellipticity is not significantly controlled by the age of the fractures or the time of formation.

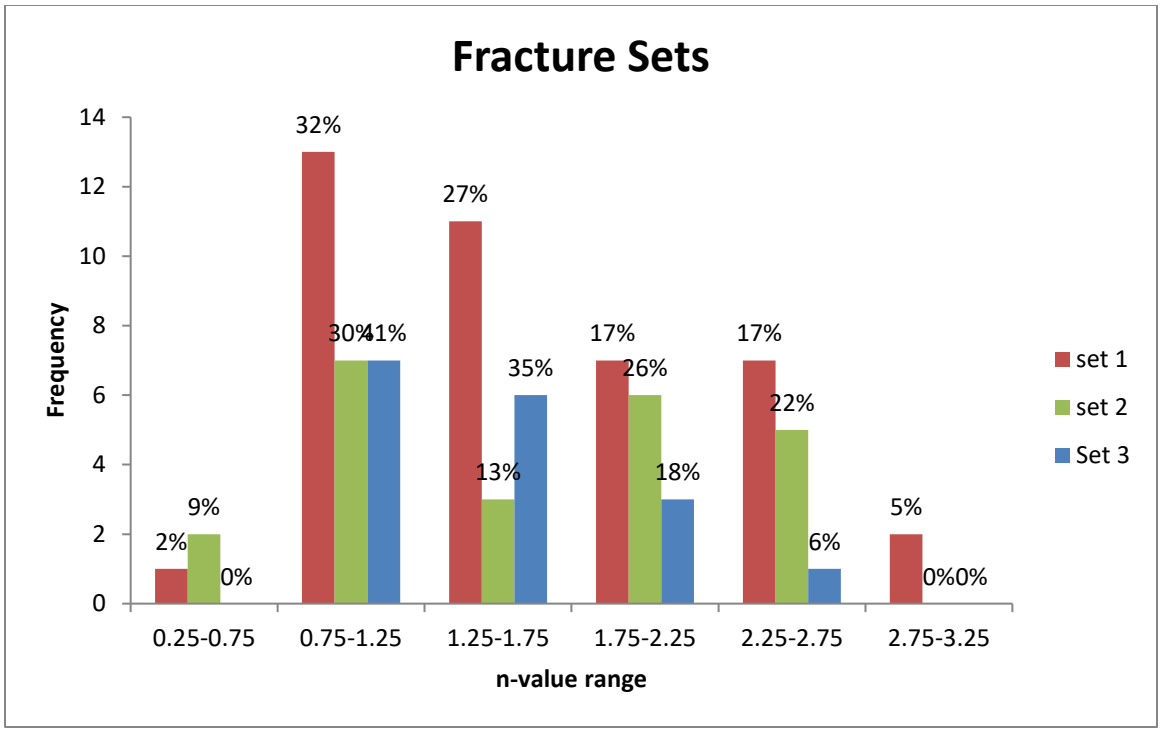

Figure 5.10: Histogram representing the distribution of the n-values of all fracture sets

The Lamé parameter n is not significantly different for fracture tips that are isolated, branching, or in close proximity to other fractures tips (Figure 5.11) suggesting that elastic interaction among closely spaced fractures has no discernible effect on fracture shape in our dataset. Isolated fracture tips make up 74% of all fracture tips that were analyzed, with n-values ranging between 0.72 and 3.09(Figure 5.11). While the n-values of branching fracture range between 0.84 and 1.55, the number of data is too small to test if the apparently narrower range in n compared to isolated tips is significant. Twelve tips are in close proximity to other fractures, with n-values between 0.97 and 3.2, similar to the range observed for isolated tips. The mode in n values of isolated tips between 2.25 and 2.75(Figure 5.11) suggests that close proximity may lead to more blunted fractures relative to isolated fracture tips.

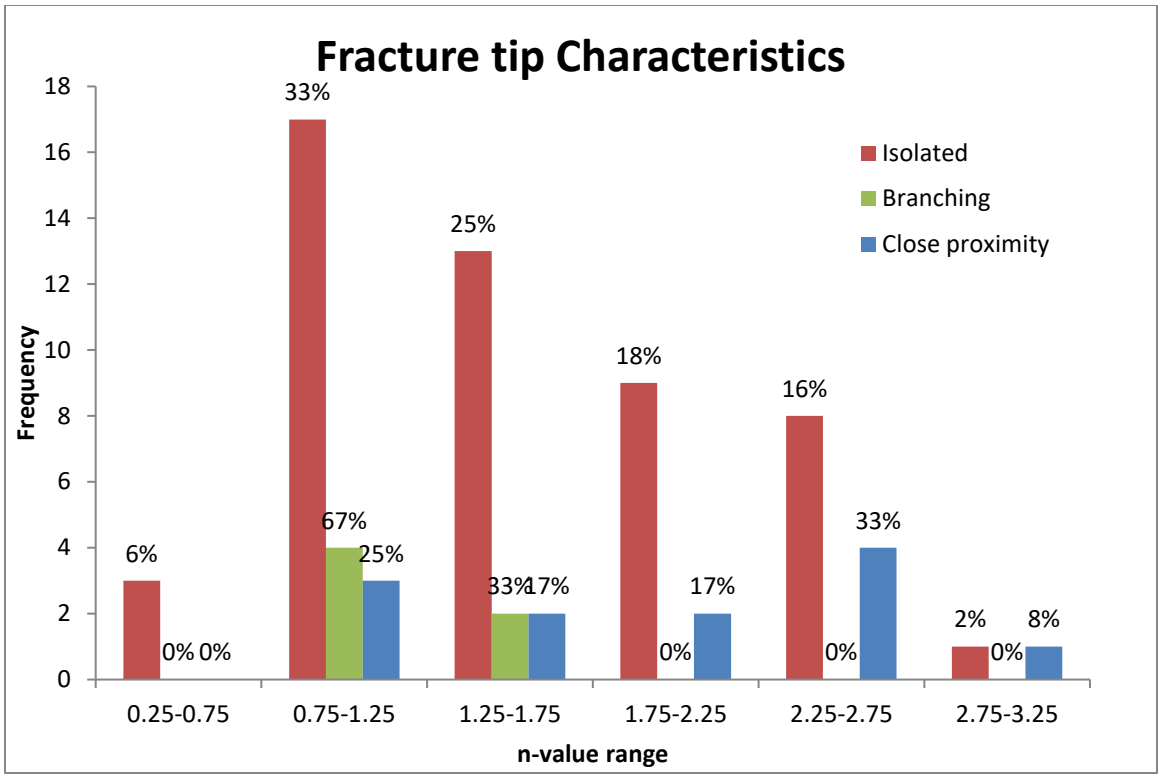

Figure 5.11: Histogram of n-values for fracture tips that are isolated, branching, and in close proximity with neighboring fracture tips.

The proximity of layer boundaries to fracture tips may lead to somewhat higher n values (Figure 5.12). The mode in n values of tips located >1 cm from layer boundaries is in the 0.75 to 1.25 range, whereas the mode for tips <1 cm is 1.25-1.75. The n-values of tips that are at more than 1 cm from layer boundaries display a wider range in n-values of 0.72 and 3.20 compared to tips within 1 cm of layer boundaries.

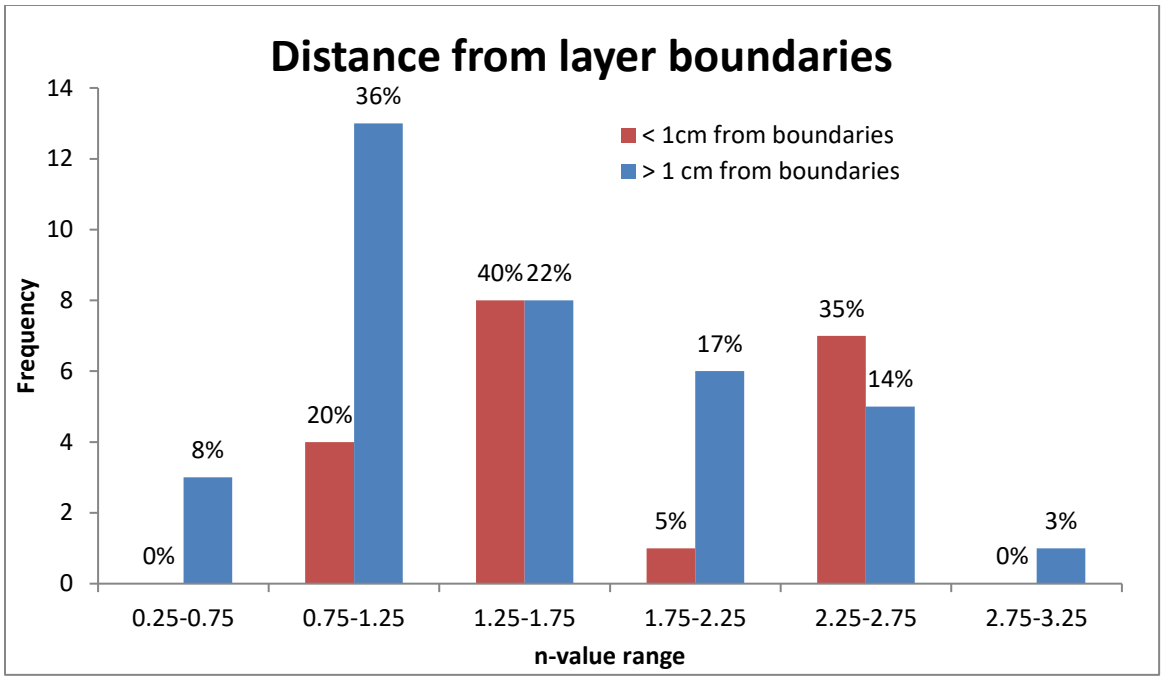

Figure 5.12: Histogram representing the distribution of the n-values in different ranges of fracture tips in the two categories of distance from layer boundaries

Fractures of low n contain preferentially blocky cement, with 81% of them having an n-value less than 2 (Figure 5.13). 50% of fractures with crack-seal texture n-value greater than 2, and none has an n-value less than 1. I conclude that conditions that lead to the formation of low-n fractures are not favorable for crack-seal cement precipitation whereas blocky cement growth occurs in fractures with n ranging over the entire range of observed values (0.72 to 3.20).

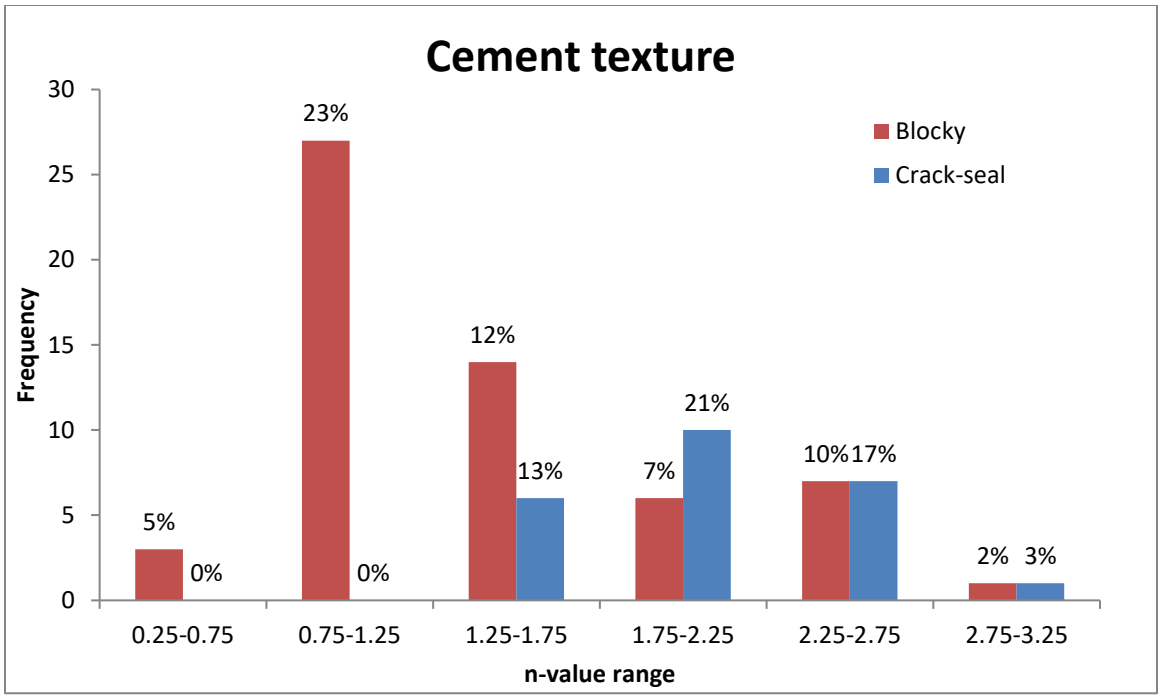

Figure 5.13: Histogram representing the distribution of the n-values of the two types of fracture cement characteristics

I do not observe a strong correlation between the half-heights of the fractures (a-values) and the n-values (Figure 5.8A and Figure 5.14A). A correlation between the b/a ratios and the n-values is also not present (Figure 5.8C and Figure 5.14C). However, I observe that fractures with b values larger than ~5 have n-values less than 2 (Figure 5.8B and Figure 5.14B). Thus, fractures that are wide tend to have low n-values.

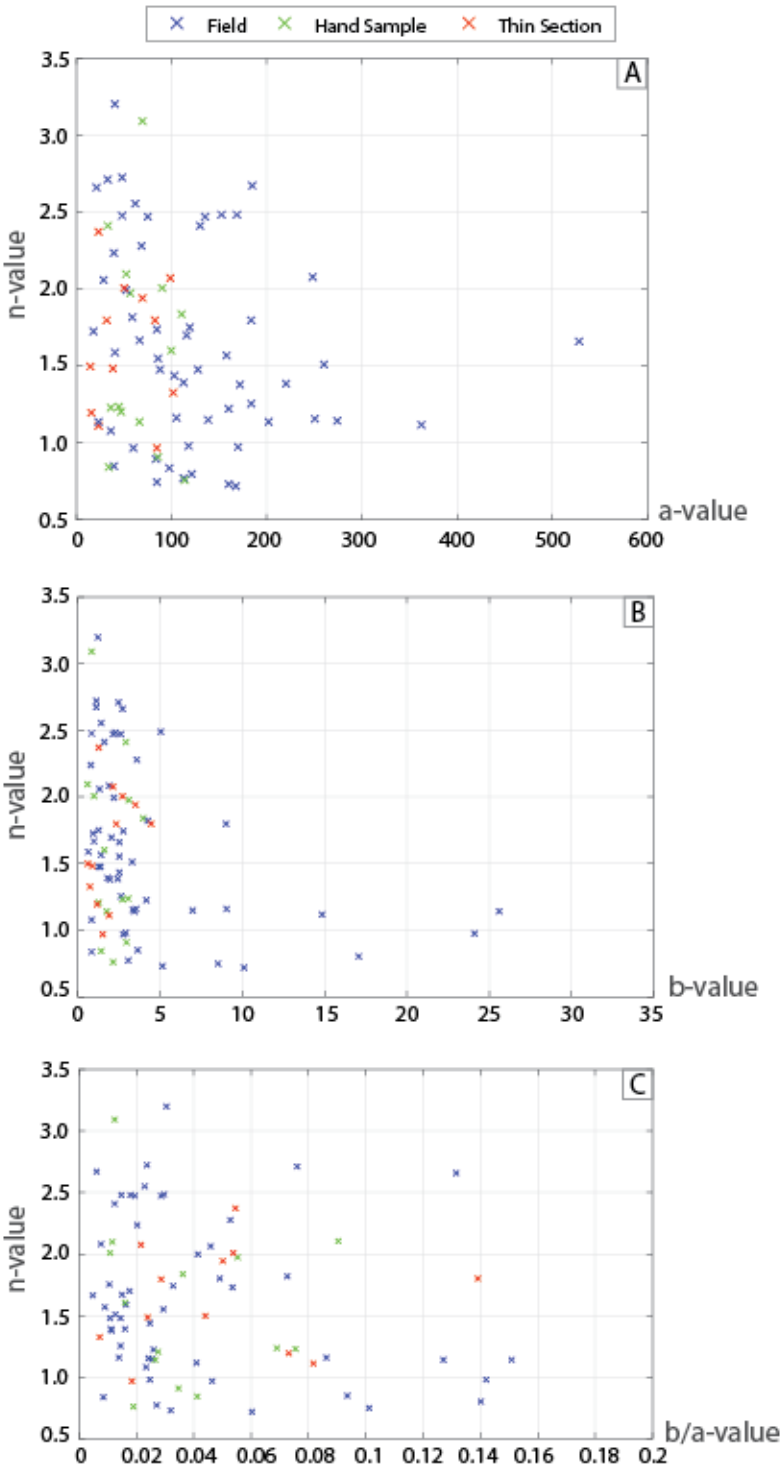

Figure 5.14: Lamé parameter n against a of all fractures; B) Lamé parameter n against b-values of all fractures; C) Lamé parameter n against b/a-values of all fractures. Blue = field data, green = hand sample data, and red = thin section data.

Higher temperatures appear to favor the formation of fractures with low n (Figure 5.15). The homogenization temperatures of inclusions in fractures with elliptical aperture profiles are between 150 and 260°C. Fractures with n-values lower than 1.5, the more linear fractures, contain higher homogenization temperatures of 270-315°C. The temperature range is also smaller than those with n-values greater than 2.

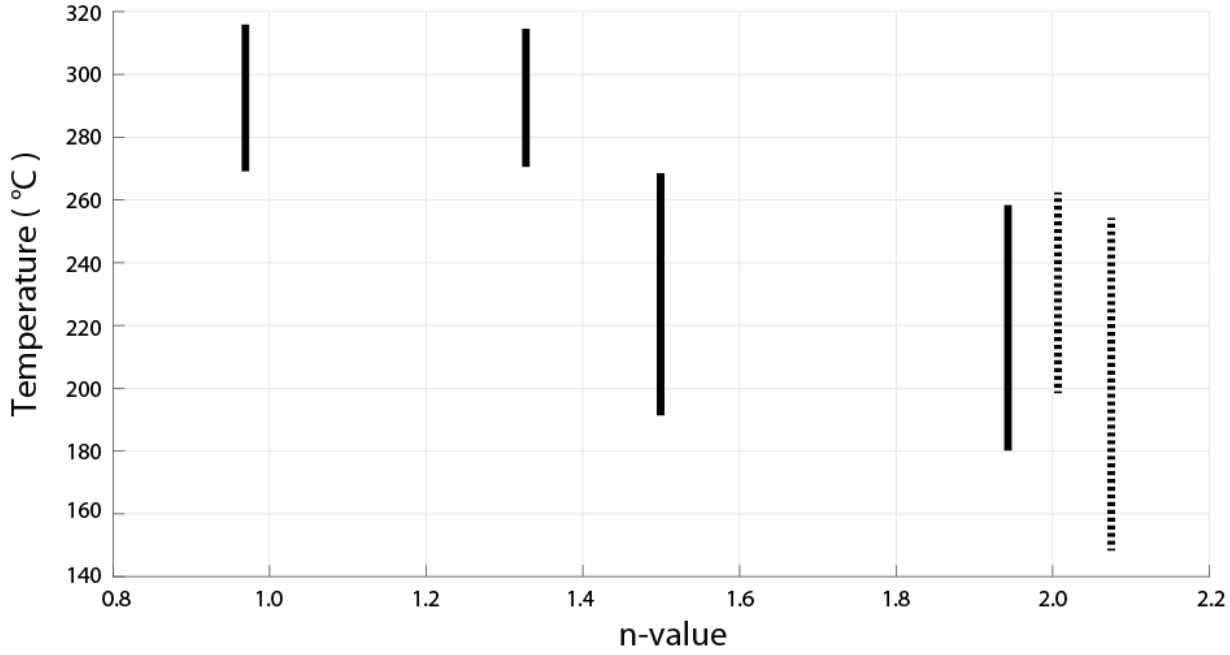

Figure 5.15: Lamé parameter n against fluid inclusion homogenization temperatures of all fractures listed in Table 5.1. Fractures with low n-values tend to form at higher temperatures. Solid lines = top fracture tips, dashed lines = samples from bottom tips

Proposed models of non-elliptical fracture growth

Fractures with elliptical aperture profiles, which have n-values close to 2, are consistent with linear elastic fracture mechanics. The aperture profile of a stationary fracture loaded by a uniform far-field stress in a homogeneous linear elastic medium is an elliptical function because displacement along the length or height of a fracture is a linear function of stress, and stress along the length or height of a fracture follows an elliptical function (Sneddon, 1946; Irwin, 1957; Pollard and Segall, 1987). For a propagating fracture in a linear elastic medium, the fracture shape at any stage of fracture growth is also elliptical (Figure 5.18A left and right). For a fracture propagating under critical stress loading conditions, with the stress concentration at the tip $K_I=K_{Ic}$ where K_{Ic} is the mode I fracture toughness of the material, the ratio of b/a is given by

$$b = \frac{4(1-\nu^2)K_{Ic}\sqrt{a}}{\pi E Y \sqrt{\pi}}$$ (Equation 4.1 in Alzayer et al. (2015),

where ν is Poisson's ratio, Y is a shape factor, E is Young's modulus, and a is half of fracture length. The aperture growth increment, i.e. the difference between two consecutive aperture profiles (Figure 5.18A right), is elliptical close to the fracture tip, reaches a local maximum at the position corresponding to the tip of the initial fracture aperture profile, and tapers off toward the center of the fracture.

The largest percentage the fractures in this study have n-values $n<2$ and close to 1. To account for fracture aperture profiles with $n<2$, I propose that fractures grow in increments of elastic aperture growth followed by periods of elastic stress dissipation by creep processes in the fracture tip region (Figure 5.18B). Each increment of fracture growth follows an elliptical function (Figure 5.18B middle). The final shape of the fracture depends on the ratio of the change in length or height a and the change in aperture b. A linear taper of the tip region results from fracture growth increments with $a_i>b_i$. Figure 5.16 shows the final fracture shape after 10

increments of fracture growth for different ratios of a_i and b_i, and for different Lamé n. For each growth increment, I assume that $a_i > b_i$, holding b_i constant (center column), decrease b_i over time (left column), or increase b_i over time (right column). In all model scenarios, and regardless of the n-values in each growth increment, I find that the final fracture shapes have n-values close to 1 (0.98 to 1.31).

n-value of each increment	Decreasing aperture growth The aperture growth (b_i) and the length growth (a_i) in each increment are described by $b_i = b_o - 0.005i$ $a_i = a_o + 0.5i$ Where i is the increment number, and $b_0 = 0.15$, and $a_0 = 2$	Constant aperture growth The aperture growth (b_i) and the length growth (a_i) in each increment are described by $b_i = 0.15$ $a_i = a_o + 0.5i$ Where i is the increment number, and $b_0 = 0.15$, and $a_0 = 2$	Increasing aperture growth The aperture growth (b_i) and the length growth (a_i) in each increment are described by $b_i = b_o + 0.005i$ $a_i = a_o + 0.5i$ Where i is the increment number, and $b_0 = 0.15$, and $a_0 = 2$
2	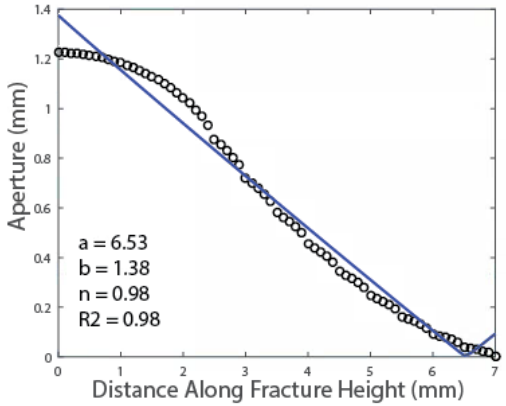	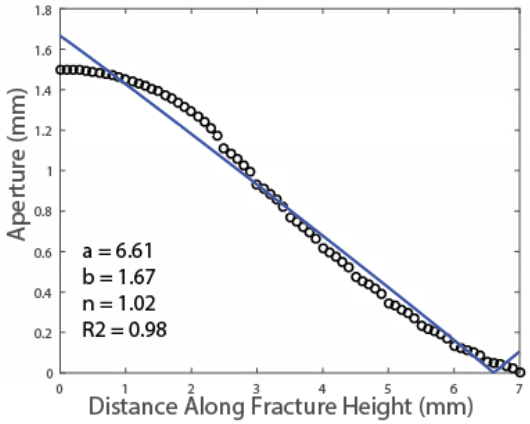	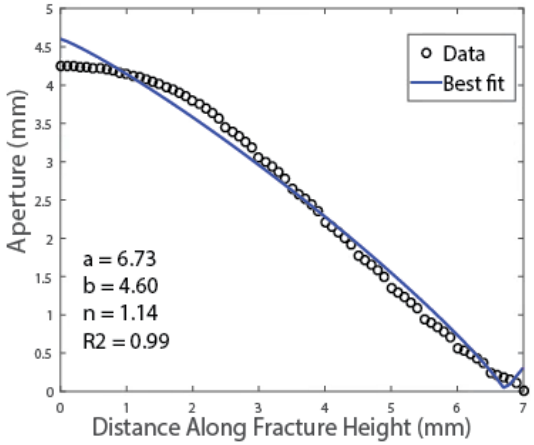
3	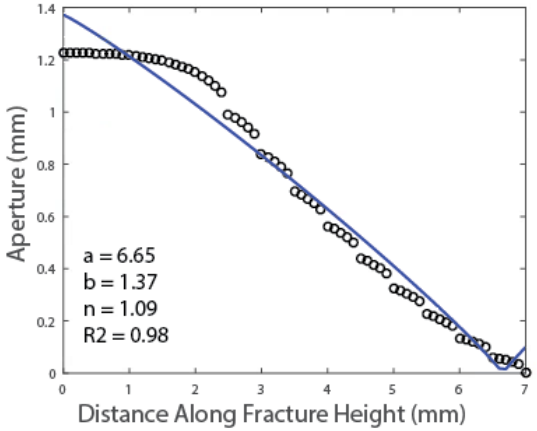	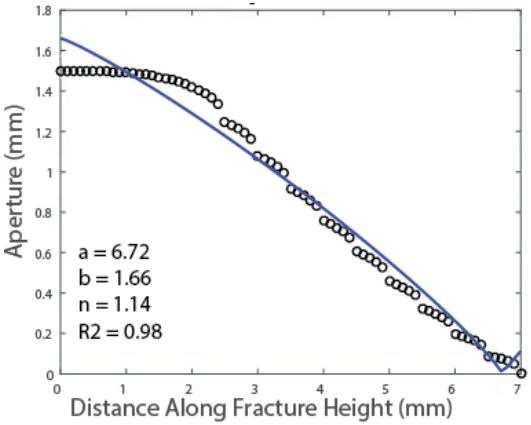	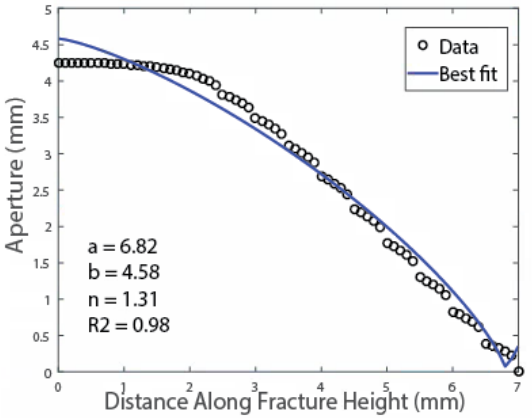

Figure 5.16: Continued on next page

Figure 5.16: Fracture growth through elastic fracture growth increments with $a_i > b_i$ and stress dissipation around the fractures tips. Each increment of fracture growth follows an elliptical function, with a (fracture half-length or –height) and b (fracture half-aperture) change at indicated in column header (units in mm). Circles: calculated aperture profile for 10 growth increments; solid line: best-fit Lamé function.

Fractures with Lamé n>2 are obtained with fracture growth increments with n-values greater than 2, and aperture growth increments $b_i > a_i$, i.e. the fracture growing faster in aperture than in length (Figure 5.17 and Figure 5.18C). Lamé n values for the final fracture shape obtained in these simulations range 2.30 – 2.34, using n=3 for each growth increment (bottom row of Figure 5.17). The n value of the final fracture shape equals the n of the increment for stationary fractures with $a_i=0$.

Fracture growth with variable a_i and b_i values has been inferred by Alzayer et al. (2016) for quartz cemented fractures from the Travis Peak sandstone based on kinematic reconstructions of crack-seal fracture opening increments. They proposed a two-stage fracture growth history, with an early stage of rapid length and slow aperture growth, followed by a stage of slow length and rapid aperture growth. They attributed this change in fracture opening kinematics to changes in deformation mechanism with increasing burial depth and temperature, resulting in enhanced rates of solution-precipitation creep allowing aperture growth with little concurrent fracture length growth.

Slower growth in fracture aperture in comparison to the growth in fracture length can result from an increase in temperature and a corresponding decrease in K_{IC}. Atkinson (1984) showed that K_{IC} of synthetic quartz decreased by 0.5 MPa$\sqrt{m}$ with a decrease in temperature from 200°C to 300°C. Following equation (1) the reduced K_{IC} leads to a decrease in maximum aperture for a critically propagating fracture. Although the Poisson ratio ν decreases with increasing temperature, the change in (1- v^2) is smaller compared to the change in K_{IC}. Young's modulus E also decreases at higher temperature, but the change is also smaller in comparison to the change in K_{IC}. For instance, Tian et al. (2016) and Ding et al. (2016) showed that the E of

sandstone dropped by approximately 20% or less as the temperatures changed from 200°C to 400°C.

I also observed that fractures with low n-values are wider (have greater b-values) and correlate with higher fluid inclusion homogenization temperatures than those of elliptical aperture profiles. The large aperture profiles might be a result of enhanced diffusive mass transfer at higher temperatures. Diffusive mass transfer, which includes diffusion along fluid-filled grain boundaries of host rock, migration, and precipitation of the material, is an important deformation mechanism in low-grade metamorphic rock (Knipe, 1989; Lloyd and Knipe, 1992; Twiss and Moores, 2007). With increasing temperature, faster rates of diffusive mass transfer in the host rock and chemical weakening at fracture tips can result in larger apertures and faster growth (Shimizu, 1995). The fracture cement, likely derived by dissolution from hostrock grains and diffusive mass transfer into the fracture space, provides evidence for the coupling between fracture growth and host rock chemical reactions (Ramsay and Huber 1987; Lloyd and Knipe, 1992; Eichhubl and Boles, 1998). The cement that filled the studied fractures, both with high n-values and low n-values, are generally minerals that make up the host rock. However, fractures with low n-values tend to be more completely filled with quartz cement and contain more chlorite, magnetite and rutile cement. This can be indicative of more effective diffusive mass transfer processes between fracture and host rock.

Fractures with n-values of 1.25 have blocky cement (Figure 5.12). Of fractures with blocky cement, 52% have $n<1.25$ whereas fracture with crack-seal cement texture have $n>1.5$ suggesting that crack-seal cement favors fracture growth conditions that lead to high n values. Following Lander and Laubach (2014), crack-seal cement forms synkinematically or concurrently with fracture opening when the rate of fracture cement growth keeps pace with the

rate of fracture opening. If the rate of fracture opening exceeds the rate of cement growth, euhedral cement growth will line the fracture instead. Later postkinematic cement will eventually occlude remaining fracture pore space forming blocky cement textures. The preferred cementation of fractures of low n by blocky cement may thus be interpreted as a result of rapid fracture aperture growth at higher temperature.

Fractures with n>2 require a process of tip blunting. Tip blunting can result from the presence of another closely spaced collinear fracture tip (Delaney and Pollard, 1981). The small separation between them causes a slightly greater dilation of adjacent tips, resulting in relative blunting of tips compared to isolated fracture tips in the same material. Although 33% of fracture tips that are located in close proximity to other fracture tips have n-values between 2.25 and 2.75, they are generally not arranged in a collinear pattern with neighboring fractures. Instead, I propose that blunting it the result of enhanced solution-precipitation creep in the tip region of fractures, resulting from a coupling between stress concentration in the tip region and chemical reaction rates.

n-value of each increment growth

Decreasing aperture growth

The aperture growth (b_i) and the length growth (a_i) in each increment are described by

$$b_i = b_o - 0.01i$$
$$a_i = a_o + 0.005i$$

Where i is the increment number, and b_0 = 0.15, and a_0 = 2

Constant aperture growth

The aperture growth (b_i) and the length growth (a_i) in each increment are described by

$$b_i = 0.15$$
$$a_i = a_o + 0.005i$$

Where i is the increment number, and b_0 = 0.15, and a_0 = 2

Increasing aperture growth

The aperture growth (b_i) and the length growth (a_i) in each increment are described by

$$b_i = b_o + 0.01i$$
$$a_i = a_o + 0.005i$$

Where i is the increment number, and b_0 = 0.15, and a_0 = 2

2

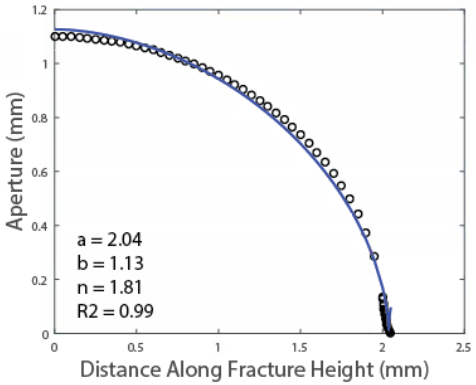

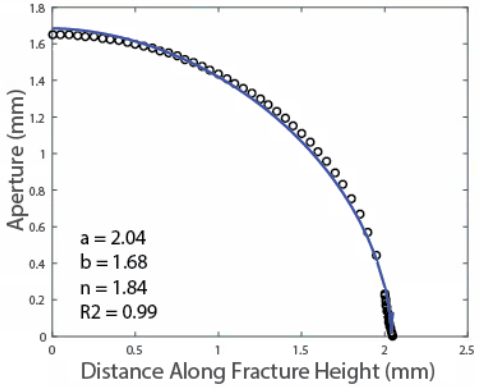

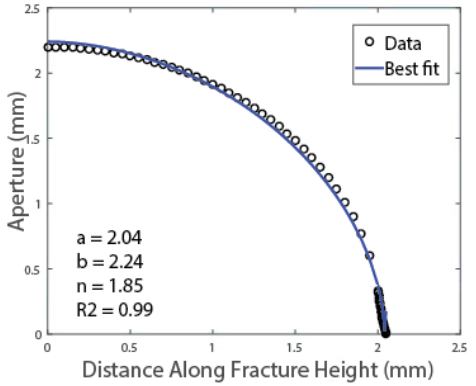

3

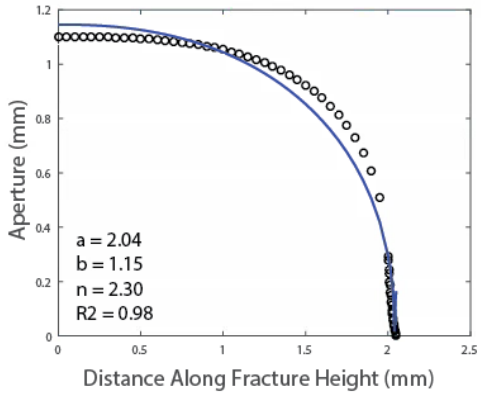

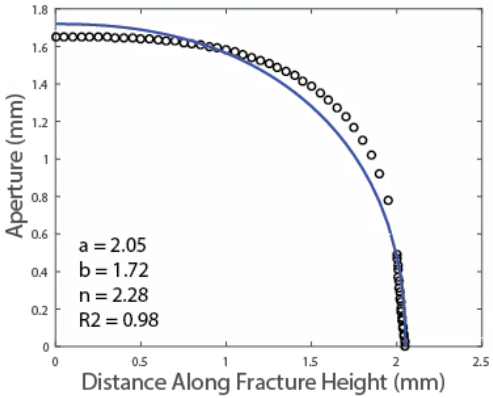

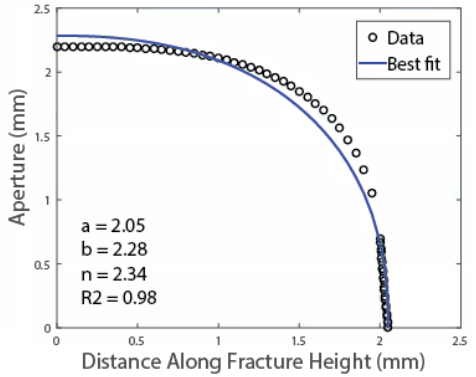

Figure 5.17: Continued on next page

Figure 5.17: Fracture growth through elastic fracture growth increments with $a_i<b_i$ and stress dissipation around the fractures tips. Each increment of fracture growth follows an elliptical function, with a (fracture half-length or –height) and b (fracture half-aperture) change at indicated in column header (units in mm). Circles: calculated aperture profile for 10 growth increments; solid line: best-fit Lamé function.

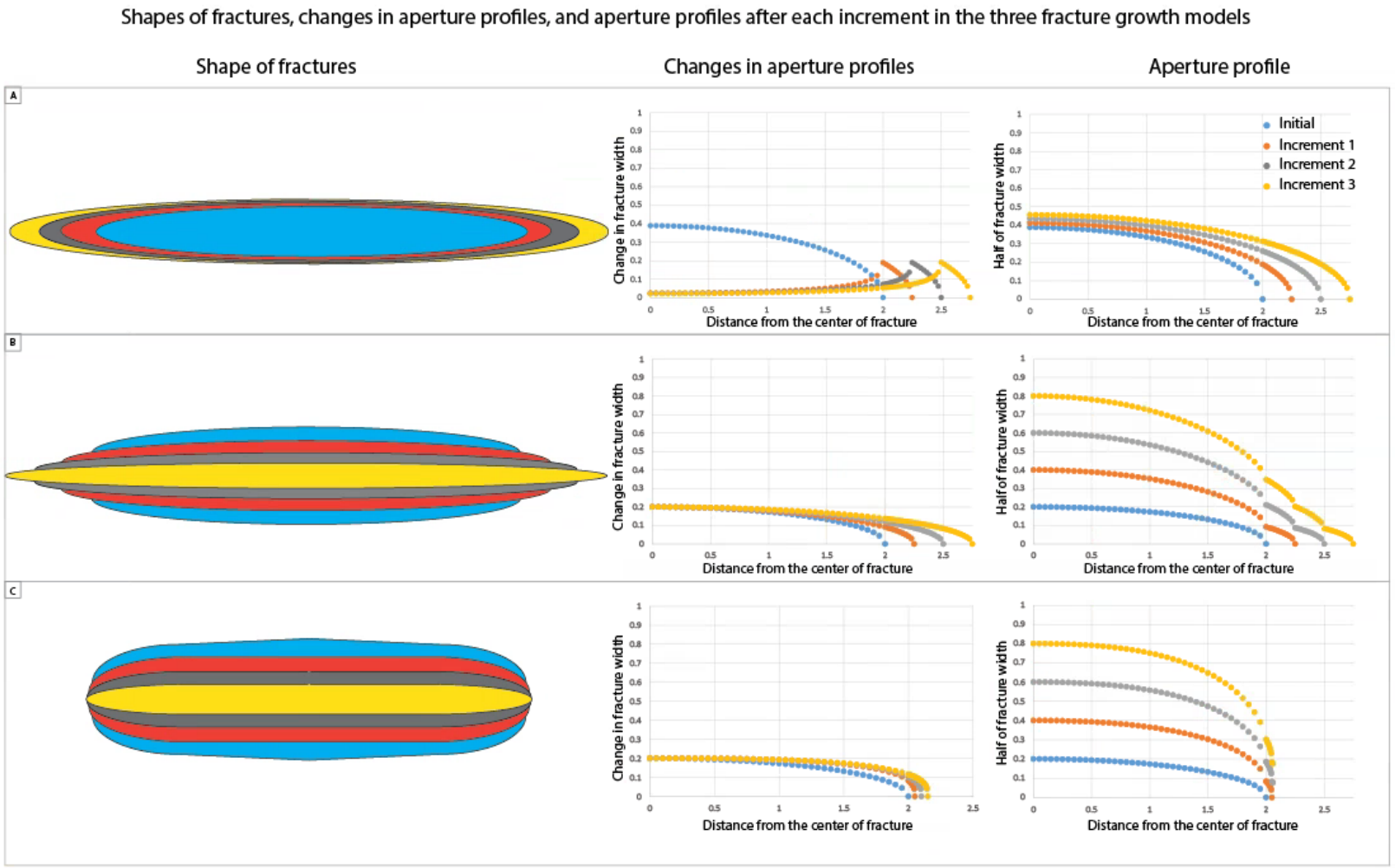

Figure 5.18: Continued on next page

Figure 5.18: Shapes of fracture, change in aperture profiles, and aperture profiles after each increment in A) linear elastic fracture, B) fracture growth after stress dissipation with fast growth in length, and C) fracture growth after stress dissipation with slow growth in height and fast growth in aperture. Blue represents the initial fracture. Red, gray, and yellow represent opening increments 1, 2, and 3, respectively. Apertures in center and right columns are twice the apertures in the left column.

CONCLUSIONS

The aperture profiles of the opening mode fractures in the Campito Formation that I collected from the field, hand sample, and thin sections display various degrees of ellipticity as expressed by the Lamé parameter n. The n-values of half of the aperture profiles range from less than 1 to more than 2, representing fracture aperture profiles ranging from triangular to elliptical and approaching rectangular shapes. This wide range in n-values indicates that fracture aperture profiles are likely controlled by the combination of competing mechanisms.

Fractures with elliptical aperture profiles, which have n-values close to 2, generally contain fibrous crack-seal cement. Elliptical aperture profiles are consistent with linear elastic fracture mechanics. The crack-seal texture indicates that they might have formed in alternating increments between brittle fracture opening and cementation. The homogenization temperature of the fractures with elliptical aperture profiles ranges between 150°C and 250°C.

I explain fracture aperture profiles with $n<2$ through a process of incremental elastic fracture growth alternating with stages of stress dissipation by solution-precipitation creep in the tip regions of fractures. This mechanisms leads to aperture profiles for $n \sim 1$ if fracture length of height increments a_i are larger than aperture increments b_i. Fracture with apertures profiles with $n>2$ require the combination of opening increments with $n>2$ and a slow rate of length or height growth relative to the rate of aperture growth.

I attribute observed variations in n to competing effects of increasing temperature on fracture growth rate by lowering fracture toughness and increasing rates of solution-precipitation creep with increasing temperature. Observed higher fluid inclusion homogenization temperatures for fractures with low n suggest that faster rates of propagation are favored at higher temperature resulting in lower n values. Lamé n-values larger than 2 may result from tip blunting by enhanced solution-precipitation creep in the vicinity of fracture tips. These results suggest that aperture profiles reflect fracture growth conditions and mechanisms. The information on the aperture profile shapes in different conditions can be used as input parameters for numerical fracture growth simulations in various environments and conditions such as igneous and epithermal or geothermal systems, fractured groundwater aquifers, and oil and gas systems.

APPENDICES

Appendix A: Curve Fitting Results

The following are results of nonlinear least squares curve fitting in Matlab. The basic equation for the solver was the superellipse or Lamé curve equation (see the methods section for more details on curve fitting).

CURVE FITTING RESULT: TOP TIPS OF FRACTURES FROM OUTCROPS

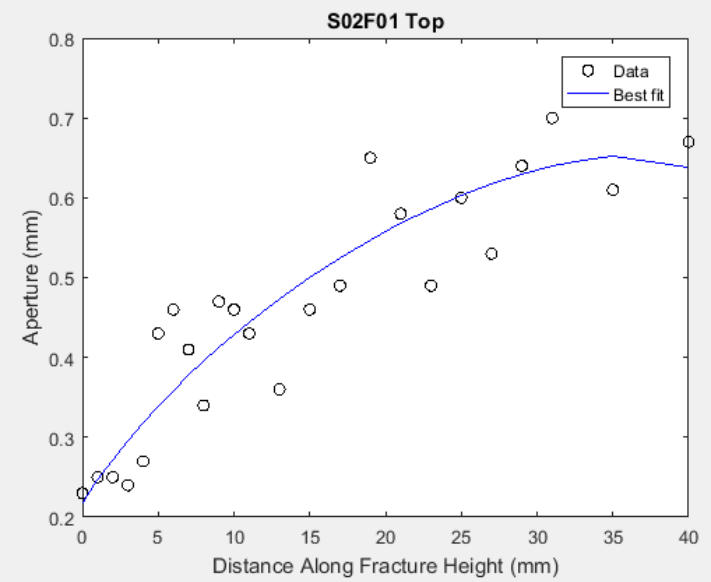


```
Name =

S02F01


Type =

Top


ans =

          results
    a          40
    b     0.65209
    c      35.423
    n      1.5889
    R2     0.84042
```

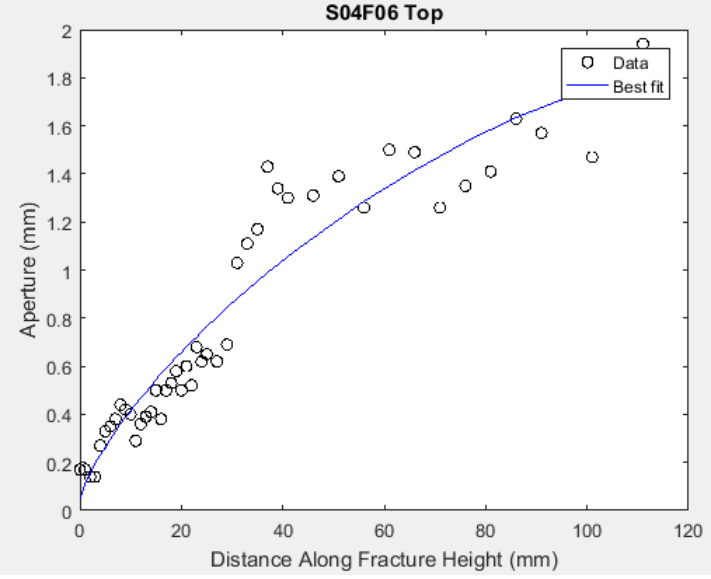


```
Name =

S04F06


Type =

Top


ans =

          results
    a      112.37
    b      1.8021
    c      111.74
    n      1.3926
    R2     0.91933
```

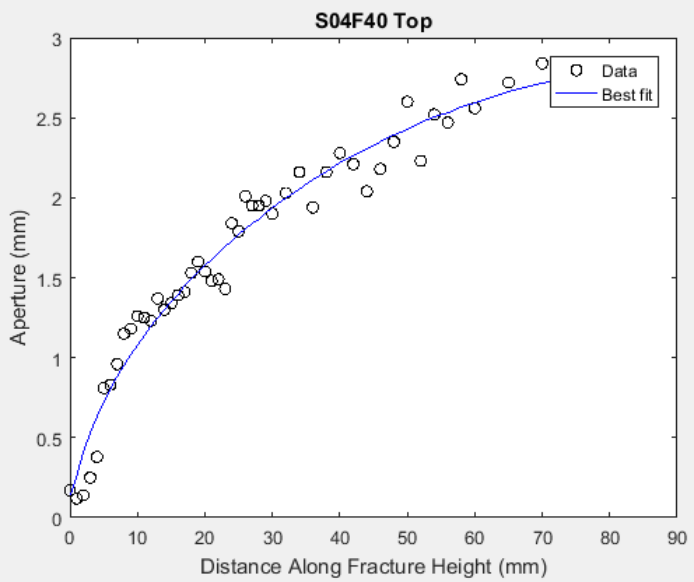


```
Name =

S04F40


Type =

Top


ans =

          results
    a      85.029
    b      2.7956
    c      85.316
    n      1.7415
    R2     0.96826
```

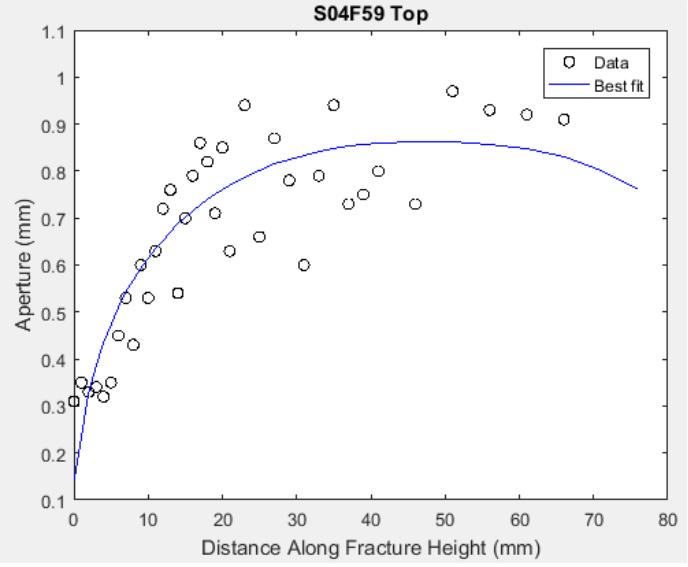


```
Name =

S04F59


Type =

Top


ans =

          results
    a      47.741
    b      0.86176
    c      47.977
    n      2.4764
    R2     0.71067
```

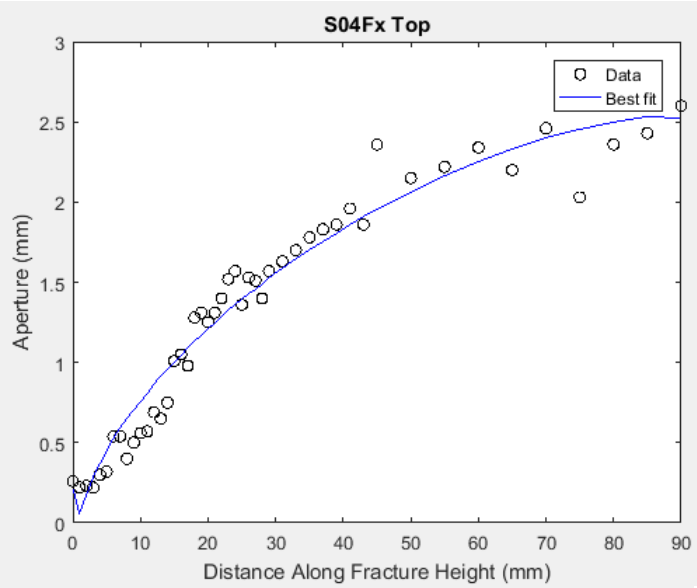


```
Name =

S04Fx


Type =

Top


ans =

          results
    a       86.09
    b      2.5351
    c      87.243
    n      1.5501
    R2    0.95719
```

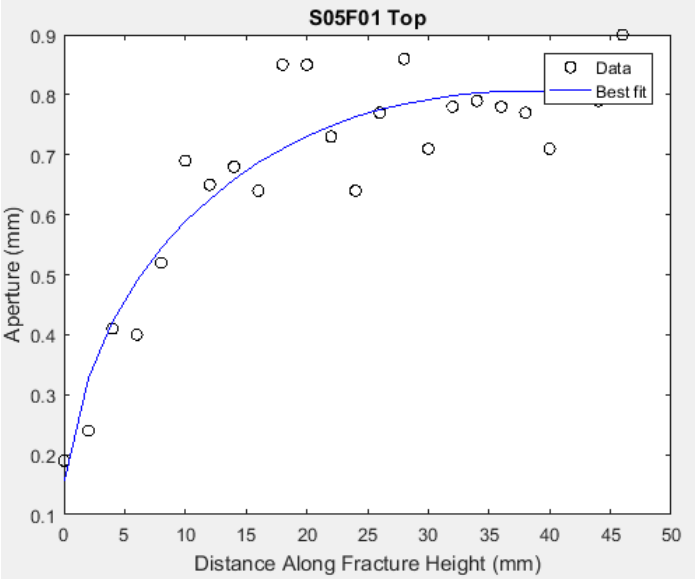


```
Name =

S05F01


Type =

Top


ans =

          results
    a      39.661
    b     0.80627
    c      39.208
    n      2.2369
    R2    0.86482
```

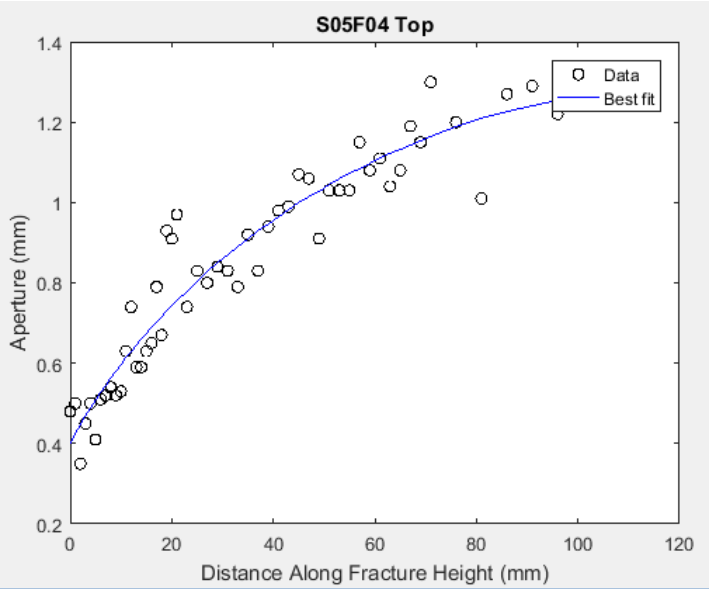


```
Name =

S05F04


Type =

Top


ans =

           results
    a       119.41
    b       1.2704
    c          110
    n       1.7506
    R2     0.91746
```

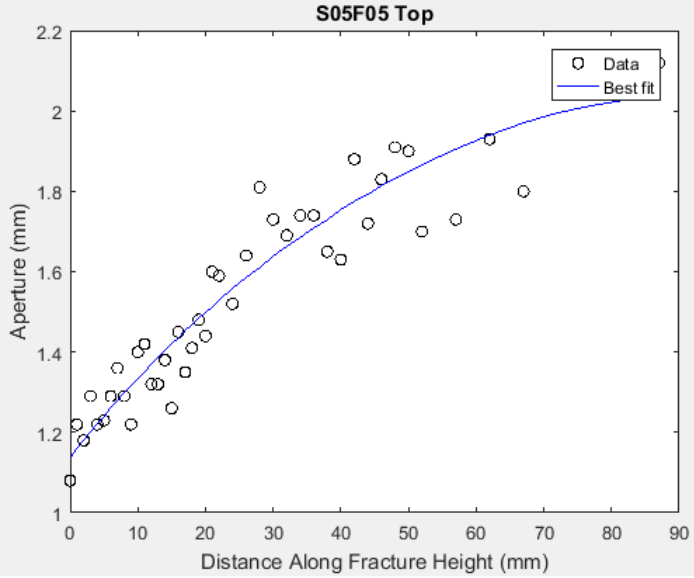


```
Name =

S05F05


Type =

Top


ans =

           results
    a          116
    b       2.0368
    c       88.176
    n       1.6972
    R2     0.90849
```

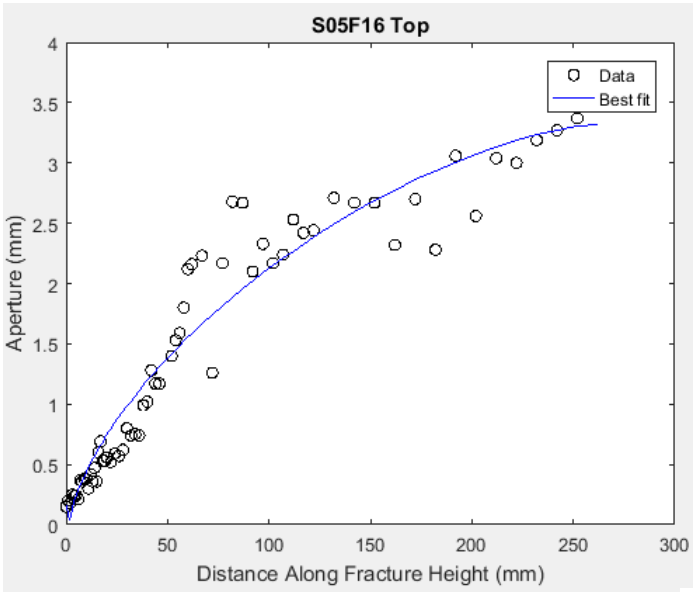


```
Name =

S05F16


Type =

Top


ans =

          results
    a      260.37
    b      3.3177
    c       262.1
    n      1.5091
    R2    0.93221
```

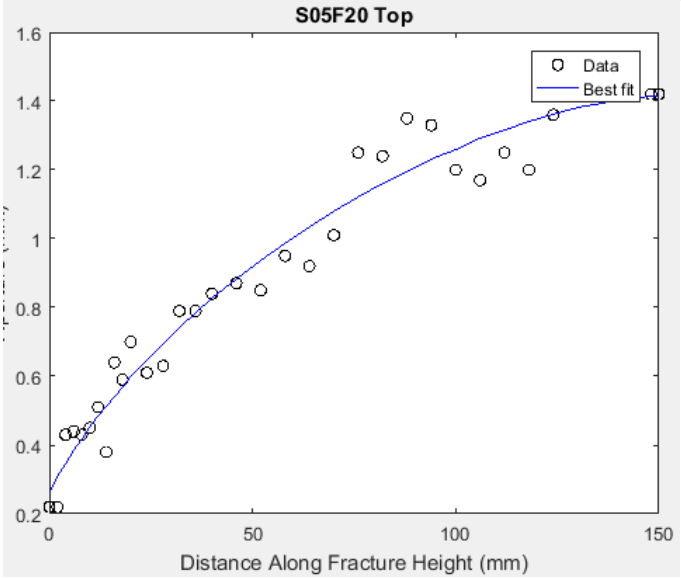


```
Name =

S05F20


Type =

Top


ans =

          results
    a      157.32
    b       1.416
    c         150
    n      1.5666
    R2     0.9616
```

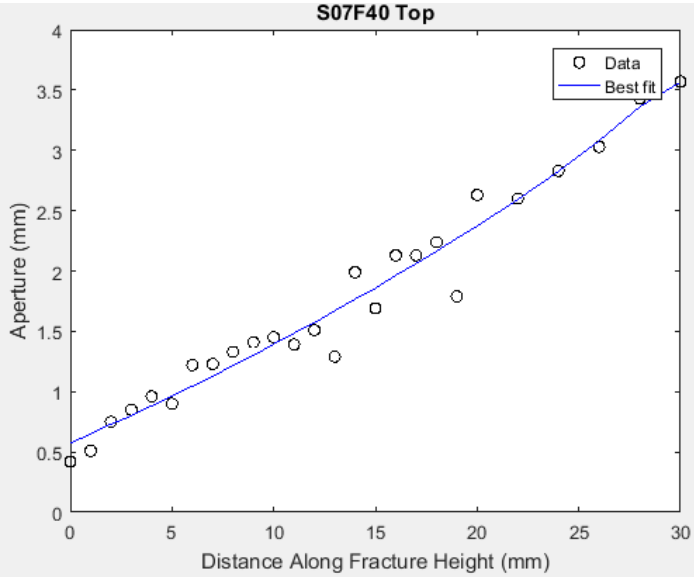


```
Name =

S07F40


Type =

Top


ans =

          results
    a       38.99
    b      3.6514
    c      29.621
    n     0.84774
    R2    0.96276
```

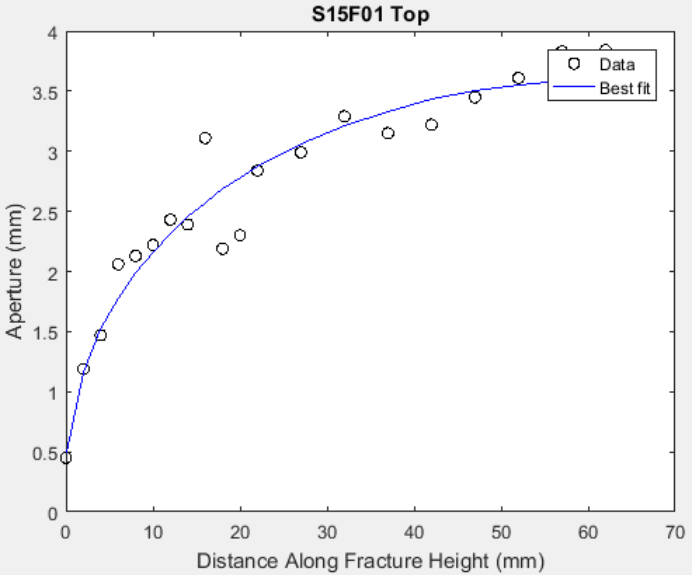


```
Name =

S15F01


Type =

Top


ans =

          results
    a       68.33
    b      3.6096
    c          68
    n      2.2794
    R2    0.92803
```

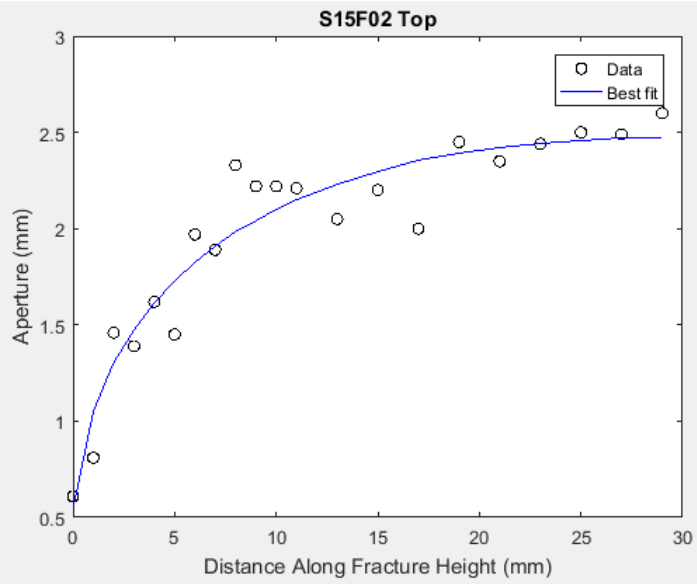


```
Name =

S15F02


Type =

Top


ans =

          results
    a      32.566
    b       2.476
    c      32.349
    n       2.711
    R2    0.90855
```

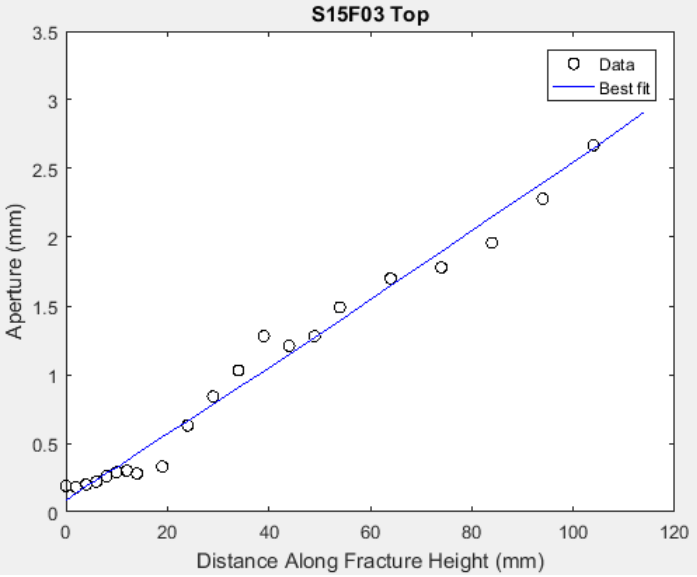


```
Name =

S15F03


Type =

Top


ans =

          results
    a      117.96
    b      2.9146
    c         114
    n       0.982
    R2     0.9841
```

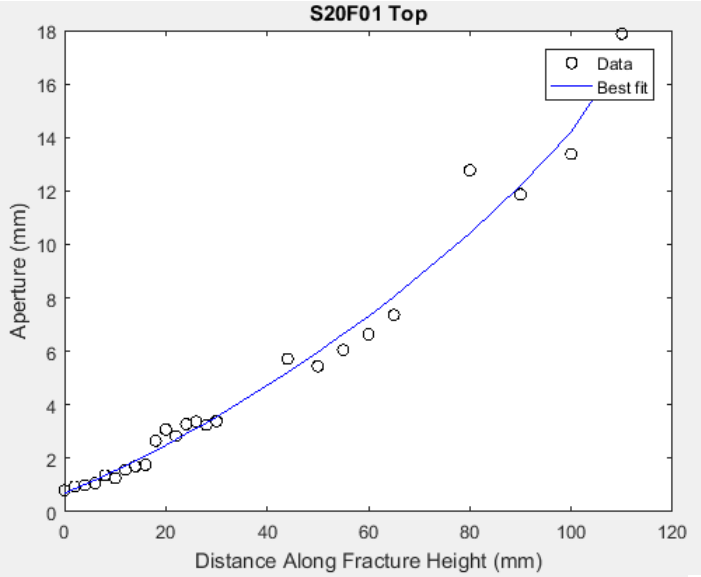


```
Name =

S20F01


Type =

Top


ans =

           results
    a       121.62
    b       17.052
    c          110
    n      0.80061
    R2     0.98029
```

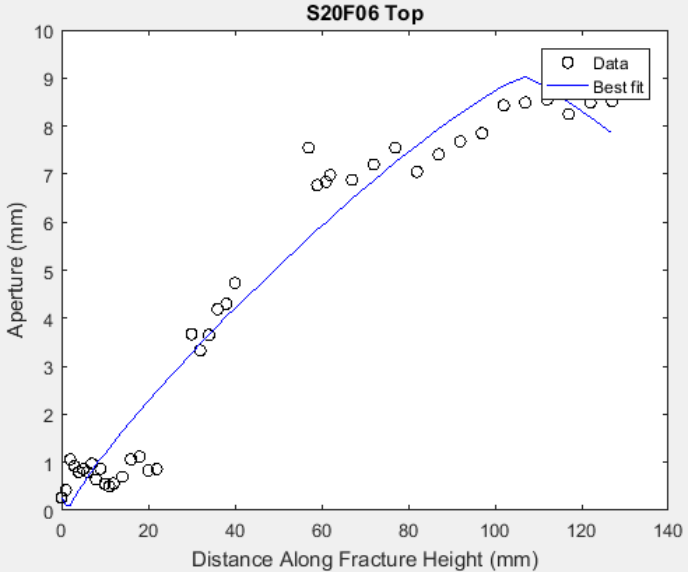


```
Name =

S20F06


Type =

Top


ans =

           results
    a       104.89
    b       9.0396
    c       106.35
    n       1.1602
    R2     0.95289
```

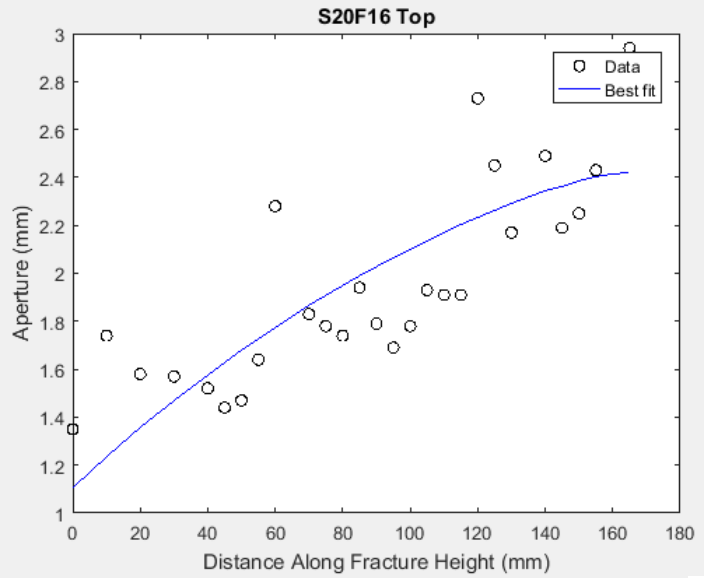


```
Name =

S20F16


Type =

Top


ans =

           results
    a          220
    b       2.4194
    c       163.38
    n       1.3884
    R2     0.59078
```

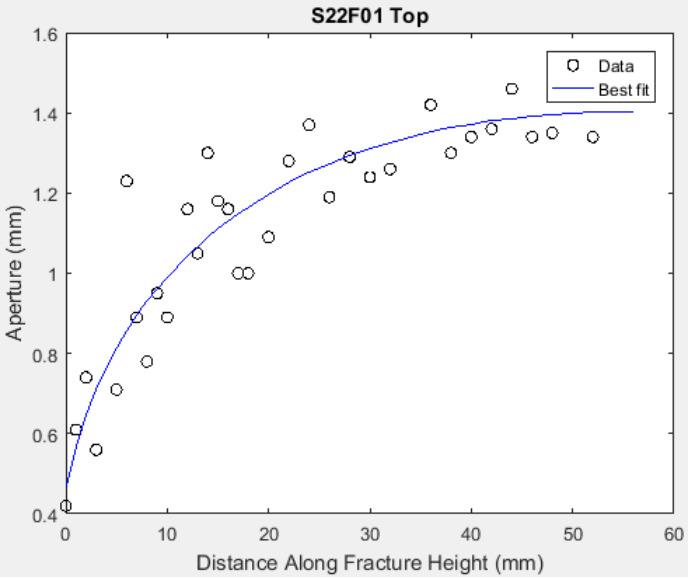


```
Name =

S22F01


Type =

Top


ans =

           results
    a       61.485
    b       1.4039
    c           60
    n       2.5535
    R2      0.8463
```

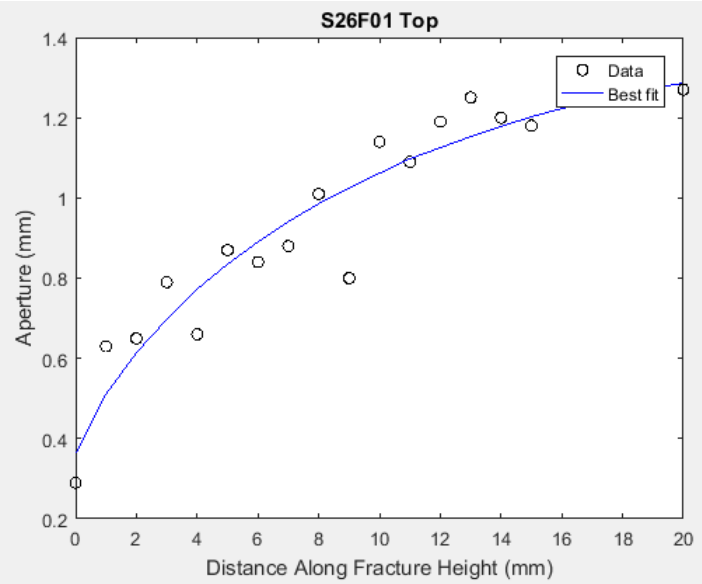


```
Name =

S26F01


Type =

Top


ans =

          results
    a      29.008
    b      1.3327
    c          28
    n      2.0619
    R2    0.91557
```

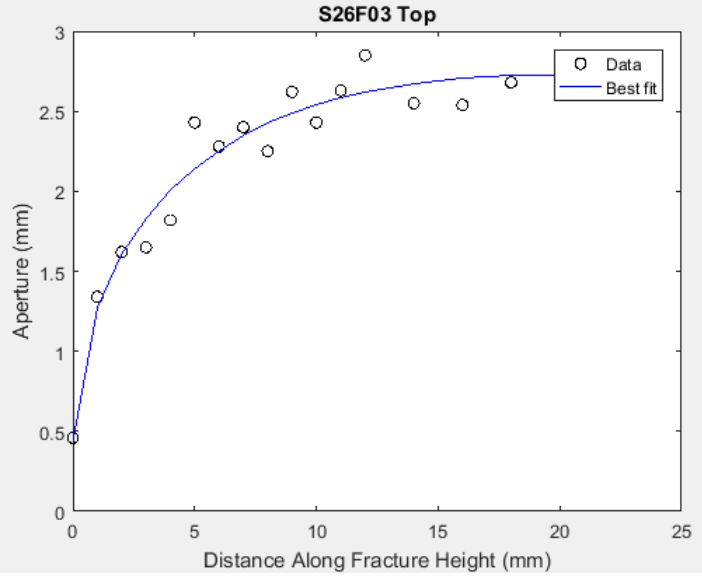


```
Name =

S26F03


Type =

Top


ans =

          results
    a      20.736
    b      2.7267
    c      20.666
    n      2.6594
    R2    0.95275
```

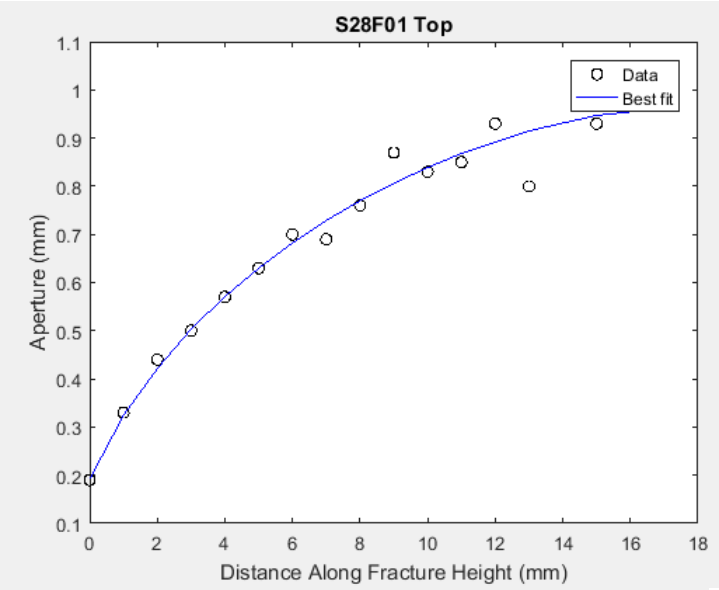


```
Name =

S28F01


Type =

Top


ans =

          results
    a          18
    b     0.96306
    c      17.338
    n      1.7282
    R2     0.96691
```

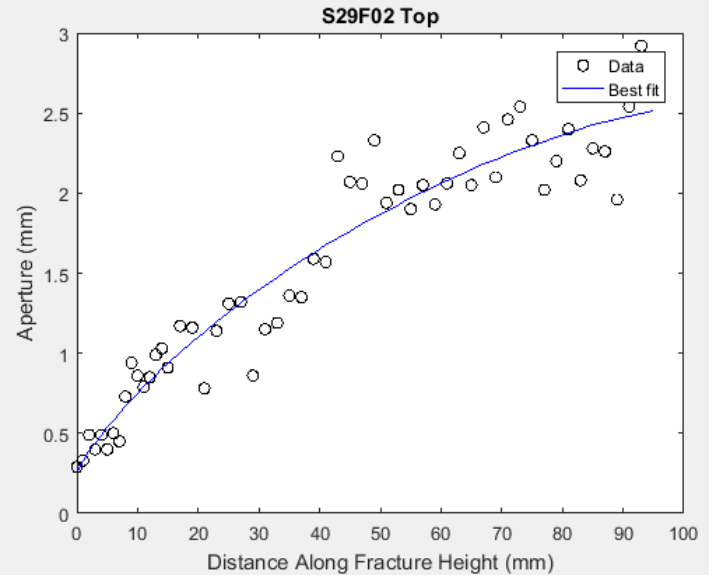


```
Name =

S29F02


Type =

Top


ans =

          results
    a      102.73
    b      2.5345
    c       99.88
    n      1.4358
    R2     0.91632
```

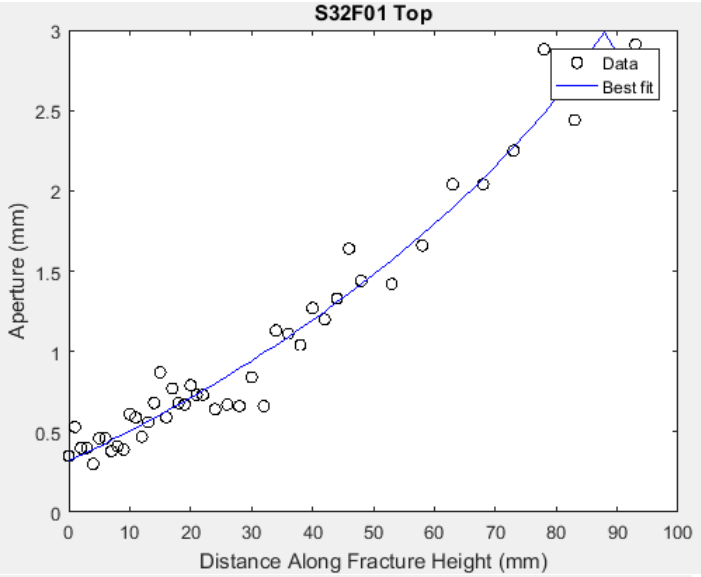


```
Name =

S32F01


Type =

Top


ans =

           results
    a       112.53
    b       3.0591
    c       87.397
    n      0.76914
    R2     0.96068
```

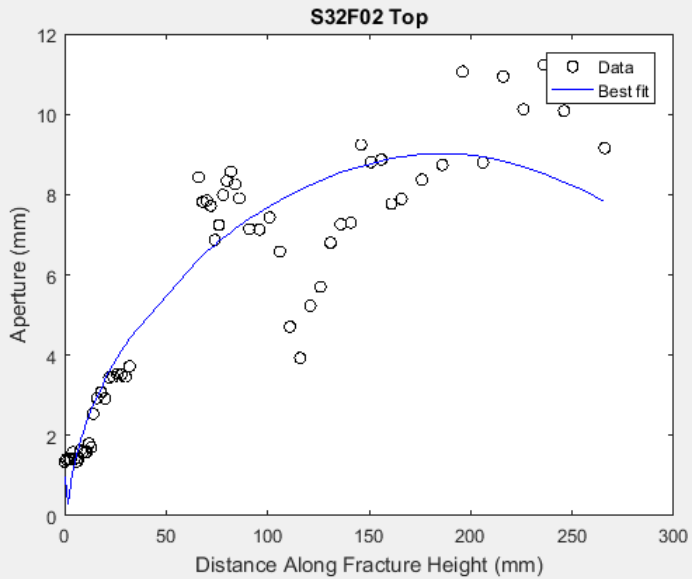


```
Name =

S32F02


Type =

Top


ans =

           results
    a       183.6
    b      9.0252
    c      185.37
    n      1.7982
    R2     0.81986
```

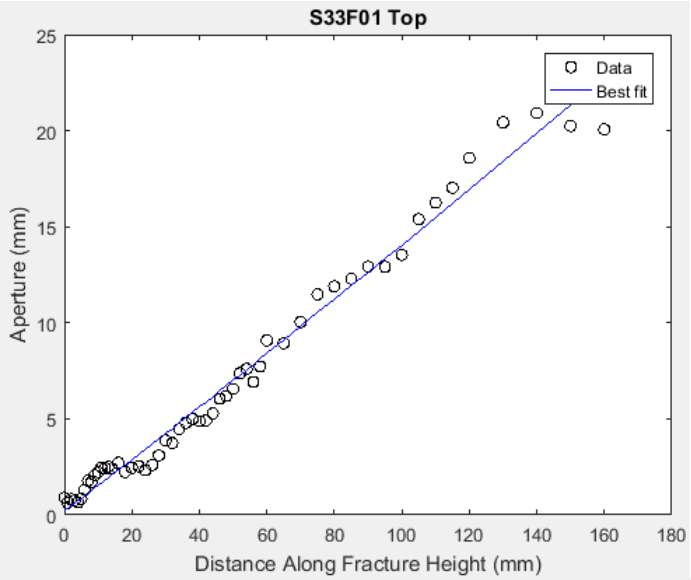


```
Name =

S33F01


Type =

Top


ans =

           results
    a       169.71
    b       24.097
    c       167.91
    n       0.9765
    R2     0.98479
```

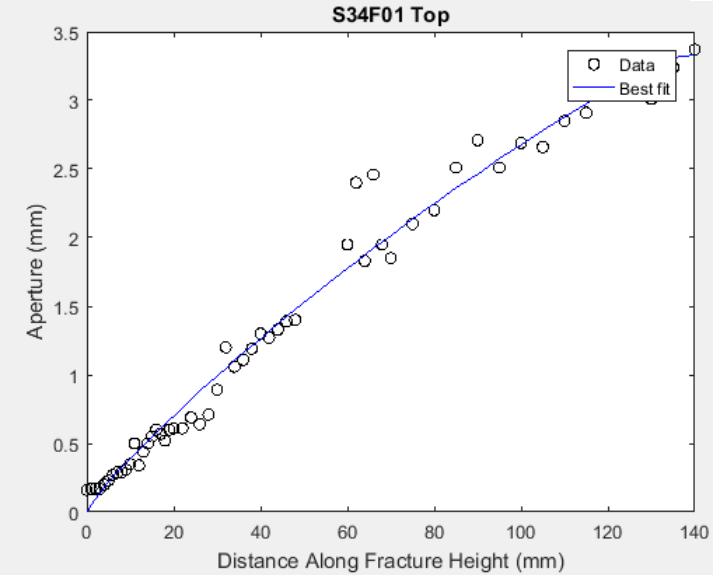


```
Name =

S34F01


Type =

Top


ans =

           results
    a       138.05
    b       3.3495
    c       137.96
    n       1.1507
    R2     0.97978
```

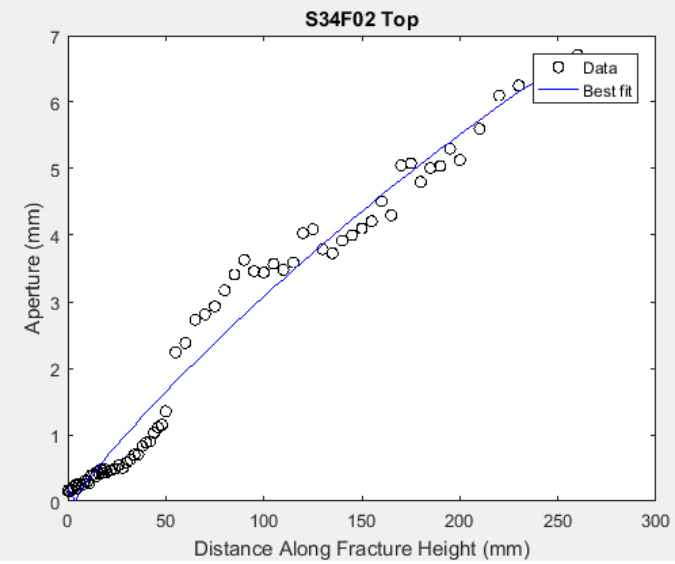


```
Name =

S34F02


Type =

Top


ans =

           results
    a       274.31
    b       6.9839
    c       278.14
    n       1.1469
    R2     0.97505
```

CURVE FITTING RESULT: BOTTOM TIPS OF FRACTURES FROM OUTCROPS

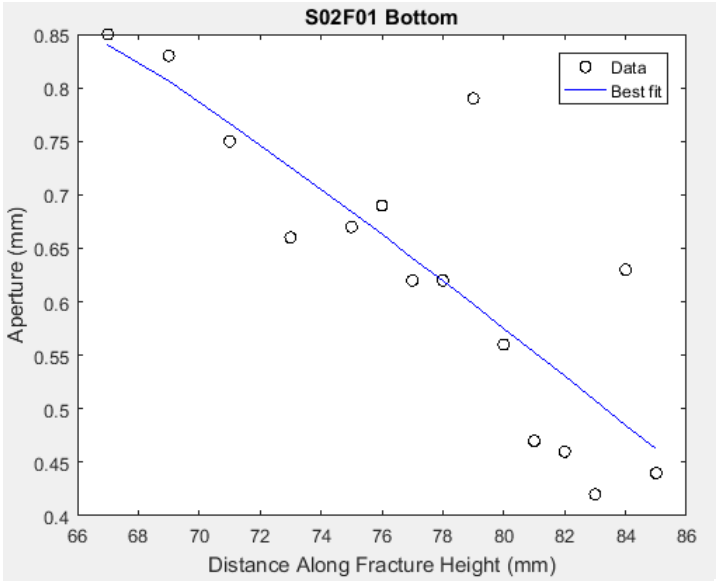


```
Name =

S02F01


Type =

Bottom


ans =

          results
    a          36
    b     0.84217
    c      66.898
    n      1.0774
    R2     0.6898
```

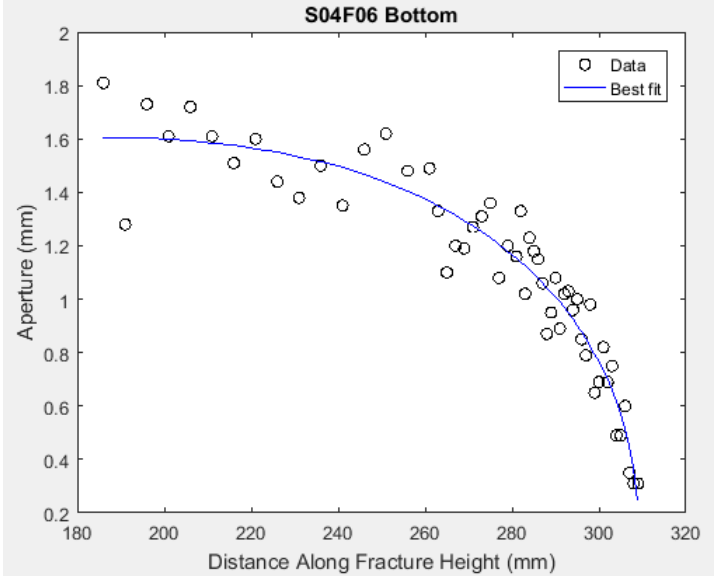


```
Name =

S04F06


Type =

Bottom


ans =

          results
    a      130.16
    b      1.6068
    c      179.42
    n      2.4088
    R2     0.9101
```

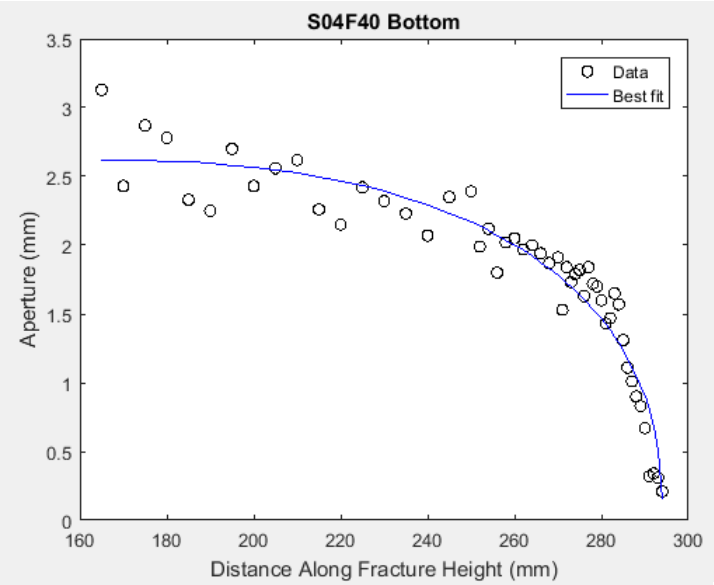


```
Name =

S04F40


Type =

Bottom


ans =

          results
    a      134.89
    b      2.6211
    c      159.06
    n      2.4714
    R2     0.91398
```

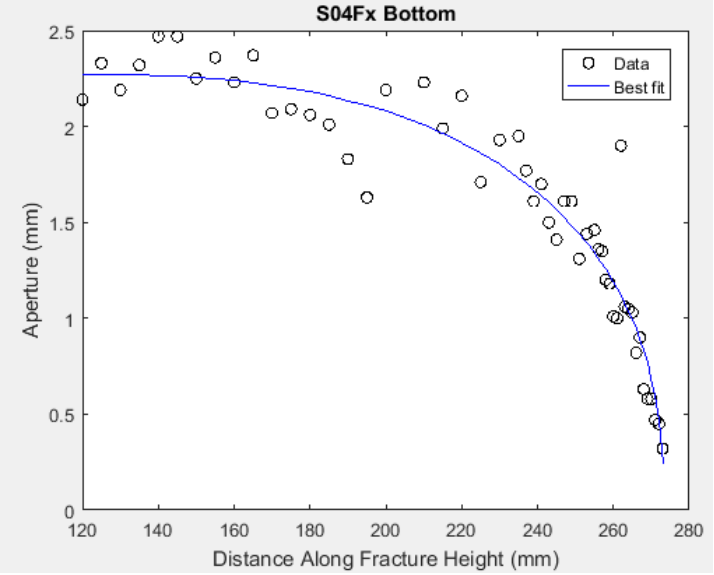


```
Name =

S04Fx


Type =

Bottom


ans =

          results
    a      152.4
    b      2.2699
    c      120.83
    n      2.4819
    R2     0.90932
```

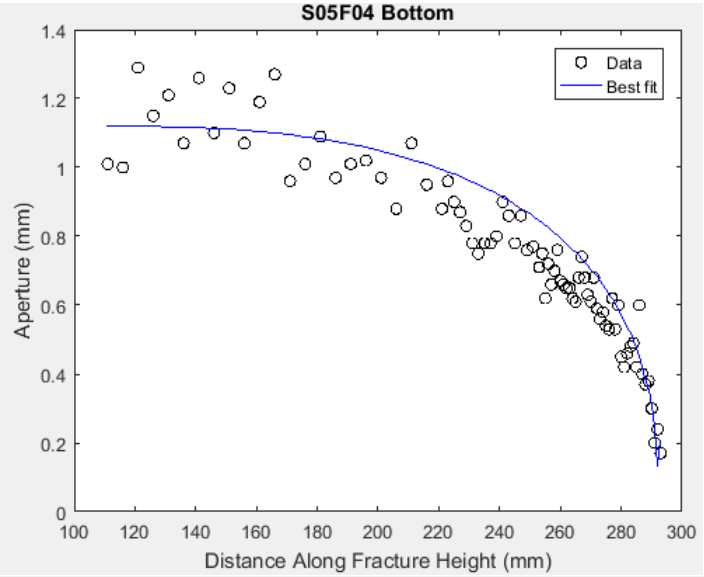


```
Name =

S05F04


Type =

Bottom


ans =

          results
    a       185.1
    b      1.1199
    c      107.14
    n      2.6724
    R2    0.84614
```

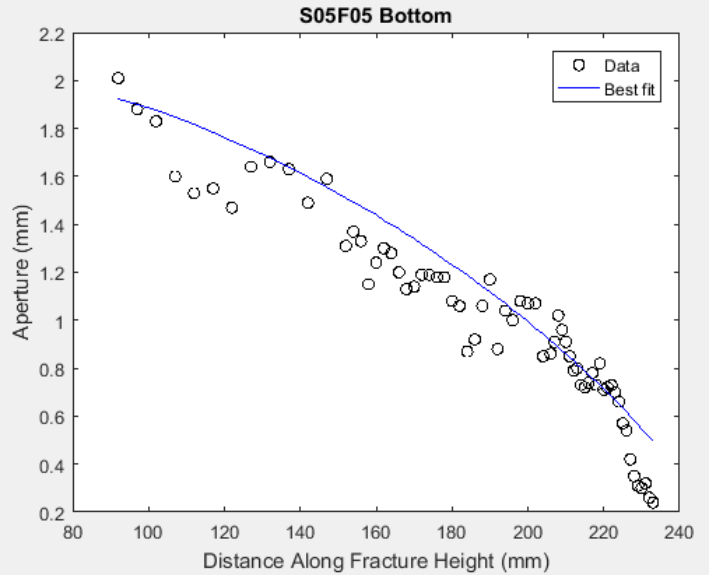


```
Name =

S05F05


Type =

Bottom


ans =

          results
    a       172.26
    b      1.9579
    c      79.914
    n      1.3803
    R2    0.86779
```

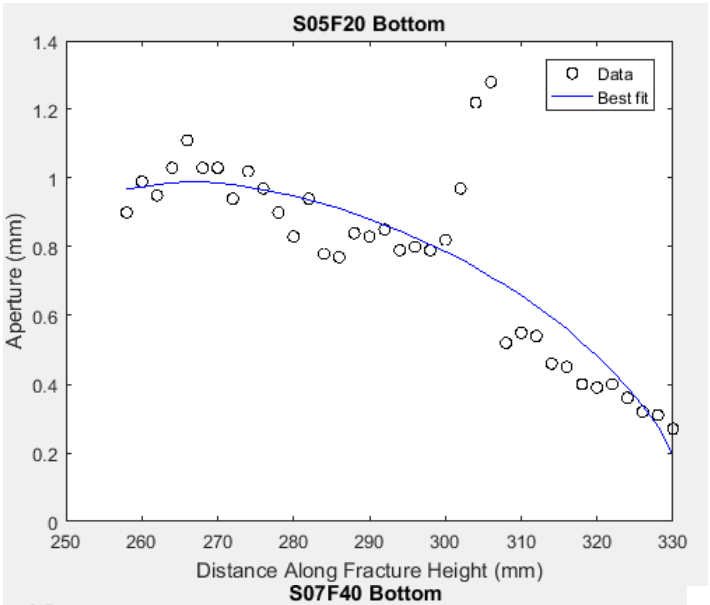


```
Name =

S05F20


Type =

Bottom


ans =

          results
    a      65.908
    b     0.98869
    c      266.87
    n      1.6674
    R2    0.70572
```

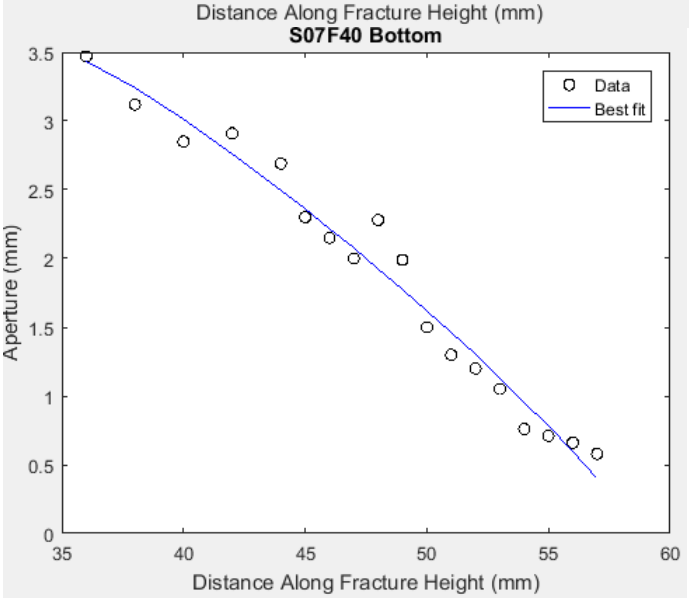


```
Name =

S07F40


Type =

Bottom


ans =

          results
    a      22.773
    b      3.4343
    c      35.973
    n      1.1392
    R2    0.97089
```

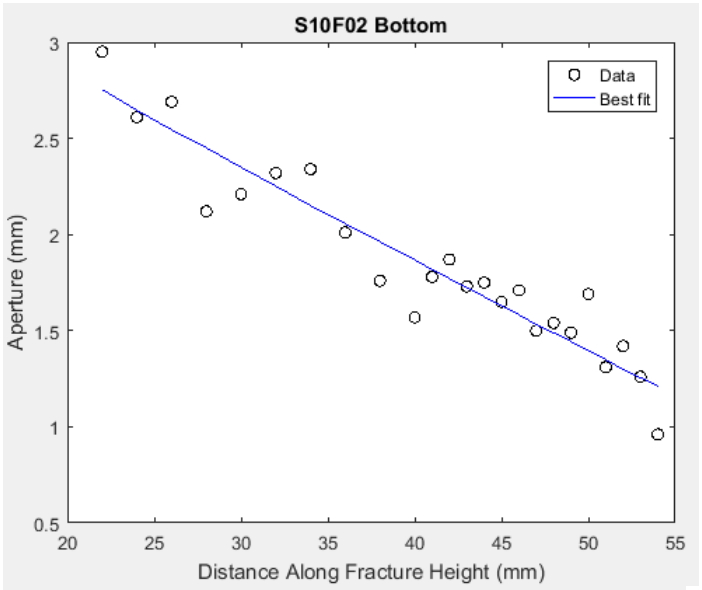


```
Name =

S10F02


Type =

Bottom


ans =

          results
    a      59.468
    b      2.7572
    c          22
    n     0.96684
    R2    0.89532
```

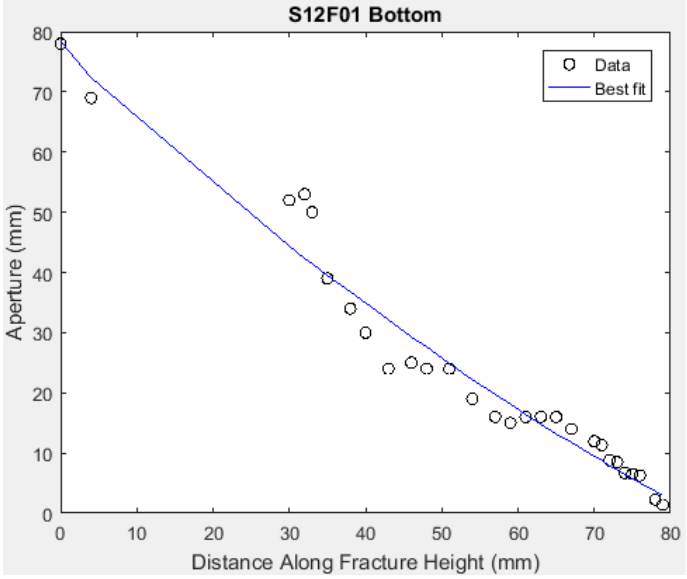


```
Name =

S12F01


Type =

Bottom


ans =

          results
    a      83.969
    b      78.257
    c           0
    n     0.89438
    R2     0.9573
```

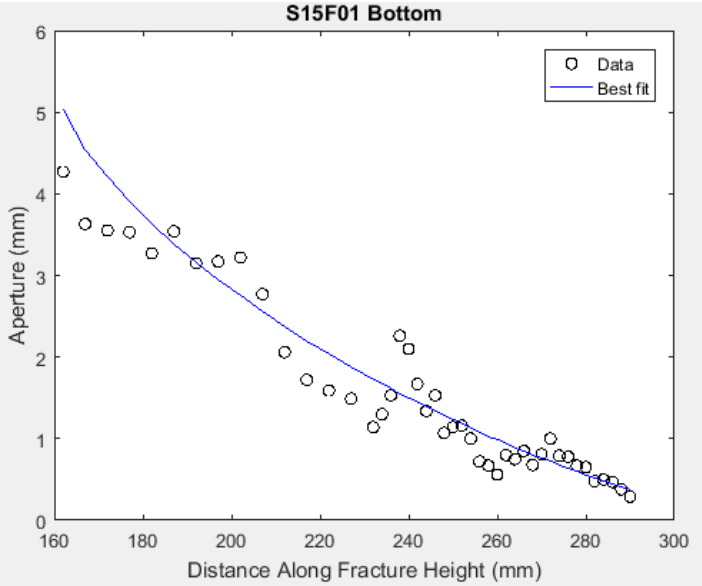


```
Name =

S15F01


Type =

Bottom


ans =

          results
    a      159.92
    b      5.1205
    c      161.62
    n      0.73163
    R2     0.90037
```

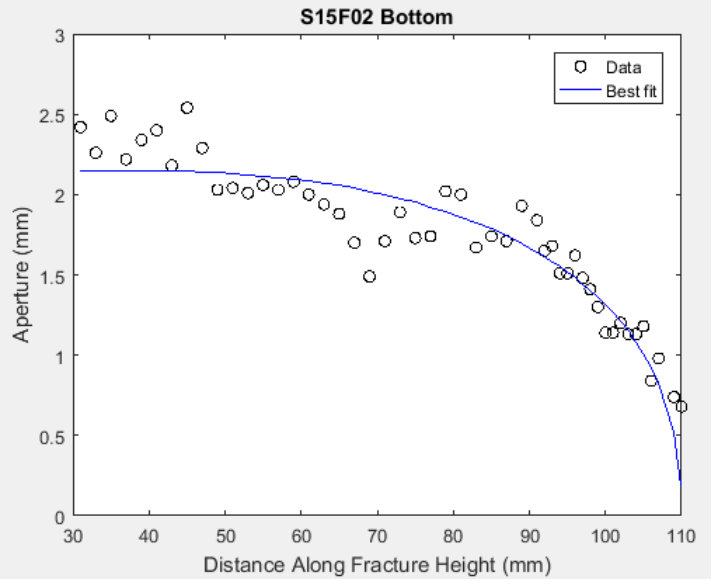


```
Name =

S15F02


Type =

Bottom


ans =

          results
    a      75.289
    b      2.151
    c      34.638
    n      2.4728
    R2     0.83386
```

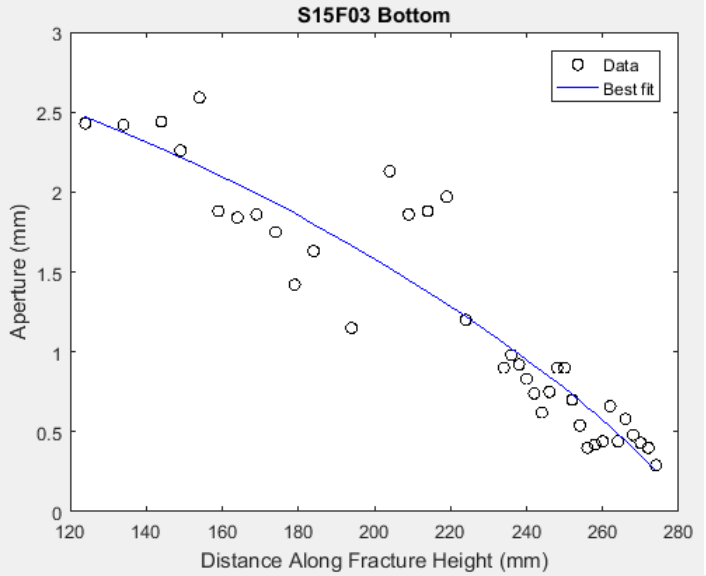


```
Name =

S15F03


Type =

Bottom


ans =

          results
    a      183.65
    b      2.6508
    c      98.152
    n      1.2544
    R2     0.87267
```

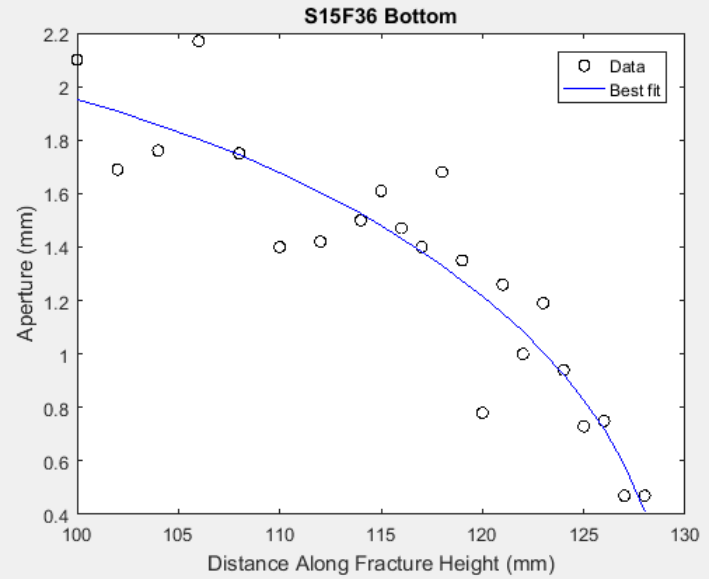


```
Name =

S15F36


Type =

Bottom


ans =

          results
    a      52.582
    b      2.186
    c      76.362
    n      1.9947
    R2     0.84618
```

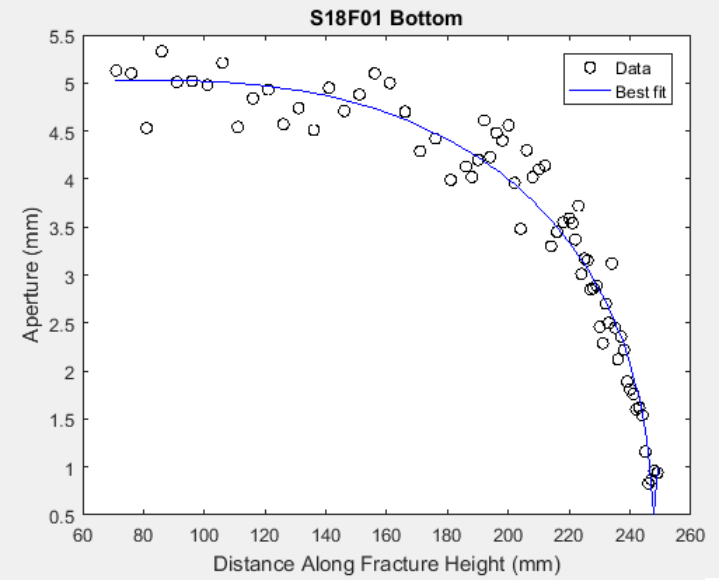


```
Name =

S18F01


Type =

Bottom


ans =

          results
    a      168.64
    b      5.0306
    c      79.132
    n      2.4867
    R2     0.95397
```

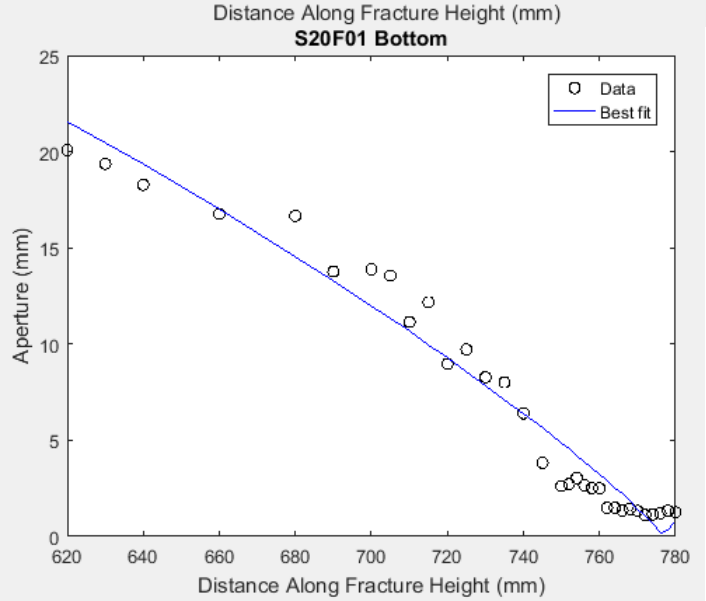


```
Name =

S20F01


Type =

Bottom


ans =

          results
    a      201.72
    b      25.624
    c      575.04
    n      1.1394
    R2     0.96293
```

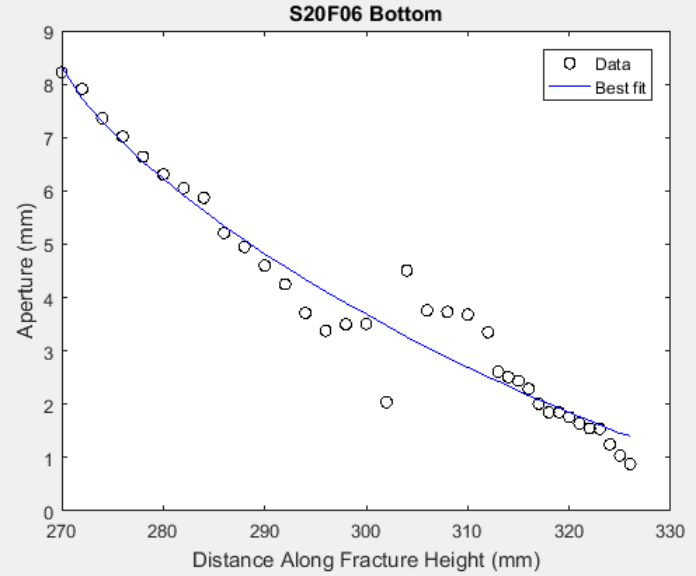


```
Name =

S20F06


Type =

Bottom


ans =

          results
    a       84.25
    b       8.535
    c       269.58
    n      0.74704
    R2     0.94265
```

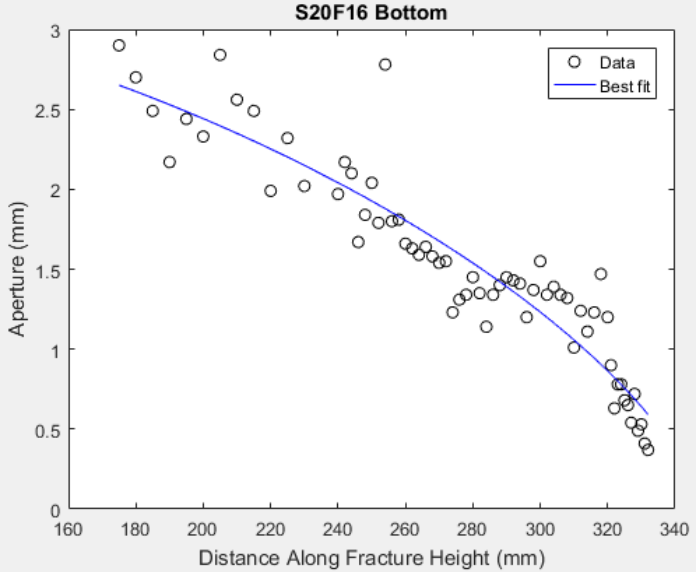


```
Name =

S20F16


Type =

Bottom


ans =

          results
    a       283.29
    b       3.1999
    c       63.949
    n       1.4986
    R2     0.87274
```

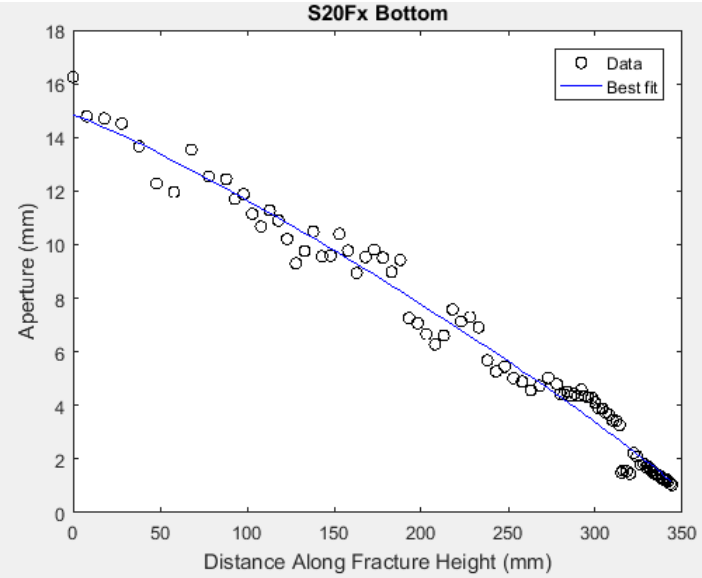


```
Name =

S20Fx


Type =

Bottom


ans =

          results
    a      362.56
    b      14.836
    c           0
    n      1.1179
    R2    0.97927
```

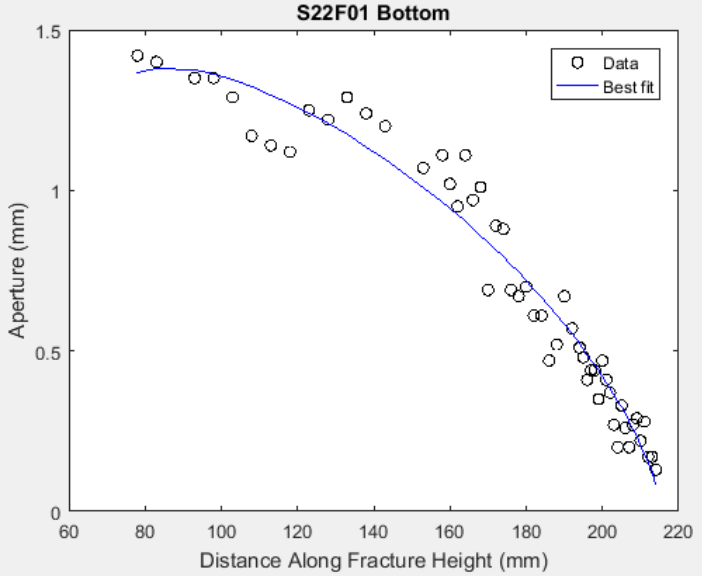


```
Name =

S22F01


Type =

Bottom


ans =

          results
    a      127.96
    b      1.3851
    c      87.382
    n      1.4763
    R2     0.9538
```

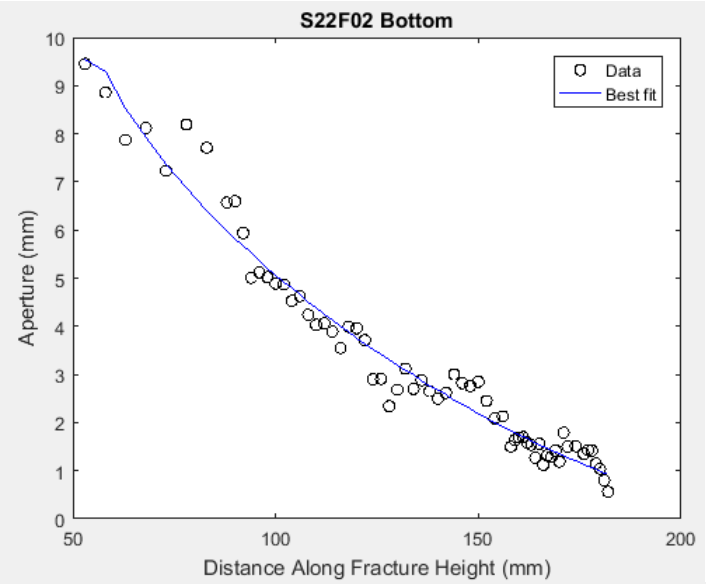


```
Name =

S22F02


Type =

Bottom


ans =

          results
    a      167.44
    b      10.097
    c      54.874
    n     0.71755
    R2    0.96618
```

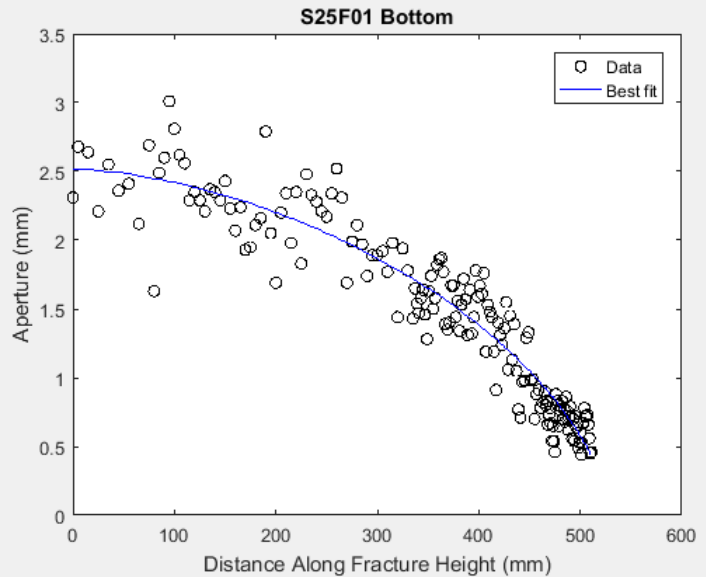


```
Name =

S25F01


Type =

Bottom


ans =

          results
    a      528.11
    b      2.5152
    c           0
    n       1.662
    R2    0.90269
```

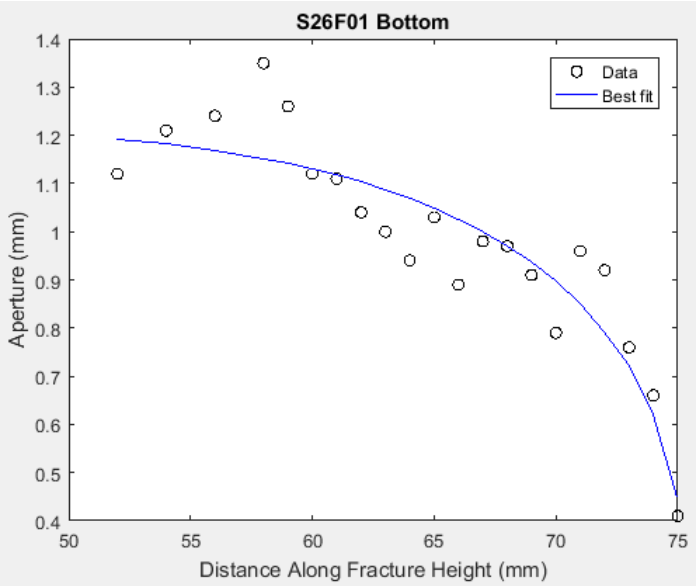


```
Name =

S26F01


Type =

Bottom


ans =

          results
    a       40.02
    b      1.2154
    c       35.503
    n      3.2007
    R2    0.83136
```

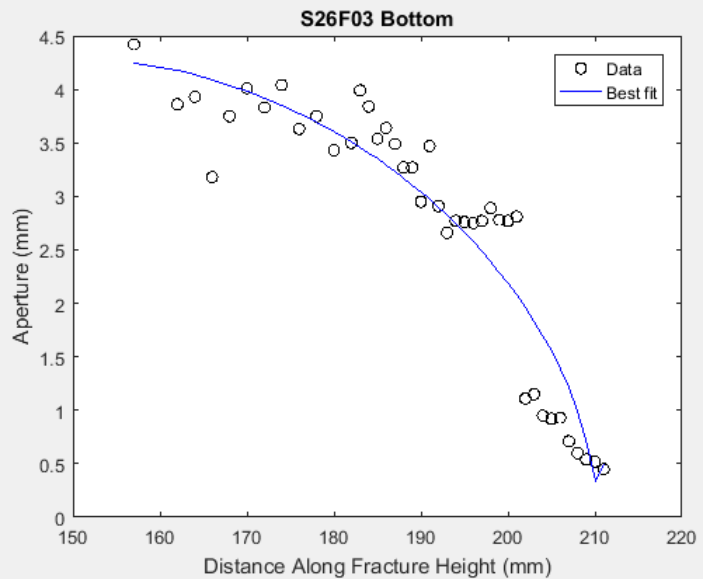


```
Name =

S26F03


Type =

Bottom


ans =

          results
    a       58.933
    b       4.2794
    c       151.39
    n       1.8181
    R2    0.88886
```

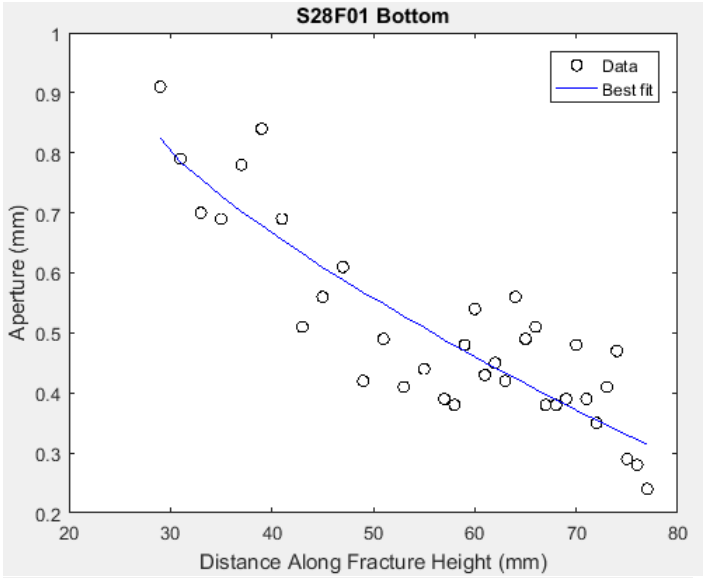


```
Name =

S28F01


Type =

Bottom


ans =

          results
    a      97.253
    b     0.82334
    c          29
    n     0.83589
    R2    0.76021
```

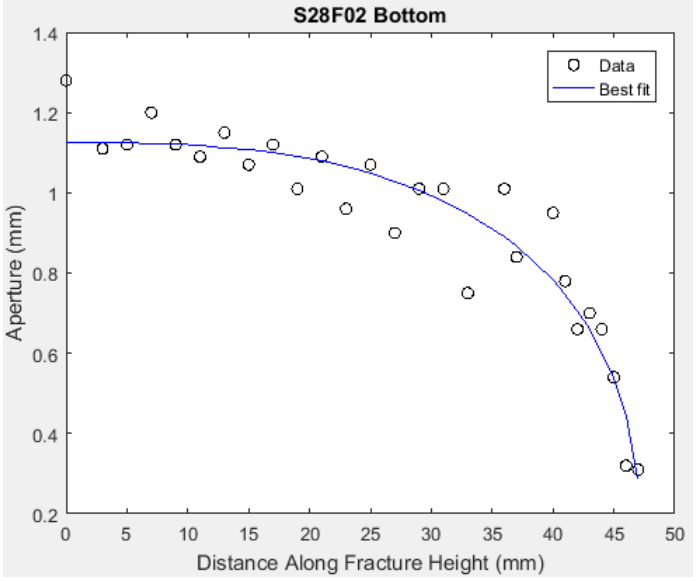


```
Name =

S28F02


Type =

Bottom


ans =

          results
    a      47.421
    b      1.1253
    c           0
    n      2.7224
    R2    0.89443
```

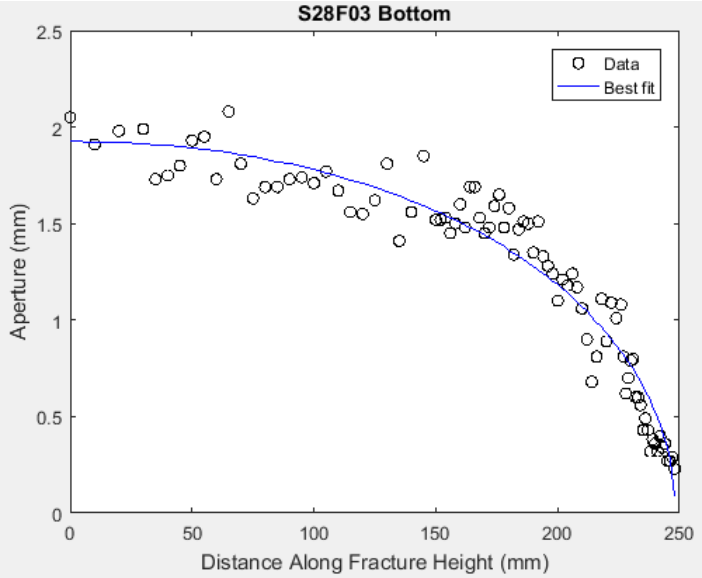


```
Name =

S28F03


Type =

Bottom


ans =

          results
    a      248.19
    b      1.9244
    c           0
    n      2.0813
    R2     0.93273
```

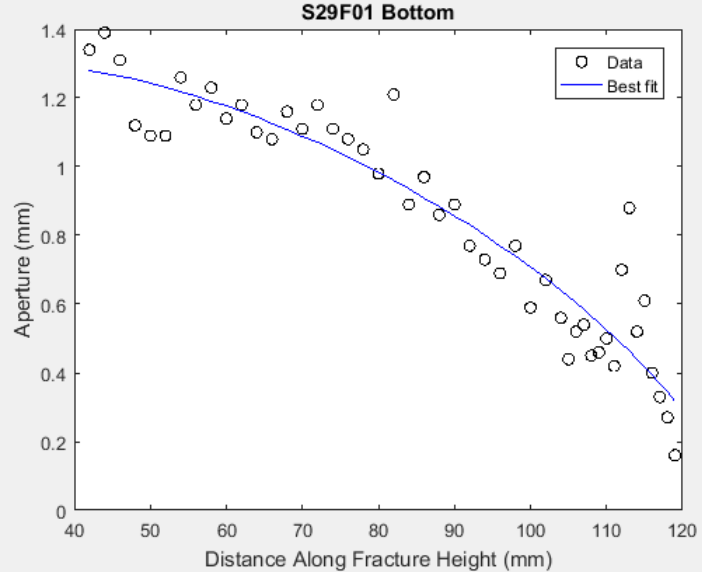


```
Name =

S29F01


Type =

Bottom


ans =

          results
    a      87.945
    b      1.2859
    c      38.727
    n      1.4766
    R2     0.8818
```

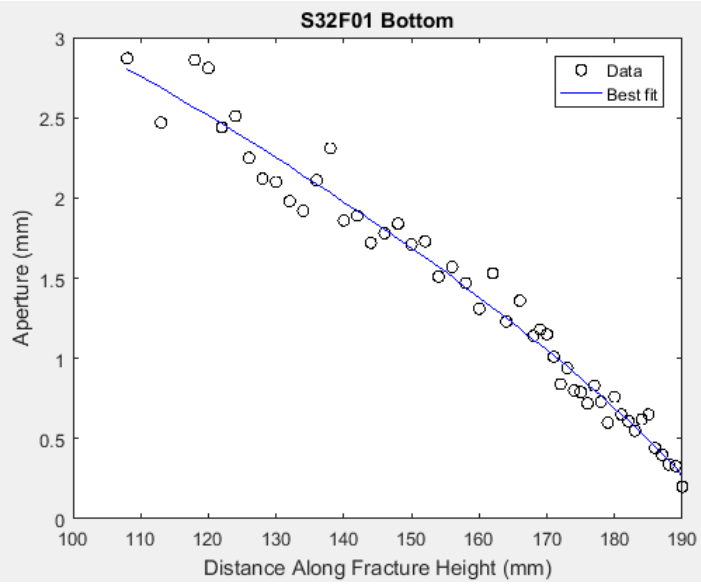


```
Name =

S32F01


Type =

Bottom


ans =

           results
    a          160
    b       4.1761
    c       34.559
    n       1.2246
    R2     0.97198
```

CURVE FITTING RESULT: TOP TIPS OF FRACTURES FROM HAND SAMPLES

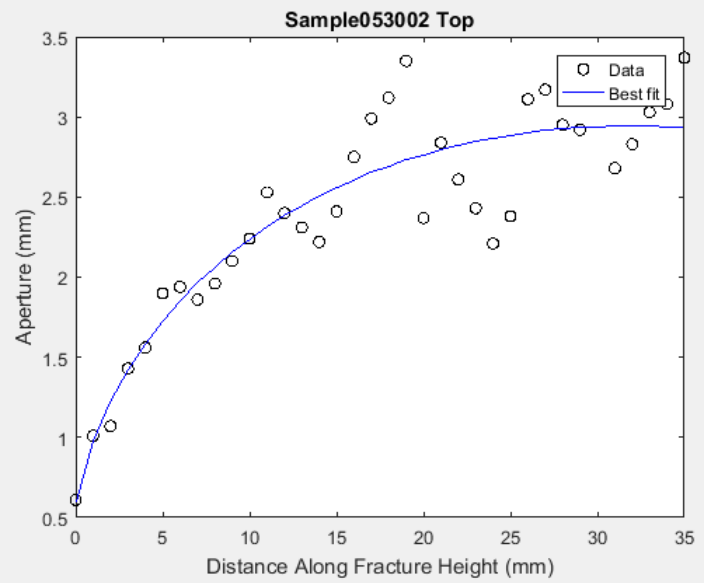


```
Name =

Sample053002


Type =

Top


ans =

           results
    a       32.545
    b       2.9414
    c           32
    n        2.106
    R2     0.84535
```

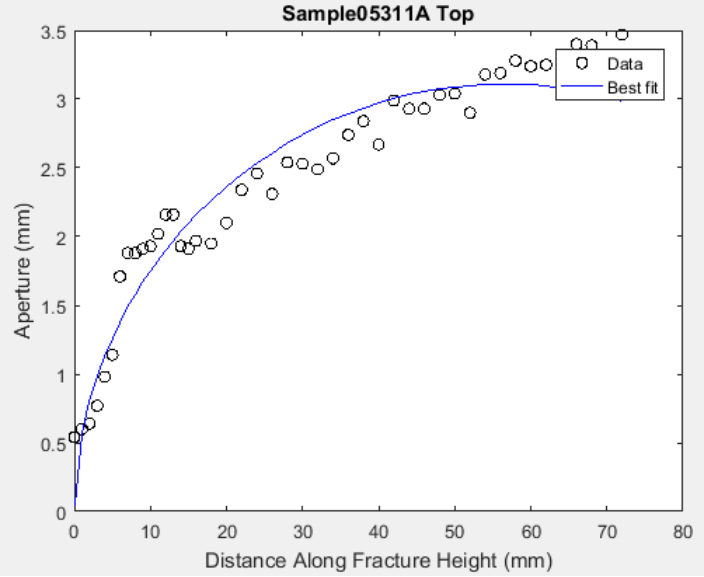


```
Name =

Sample05311A


Type =

Top


ans =

           results
    a       56.314
    b       3.1115
    c        56.32
    n       1.9758
    R2     0.91825
```

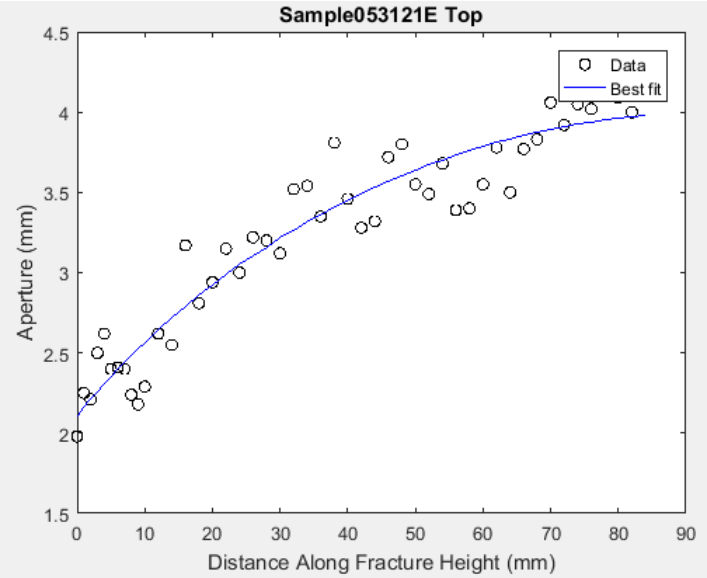


```
Name =

Sample053121E


Type =

Top


ans =

          results
    a     110.18
    b     3.9885
    c     89.999
    n     1.8379
    R2    0.9093
```

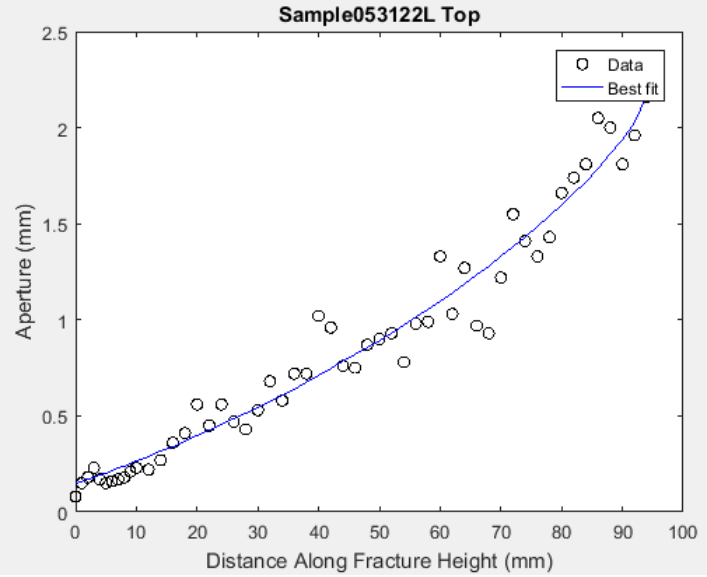


```
Name =

Sample053122L


Type =

Top


ans =

          results
    a      113.23
    b      2.1601
    c      94.003
    n     0.75864
    R2    0.95819
```

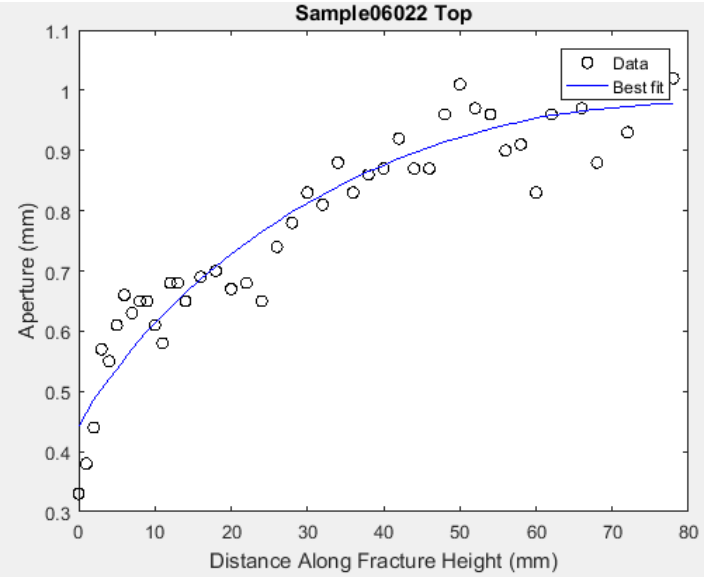


```
Name =

Sample06022


Type =

Top


ans =

           results
    a       89.689
    b      0.97759
    c           80
    n       2.0063
    R2      0.9042
```

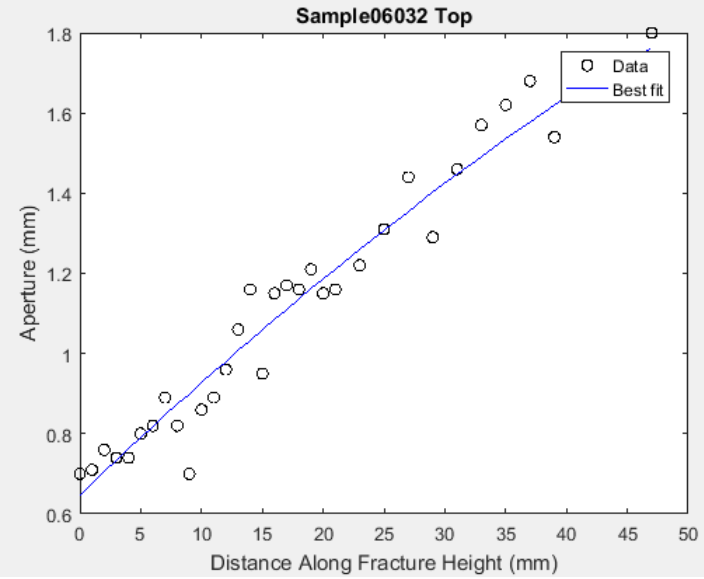


```
Name =

Sample06032


Type =

Top


ans =

           results
    a       66.134
    b       1.7609
    c       47.106
    n       1.1382
    R2     0.95738
```

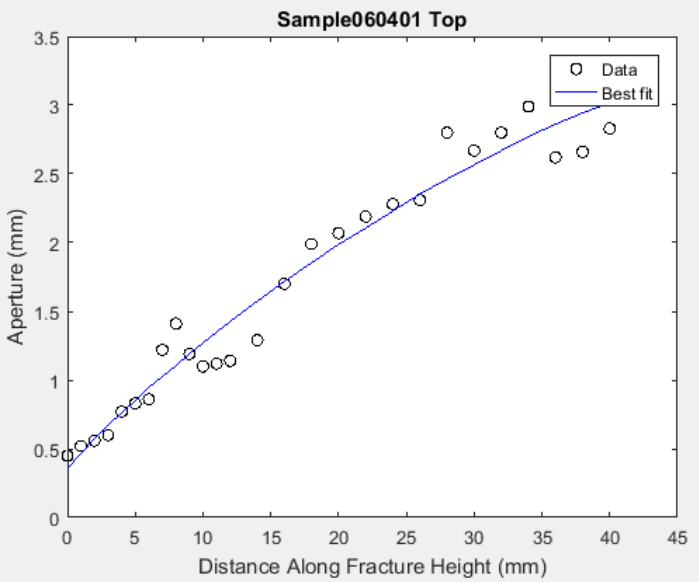


```
Name =

Sample060401


Type =

Top


ans =

          results
    a      44.602
    b      3.0722
    c      42.043
    n      1.2373
    R2    0.96147
```

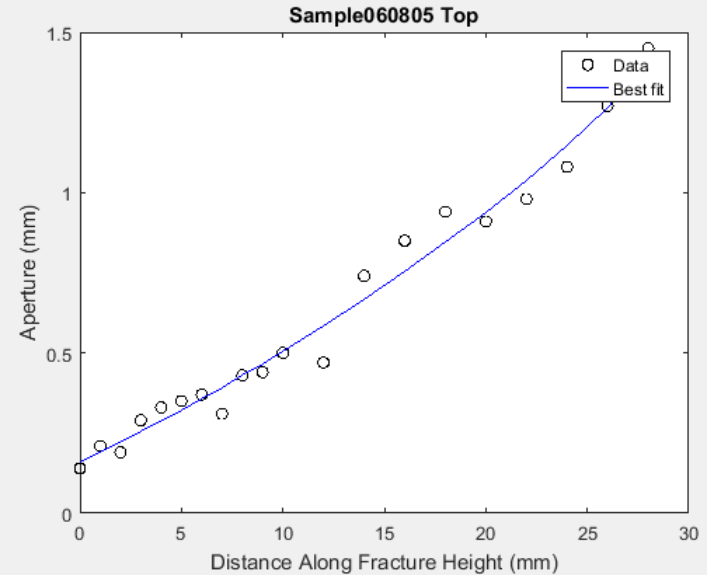


```
Name =

Sample060805


Type =

Top


ans =

          results
    a      34.417
    b      1.4172
    c          28
    n      0.8416
    R2    0.97863
```

CURVE FITTING RESULT: BOTTOM TIPS OF FRACTURES FROM HAND SAMPLES

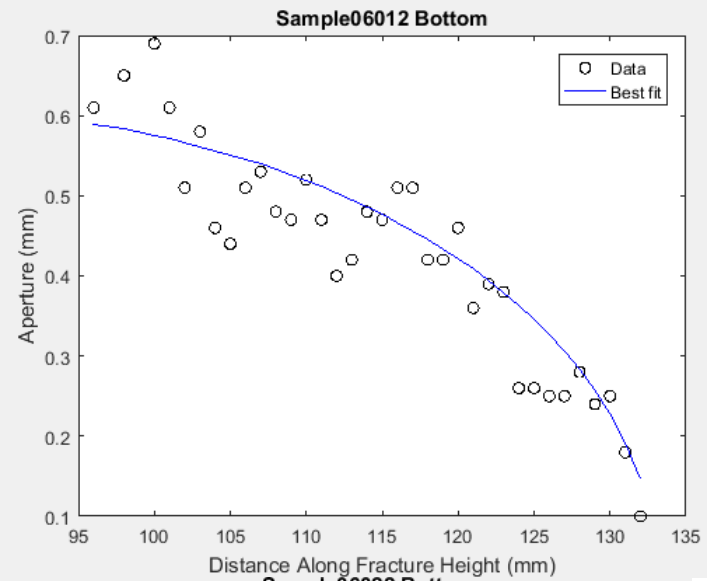


```
Name =

Sample06012


Type =

Bottom


ans =

          results
    a      52.261
    b     0.61142
    c      81.002
    n      2.0963
    R2    0.83168
```

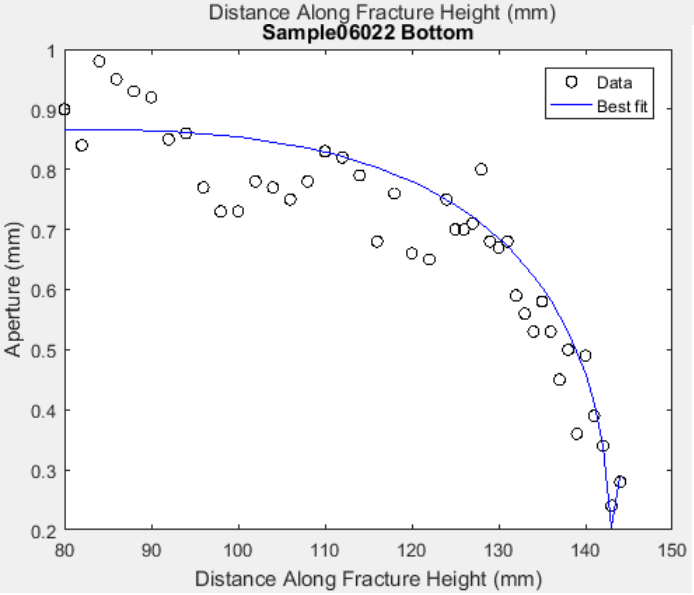


```
Name =

Sample06022


Type =

Bottom


ans =

          results
    a      69.136
    b     0.86705
    c       74.12
    n      3.0928
    R2    0.85594
```

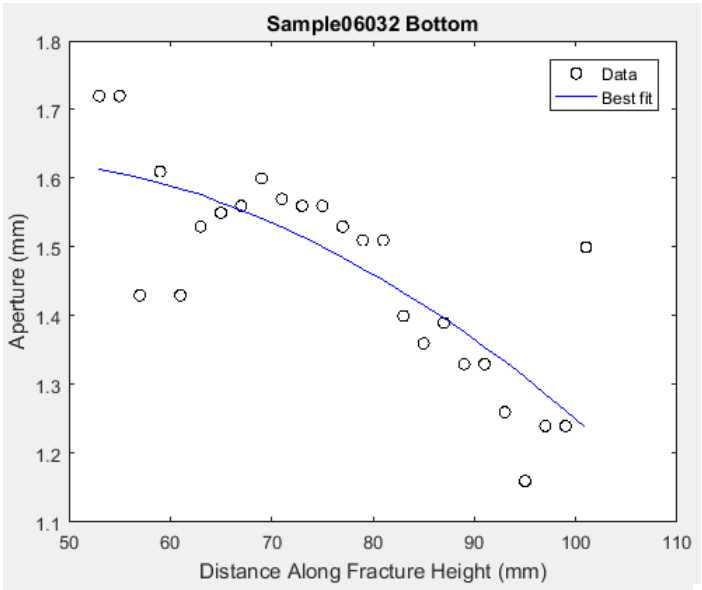


```
Name =

Sample06032


Type =

Bottom


ans =

           results
    a       99.982
    b       1.6187
    c       49.118
    n       1.6028
    R2     0.60999
```

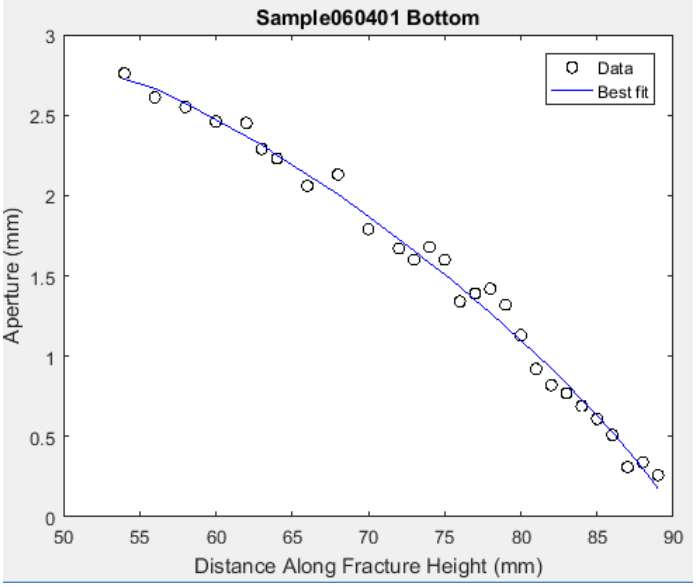


```
Name =

Sample060401


Type =

Bottom


ans =

           results
    a       36.153
    b       2.7325
    c       53.805
    n       1.2288
    R2     0.98985
```

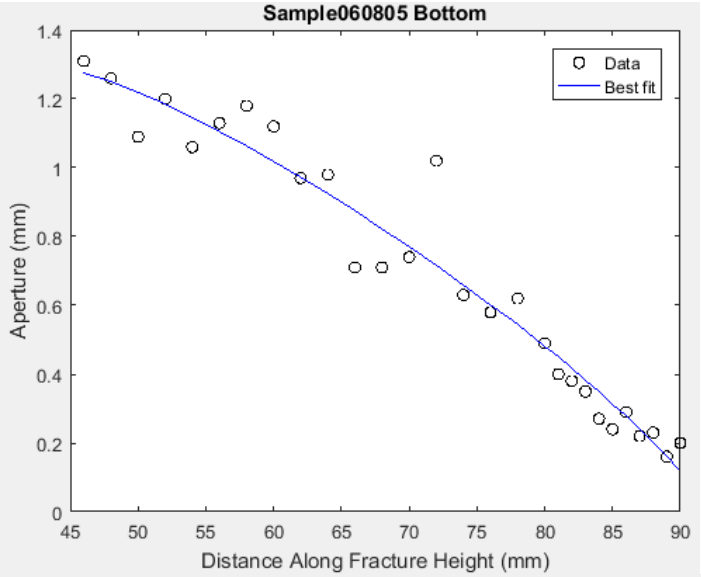


```
Name =

Sample060805


Type =

Bottom


ans =

           results
    a       46.401
    b       1.2784
    c       45.807
    n       1.2053
    R2     0.94549
```

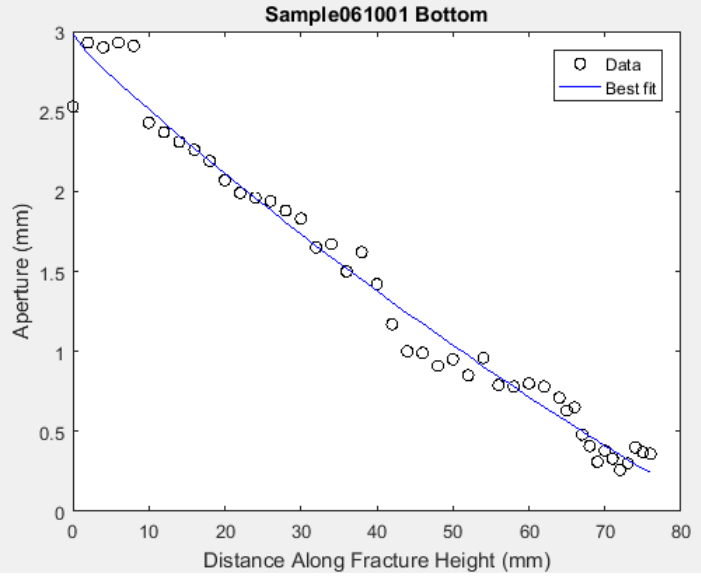


```
Name =

Sample061001


Type =

Bottom


ans =

           results
    a        85.54
    b       2.9767
    c            0
    n      0.90601
    R2     0.97635
```

CURVE FITTING RESULT: TOP TIPS OF FRACTURES FROM THIN SECTIONS

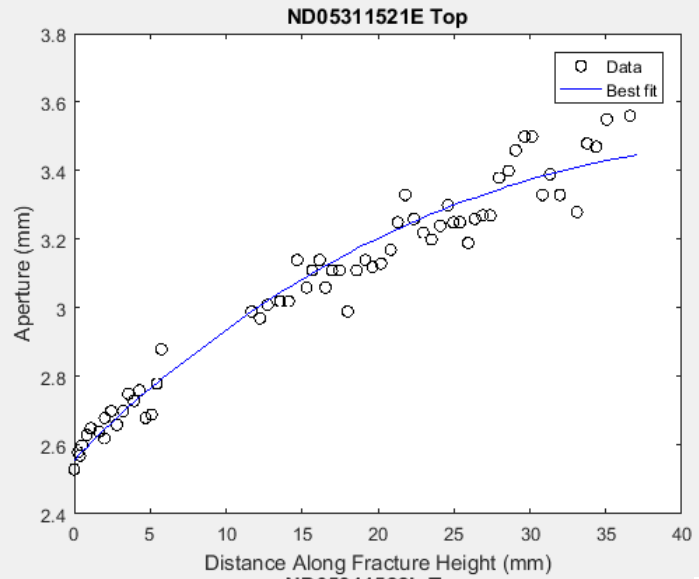


```
Name =

ND05311521E


Type =

Top


ans =

           results
    a       69.313
    b       3.4786
    c       45.926
    n        1.943
    R2     0.95113
```

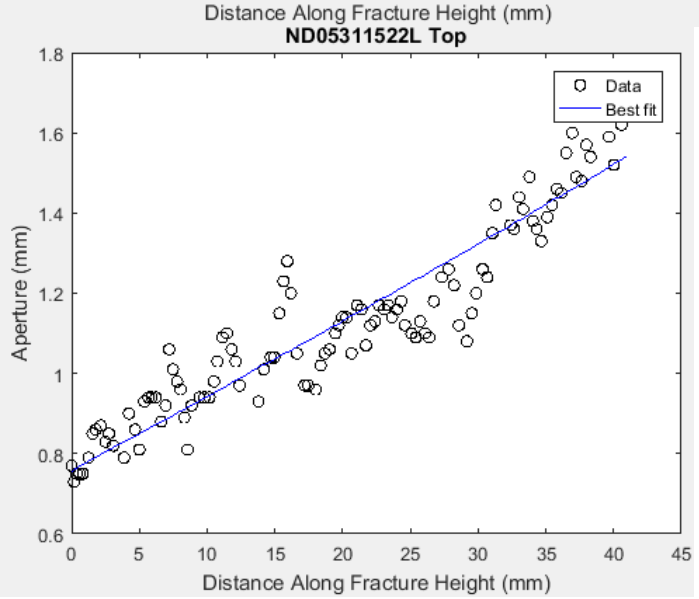


```
Name =

ND05311522L


Type =

Top


ans =

           results
    a       84.079
    b       1.5428
    c       40.971
    n      0.96913
    R2      0.8752
```

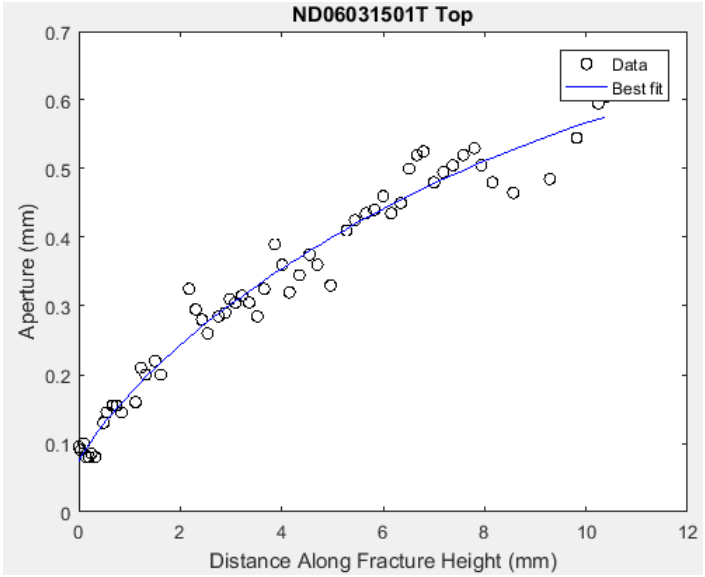


```
Name =

ND06031501T


Type =

Top


ans =

           results
    a       14.142
    b      0.62448
    c       13.746
    n       1.4991
    R2     0.96709
```

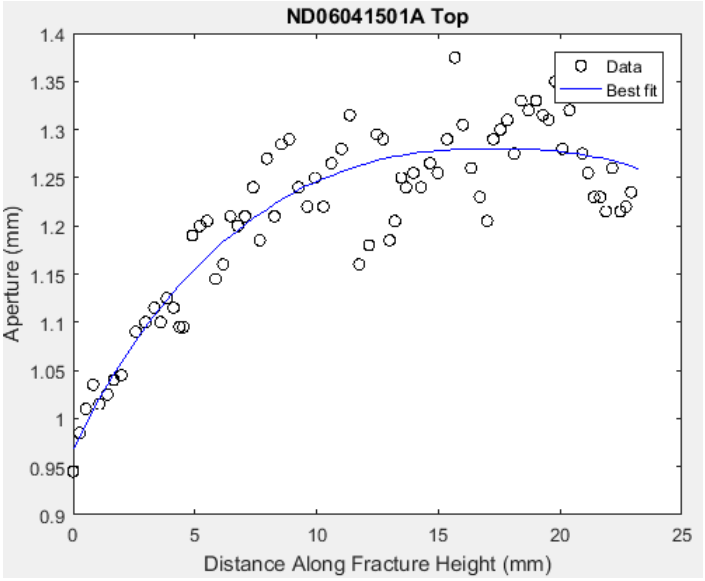


```
Name =

ND06041501A


Type =

Top


ans =

           results
    a       23.443
    b       1.2803
    c       17.289
    n       2.3724
    R2      0.8228
```

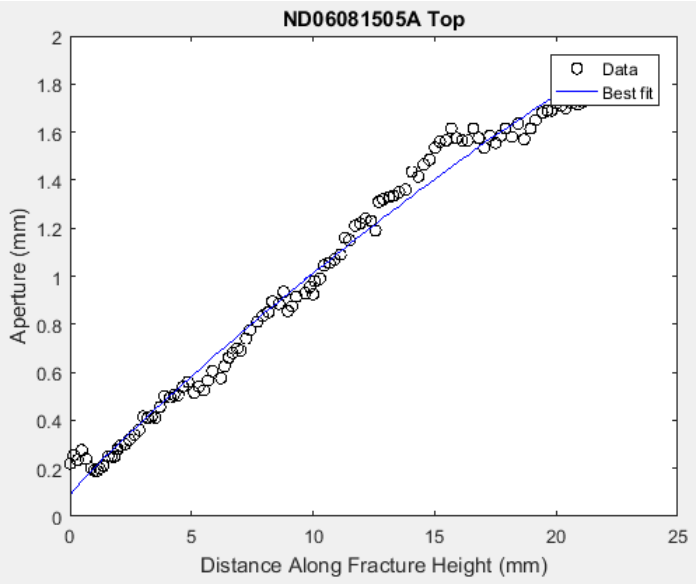


```
Name =

ND06081505A


Type =

Top


ans =

          results
    a      23.056
    b      1.8874
    c      22.318
    n      1.1092
    R2     0.98646
```

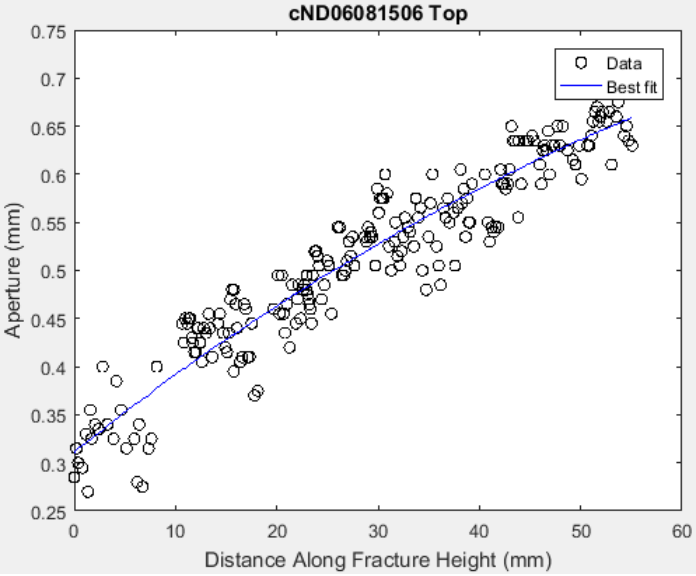


```
Name =

cND06081506


Type =

Top


ans =

          results
    a         102
    b      0.72677
    c       75.934
    n       1.3272
    R2     0.90264
```

CURVE FITTING RESULT: BOTTOM TIPS OF FRACTURES FROM THIN SECTIONS

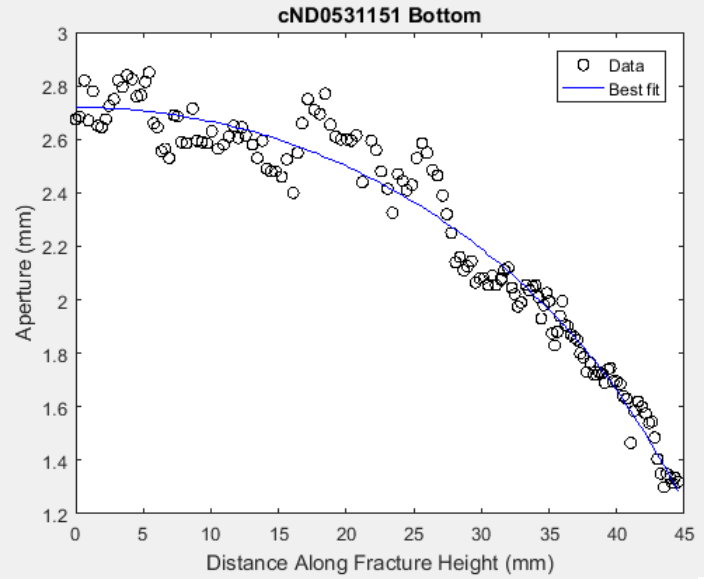


```
Name =

cND0531151


Type =

Bottom


ans =

          results
    a      50.446
    b      2.7191
    c           0
    n      2.0067
    R2     0.9609
```

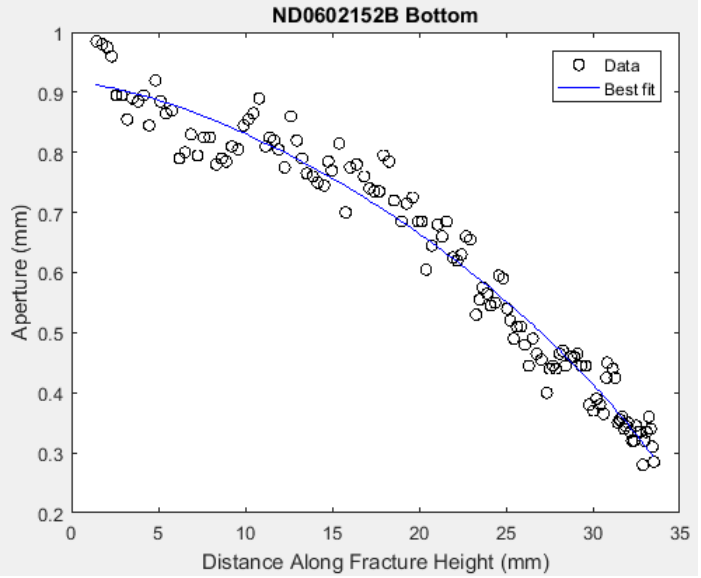


```
Name =

ND0602152B


Type =

Bottom


ans =

          results
    a      38.429
    b      0.91689
    c           0
    n      1.4831
    R2     0.96365
```

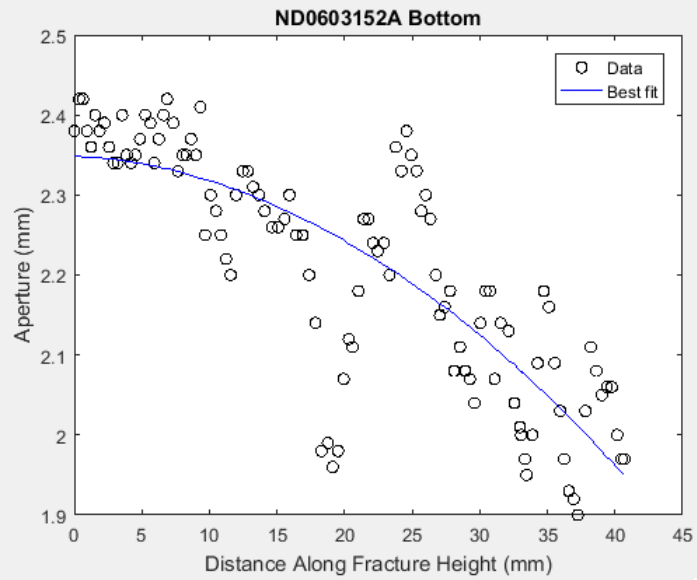


```
Name =

ND0603152A


Type =

Bottom


ans =

           results
    a           82
    b        2.348
    c            0
    n       1.7959
    R2     0.64828
```

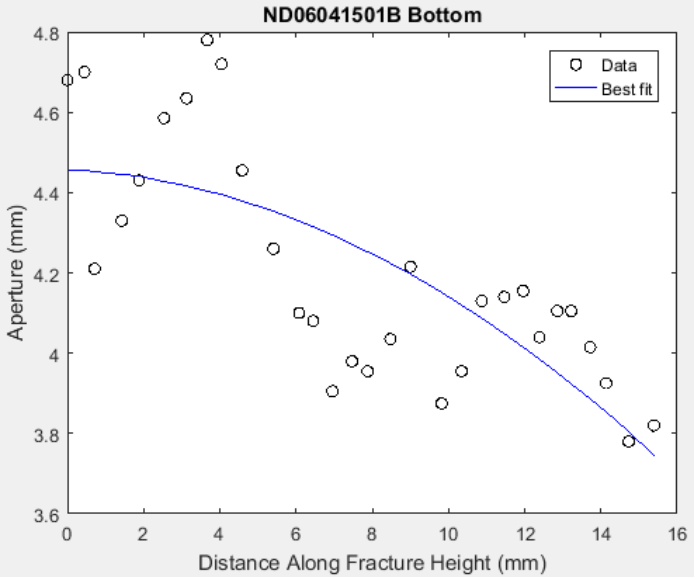


```
Name =

ND06041501B


Type =

Bottom


ans =

           results
    a           32
    b       4.4551
    c            0
    n       1.7987
    R2     0.51104
```

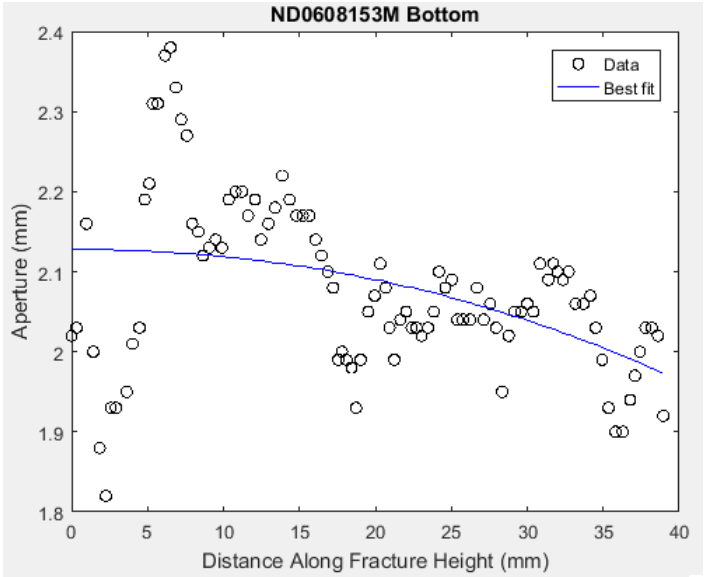


```
Name =

ND0608153M


Type =

Bottom


ans =

           results
    a       98.789
    b       2.1277
    c            0
    n       2.0747
    R2     0.18889
```

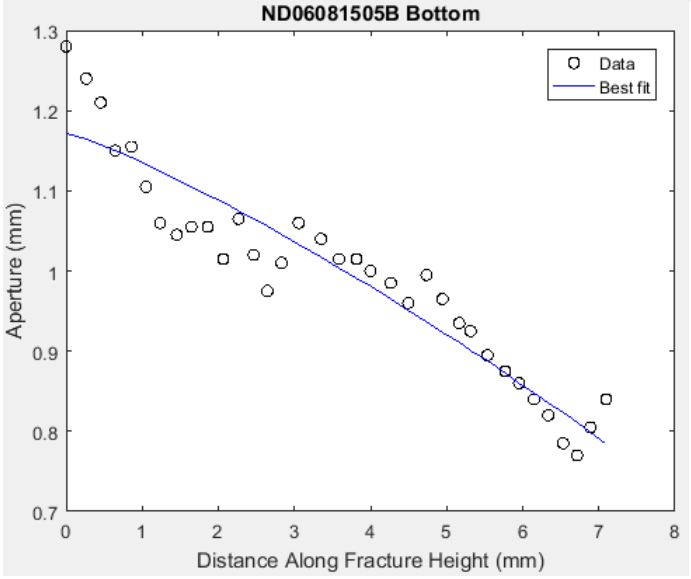


```
Name =

ND06081505B


Type =

Bottom


ans =

           results
    a           16
    b        1.171
    c            0
    n        1.193
    R2     0.87945
```

Appendix B: Petrographic Results

DETAILED DESCRIPTION OF THIN SECTIONS

Sample ND_053115_1A

The thin section includes the bottom tip of sample ND_05/31/15_1A from site 15. The orientation of the fracture is 160/80 (dip azimuth/dip), which is categorized as set 2 fracture. The tip is split into two micro-fractures of smaller sizes. The center of the fracture comprises mainly quartz cement, which the elongated quartz cement grows from both walls toward the center of the fracture (syntaxial fractures). Chlorite and magnetite are present at the tip of the fracture. Only isolated fluid inclusions are observed, rather than trail of fluid inclusion assemblages (FIAs) that record crack-seal events.

Sample ND_053115_1Ab

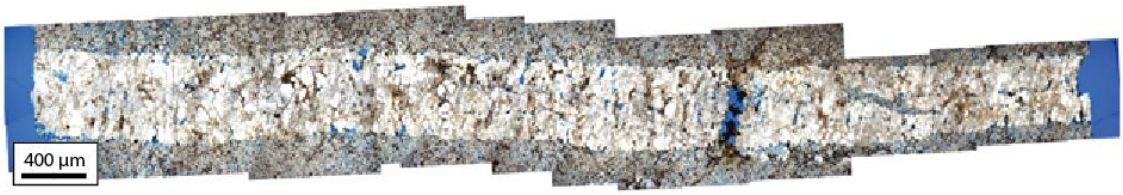

This sample is also from sample ND_05/31/15_1A from stop 15. It comes from the area of the fracture that is closer to the center than thin section ND_053115_1A. This thin section contains more pore space and dark magnetite and rutile, but less chlorite than sample ND_053115_1A. The fracture is cut by a smaller fracture at the area between the top and the center of the fracture, resulting in a void space that is partially filled with mafic minerals. The fluid inclusions in this sample are abundant but isolated, and crack-seal texture is absent.

Sample ND_053115_21E

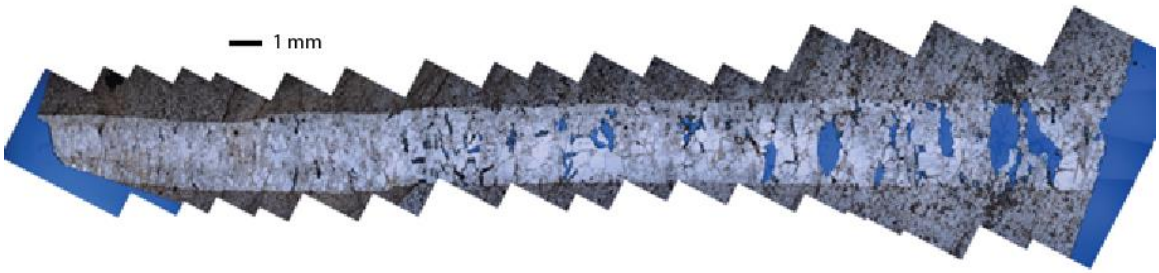

This thin section come from sample ND_05/31/15_2, collected at stop 15. The fracture belongs to set 2 and is orientated 152/83. The thin section contains mainly quartz cement with trace amount of magnetite, and chlorite. Crack-seal texture, marked by trails of FIAs that are parallel to fracture walls, is prominent toward the center of the fracture.

The fracture also contains multiple quartz cement bridges. Large pore spaces also present in the same region on the fracture. At the tip, the quartz cement is more blocky, and pore space is absent.

Sample ND_053115_22L

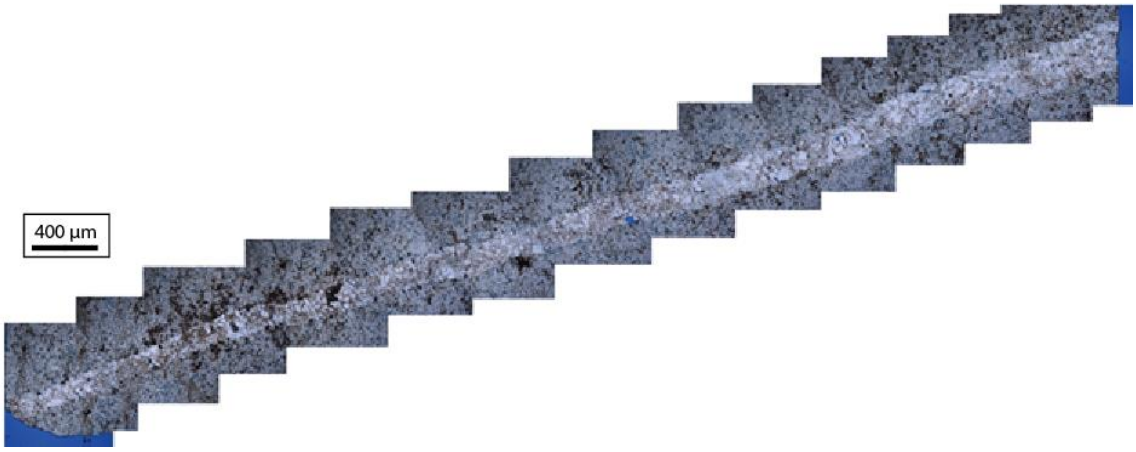

This thin section comes from the same sample with the thin section ND_053115_21E, but it contains a different fracture. The fracture belongs to set 1. The orientation of fracture is 131/83. The fracture is filled mostly with blocky quartz cement, with small percentages of chlorite, magnetite, rutile, and pore space. The inclusions are significantly less abundant compared to the previous thin section, and are scattering throughout the sample. No crack-seal FIA trails are present.

Sample ND_060215_2B

The thin section is made from the bottom tip of a fracture in sample ND_06/02/15_2 from stop 5. With its orientation of 304/60, the fracture belongs to set 1. The fracture is filled with quartz cement, with small amount of chlorite and magnetite. Crack-seal textures are prominent, as indicated by multiple trails of inclusions that align parallel to fracture walls in each cement bridge. Between areas of cementations are large pore spaces. The very tip of fracture is completely filled with cement, and also contains crack-seal FIAs.

Sample ND_060315_01M

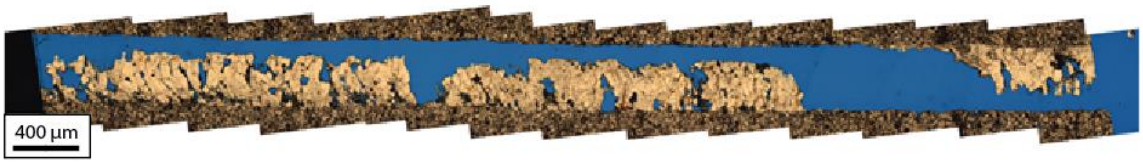

The aperture profile of this fracture was collected in the field before the fracture was taken as a hand sample and turned into this thin section. The fracture is fracture 06 of Stop 4. It belongs to set 1 fractures, with an orientation of 314/70. Note that the top and the bottom walls of fracture used to be connected by quartz cement bridges. The void

spaces close to fracture walls are induced after the sample is cut. The cement bridges consist mostly of quartz cement bridges, with small percentages of chlorite and mafic minerals. Multiple lines of FIAs that are parallel to fracture walls indicate a series of crack-seal intervals.

Sample ND_060315_01T

This thin section is the top tip of fracture 06 of Stop 4, continuing from the previous thin section. The tip of the fracture is split into two smaller tips, with one of them continuing to grow and occuring in an en-echelon pattern with two other micro-fractures. En-echelon is the term used to describe the case where a tip of fracture is parallel and offsets relative to the tips of the other fractures. The fracture is filled with quartz cement, chlorite, magnetite, and rutile. Crack-seal texture is also present throughout the fracture, including at the very tip. Parallel lines of FIAs are present not only at the largest part of the fracture, but also at the small fracture tip.

Sample ND_060315_2A

This thin section is made from a fracture in sample ND_06/03/15_2 from stop 18. The fracture's orientation is 170/54, and belongs to set 2. The cement is mainly blocky quartz with no indication of growth direction. It also contains a small amount of dark minerals and pore spaces. The inclusions are not as abundant as in other thin sections. They are small, scattering throughout, and do not display crack-seal texture.

Sample ND_060415_1A

This thin section is the bottom tip of the fracture in sample ND_06/04/15_1 from stop 24, which belongs to set 2. The orientation of fracture is 178/41. The most interesting feature of this thin section is the inclusion trails that are both parallel and perpendicular to fracture walls, which indicates that fracture walls might have collapsed. Cement that fills the fracture consists mostly of quartz crystals that grow toward the center. The void spaces are present throughout the length of the fracture. The two fracture tips are almost connected on the right of the image, suggesting that the fracture could have formed by coalescence or linkage of two en-echelon fractures.

Sample ND_060815_3M

This thin section comes from stop 28. The fracture ND_060815_3M is part of fracture set 3, with an orientation of 232/78. This thin section is different from the others. Besides quartz, the cement consists of large percentages of calcite and chlorite cement. The dark green chlorite and the twinning calcite are prominently visible under a petrographic microscope, and fill the spaces between quartz cement bridges. The inclusions align horizontally with respect to fracture walls, in the form of trails of FIAs, which is indicative of crack-seal texture. Both calcite and quartz cement contain inclusions, but I only determined homogenization temperature of inclusions in quartz cement. Pore space is not observed in the fracture.

Sample ND_060815_05A

This thin section is the top tip of fracture ND_06/08/15_05, collected from stop 29. The fracture orientation is 25/80, which is categorized as a set 3 fracture. The fracture is filled with quartz cement, with small percentages of black magnetite and greenish-brown chlorite and pore spaces. The cement is blocky, and aligns diagonally to fracture walls. The diagonal cement could have resulted from the fracture being stretched. The fracture surface might cut through previously precipitated material or through the wall rock, resulting in no systematic trend in the localization of newly precipitated cement. The most noticeable characteristic of this fracture tip is the rapid tapering of the fracture tip, which results in the triangular-shaped tip. A small fracture also grows out of the main fracture at the point where the main fracture starts to taper rapidly. The smaller fracture is partially cemented. The top tip, on the other hand, is fully cemented. Since cementation can completely fill a narrow fracture faster than a larger one, the small fracture might have formed long after the top main tip had been partially or completely filled with cement.

Sample ND_060815_05B

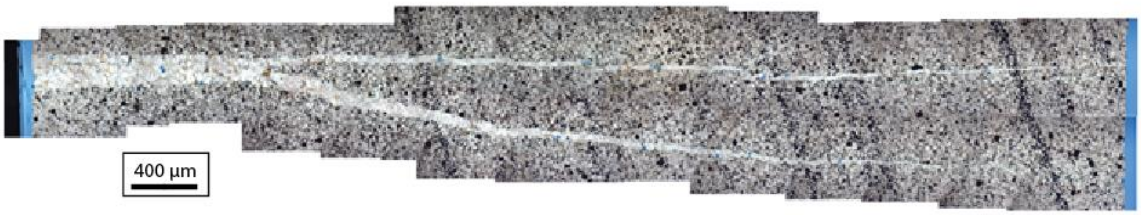

Similar to the previous sample, this thin section comes from fracture ND_06/08/15_05. It is the bottom tip of the fracture. The cement comprises mainly blocky quartz with a small amount of magnetite, rutile, and chlorite. The tip of the fracture is separated into two smaller fractures. Both the top and bottom tips are also filled with blocky quartz cement. The top tip occurs in an en-echelon pattern with another micro-scale fracture that is almost coalescent to another micro-fracture on the right of the picture.

Sample ND_060815_06M

The fracture in this thin section comes from sample ND_06/08/15_06, collected from site 29. The fracture belongs to set 3, with an orientation of 008/39. The cement is crack-seal, as indicated by horizontal alignments of chlorite, magnetite, and fluid inclusions that are parallel to fracture walls in the cement. The magnetite crystals are large and can be observed without a petrographic microscope. The fracture is completely filled with no pore space. Quartz cement is blocky, and cement bridges are not observed.

Sample ND_060815_06T

This thin section is the top tip of fracture ND_06/08/15_06, continuing from the previous sample. It is also completely filled with quartz, magnetite, and chlorite. Minerals and fluid inclusions also show crack-seal textures. Quartz bridges are not present. The quartz cement is blocky. The tip of the fracture is separated into two smaller tips. Both tips are completely filled with the same minerals as the main fracture, and the textures of the minerals are the same.

Appendix C: EDS Analysis Results

Based on the series of the overlay and spectral maps, the host rocks consist of quartz, chlorite, muscovite, orthoclase, rutile, magnetite, apatite, and ilmenite, from the most to the least abundant (Figure C1.1 and Table C1.1).

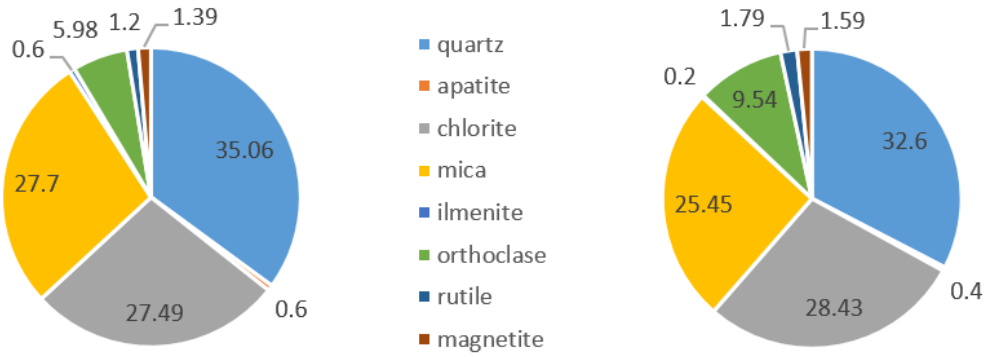

Figure C1: Pie charts showing composition of host rock from samples ND_060215_2B (left) and ND_060815_05B (right)

Minerals	Percentage of minerals in host rock		Averages
	ND_060215_2B	ND_060815_05B	
Quartz	35.06	32.60	32.60
Apatite	0.60	0.40	0.50
Chlorite	27.49	28.43	27.96
Mica	27.30	25.45	26.38
Orthoclase	6.36	9.54	7.95
Rutile	1.20	1.79	1.50
Magnetite	1.39	1.59	1.49
Ilmenite	0.60	0.20	0.40
Total	100.00	100.00	100.00

Table C1: Mineral percentages in the host rocks

Appendix D: Fluid Inclusion Microthermometry Results

Sample ND05311522L

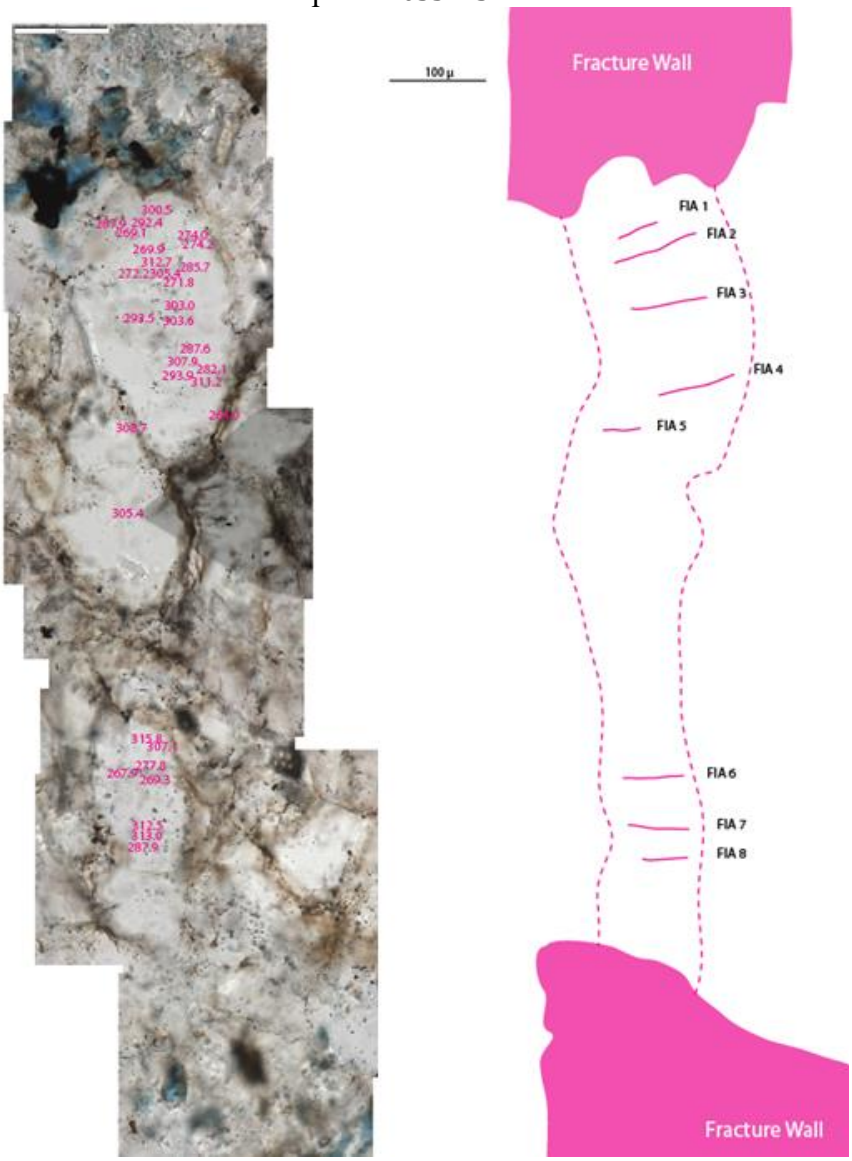

Figure D1: Homogenization temperatures and lines representing fluid inclusion assemblages of sample ND05311522L

Fluid inclusion assemblages line numbers (from top to bottom)	Homogenization temperatures (◦C)
1	269.1
	287.9
	292.4
	300.5
2	269.9
	274.0
	274.2
	285.7
	312.7
	272.2
3	303.0
	293.5
	303.6
4	287.6
	307.9
	282.1
	311.2
	293.9
5	264.0
	308.7
6	315.8
	307.1
	277.8
	267.9
	269.3
7	312.5
8	313.0
	287.9

Table D1: Homogenization temperatures of each fluid inclusion assemblage of sample ND05311522L

Sample ND06031501T

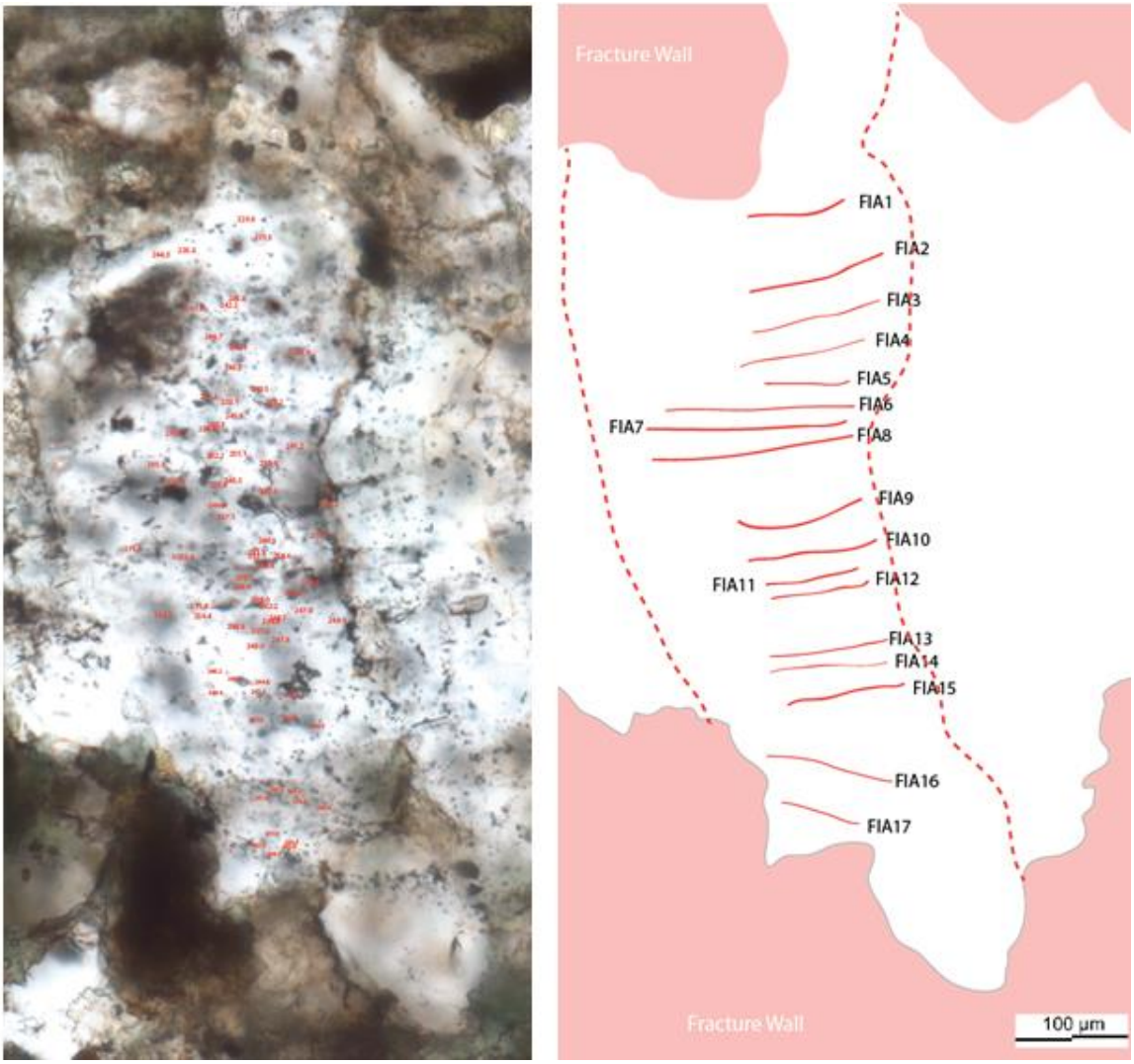

Figure D2: Homogenization temperatures and lines representing fluid inclusion assemblages of sample ND06031501T

Fluid inclusion assemblages line numbers (from top to bottom)	Homogenization temperatures (◦C)
1	229.9
	231.5
	235.0
	244.3
2	246.1
	242.2
	241.6
3	245.4
	246.7
4	247.8
	245.5
5	251.3
	233.1
	249.5
	239.2
6	250.3
	231.8
	250.2
7	250.3
	255.1
	252.2
	255.1
	245.2
8	253.9
	245.3
	255.9
	239.0
	257.1
	246.8
9	233.3
	219.7
	249.9
	251.9
	255.1
	255.4
	211.0

Table D2: Continued on next page

10	252.1
	248.0
	244.8
11	243.3
	256.4
	211.8
	258.0
	242.2
	253.0
	234.9
12	247.0
	248.7
	238.8
	249.6
	248.9
	247.6
	248.0
	257.6
13	246.2
	240.1
	249.4
	244.6
14	241.5
	236.0
15	255.9
	252.9
	249.5
16	241.8
	240.9
	243.2
	243.6
	246.8
17	253.3
	254.4
	253.6
	256.7
	257.5

Table D2: Homogenization temperatures of each fluid inclusion assemblage of sample ND06031501T

Sample cND0531151

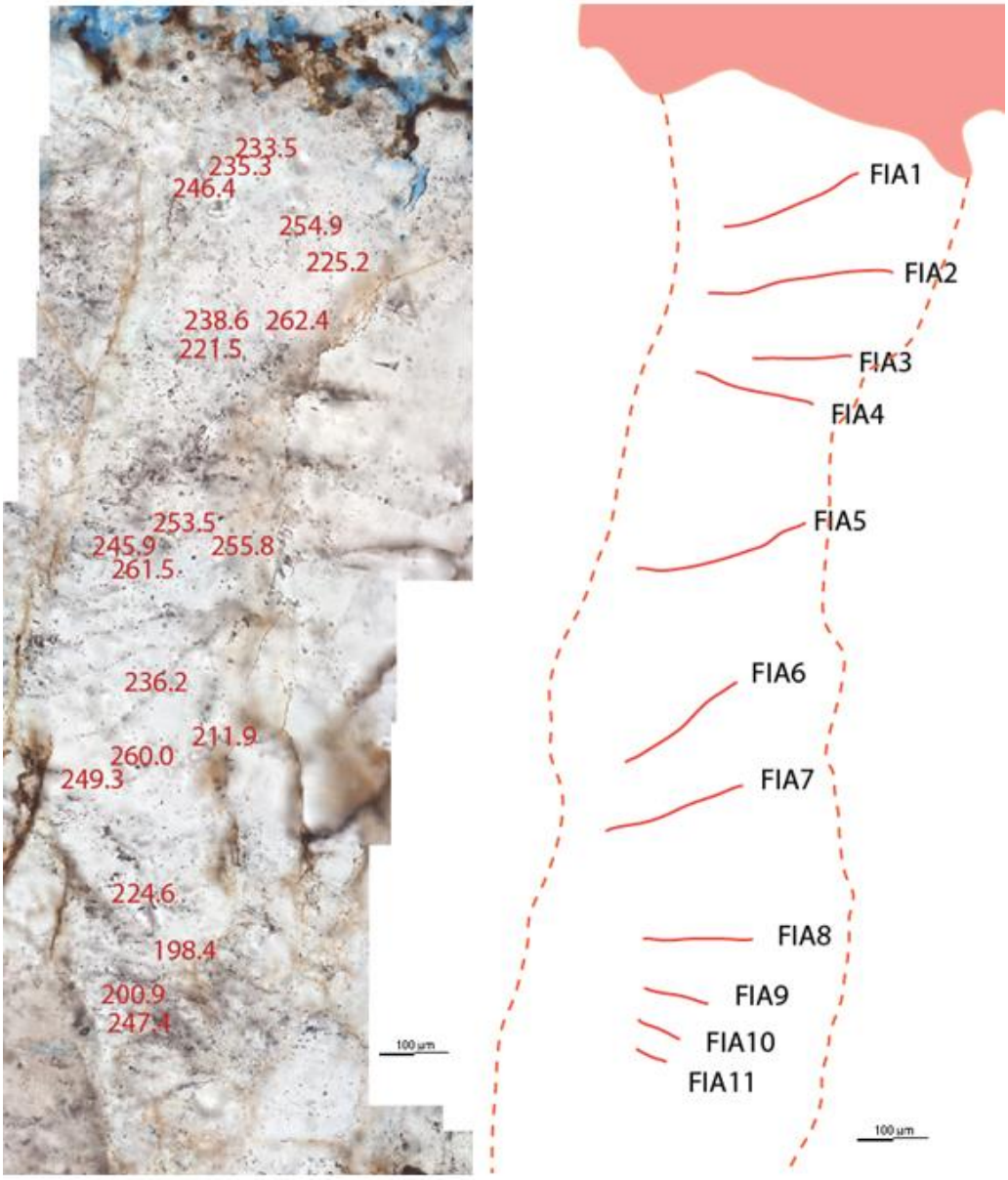

Figure D3: Homogenization temperatures and lines representing fluid inclusion assemblages of sample cND0531151

Fluid inclusion assemblages line numbers (from top to bottom)	Homogenization temperatures (◦C)
1	233.5
	235.3
	246.4
2	254.9
	225.2
3	238.6
	262.4
4	221.5
5	253.5
	255.8
	245.9
	261.5
6	236.2
7	211.9
	260.0
	249.3
8	224.6
9	198.4
10	200.9
11	247.4

Table D3: Homogenization temperatures of each fluid inclusion assemblage of sample cND0531151

Sample cND06081506

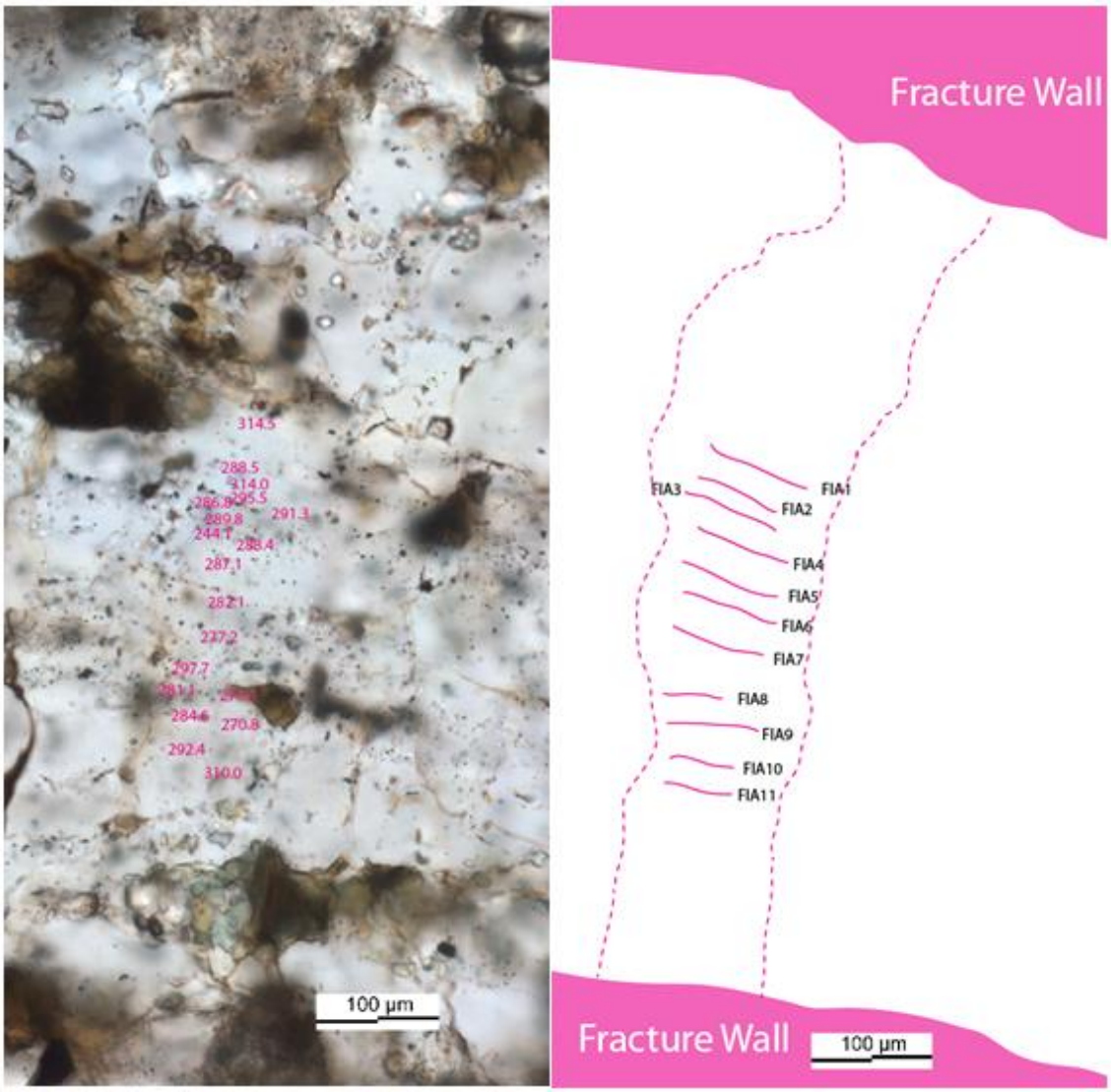

Figure D4: Homogenization temperatures and lines representing fluid inclusion assemblages of sample cND06081506

Fluid inclusion assemblages line numbers (from top to bottom)	Homogenization temperatures (◦C)
1	314.5
2	288.5
	314.0
3	295.5
	286.8
	291.3
4	289.8
	244.1
	288.4
5	287.1
6	282.1
7	277.2
8	297.7
	281.1
	273.1
9	284.6
	270.8
10	292.4
11	310.0

Table D4: Homogenization temperatures of each fluid inclusion assemblage of sample cND06081506

References

Alzayer, Y.A., 2014, Fracture growth kinematics in tight sandstone reservoirs [thesis].

Alzayer, Y., Eichhubl, P., and Laubach, S.E., 2015, Non-linear growth kinematics of opening-mode fractures: Journal of Structural Geology, v. 74, p. 31–44, doi: 10.1016/j.jsg.2015.02.003.

Anders, M. H., and Wiltschko, D. V., 1994, Microfracturing, paleostress and the growth of faults: Journal of Structural Geology, v. 16, no. 6, p. 795-815.

Anderson, T.L., 1995, Fracture mechanics: fundamentals and applications: Boca Raton, CRC Press.

Atkinson, B. K., 1980, Stress corrosion and the rate-dependent tensile failure of a fine-grained quartz rock: Tectonophysics, v. 65, no. 3, p. 281-290.

Atkinson, B.K., and Meredith, P.G., 1981, Stress corrosion cracking of quartz: A note on the influence of chemical environment: Tectonophysics, v. 77.

Atkinson, B. K., and Meredith, P. G., 1987, 4 – The theory of sub-critical crack growth with application to minerals and rocks, Fracture Mechanics of Rock: London, Academic Press, p. 111-166.

Atkinson, B.K., 1984, Subcritical crack growth in geological materials: J. Geophys. Res. Journal of Geophysical Research: Solid Earth, v. 89, p. 4077–4114.

Atkinson, B.K., 1987, Introduction to fracture mechanics and its geophysical applications, in Fracture mechanics of rock, London, Academic Press, p. 1–26.

Atkinson, B.K., 1989, The theory of subcritical crack growth with applications to minerals and rocks, in Meredith, P.G. ed., Fracture mechanics of rock, London, Academic Press, p. 111–1666.

Bahat, D., Bankwitz, P., and Bankwitz, E., 2004, The index of hackle raggedness on joint fringes: Geological Society, London, Special Publications, v. 231, no. 1, p. 103-116.

Bahat, D., and Engelder, T., 1984, Surface morphology on cross-fold joints of the Appalachian Plateau, New york and Pennsylvania: Tectonophysics, v. 104, no. 3, p. 299-313.

Barton, M.D., 2000, Overview of the Lithophile Element-Bearing Magmatic-Hydrothermal System at Birch Creek, White Mountains, California: Society of Economic Geologists Guidebook Series, p. 9–26.

Bateman, P.C., 1992, Stratigraphic and Structural Setting , in Plutonism in the Central Part of the Sierra Nevada Batholith, California, Washington, U.S. G.P.O., p. 5–24.

Becker, S., Eichhubl, P., Laubach, S., Reed, R., Lander, R., and Bodnar, R., 2010, A 48 my history of fracture opening, temperature, and fluid pressure: Cretaceous Travis

Peak Formation, East Texas basin: Geological Society of America Bulletin, v. 122, no. 7-8, p. 1081-1093.

Bergerat, F., Bouroz-Weil, C., and Angelier, J., 1992, Palaeostresses inferred from macrofractures, Colorado Plateau, western USA: Tectonophysics, v. 206, no. 3, p. 219-243.

Bonnet, E., Bour, O., Odling, N. E., Davy, P., Main, I., Cowie, P., and Berkowitz, B., 2001, Scaling of fracture systems in geological media: Reviews of Geophysics, v. 39, no. 3, p. 347-383.

Bons, P.D., Elburg, M.A., and Gomez-Rivas, E., 2012, A review of the formation of tectonic veins and their microstructures: Journal of Structural Geology, v. 43, p. 33–62.

Bradley, W., Cantwell, W.J., Kausch, H.H., 1997. Viscoelastic Creep Crack Growth: A Review of Fracture Mechanical Analyses. Mechanics of Time-Dependent Materials 1, 241-268.

Brinson, H. F., 1970, The ductile fracture of polycarbonate: Experimental Mechanics, v. 10, no. 2, p. 72-77.

Broberg, K. B., 1999, Cracks and fracture, Academic Press., p. 236-246

Burchfiel, B.C., and Davis, G.A., 1975, Nature and controls of Cordilleran orogenesis, western United States: Extensions of an earlier synthesis: American Journal of Science, v. 275-A, p. 363–396.

Charles, R.J., 1958, Dynamic Fatigue of Glass: J. Appl. Phys. Journal of Applied Physics, v. 29, p. 1657.

Coleman, D.S., Briggs, S., Glazner, A.F., and Northrup, C., 2003, Timing of plutonism and deformation in the White Mountains of eastern California: Geological Society of America Bulletin, v. 115, p. 48–57.

Cooke, M. L., and Underwood, C. A., 2001, Fracture termination and step-over at bedding interfaces due to frictional slip and interface opening: Journal of Structural Geology, v. 23, no. 2–3, p. 223-238.

Corbett, K. P., Wrucke, C. T., and Nelson, C. A., 1988, Structure and tectonic history of the Last Chance thrust system, in Morgan, S.S., and Law, R.D., 1998, An Overview of Paleozoic-Mesozoic Structures Developed in the Central White-Inyo Range, Eastern California: International Geology Review, v. 40, p. 245–256.

Corte, A., and Higashi, A., 1964, Experimental research on desiccation cracks in soil.

Daneshy, A. A., 1973, A study of inclined hydraulic fractures: Society of Petroleum Engineers Journal, v. 13, no. 02, p. 61-68.

Davatzes, N. C., and Aydin, A., 2003, The formation of conjugate normal fault systems in folded sandstone by sequential jointing and shearing, Waterpocket monocline, Utah: Journal of Geophysical Research: Solid Earth, v. 108, no. B10, p. n/a-n/a.

Ding, Q.-L., Ju, F., Mao, X.-B., Ma, D., Yu, B.-Y., and Song, S.-B., 2016, Experimental Investigation of the Mechanical Behavior in Unloading Conditions of Sandstone After High-Temperature Treatment: Rock Mechanics and Rock Engineering, v. 49, no. 7, p. 2641-2653.

Delaney, P. T., and Pollard, D. D., 1981, Deformation of host rocks and flow of magma during growth of minette dikes and breccia-bearing intrusions near Ship Rock, New Mexico: USGPO, 2330-7102.

Delaney, P. T., Pollard, D. D., Ziony, J. I., and McKee, E. H., 1986, Field relations between dikes and joints: Emplacement processes and paleostress analysis: Journal of Geophysical Research: Solid Earth, v. 91, no. B5, p. 4920-4938.

Dugdale, D. S., 1960, Yielding of steel sheets containing slits: Journal of the Mechanics and Physics of Solids, v. 8, no. 2, p. 100-104.

Dunne, G.C., and Walker, J.D., 2004, Structure and evolution of the East Sierran thrust system, east central California: Tectonics, v. 23.

Eichhubl, P., 2004, Growth of ductile opening-mode fractures in geomaterials, in: Cosgrove, J. W., and Engelder, T. , eds., The Initiation, Propagation, and Arrest of Joints and Other Fractures: Interpretations based on Field Observations. Geological Society London Special Publication, vol. 231, p. 11-24. http://dx.doi.org/10.1144/GSL.SP.2004.231.01.02

Eichhubl, P., and Aydin, A., 2003, Ductile opening-mode fracture by pore growth and coalescence during combustion alteration of siliceous mudstone: Journal of Structural Geology, v. 25, no. 1, p. 121-134.

Eichhubl, P., Boles, J.R., 1998. Vein formation in relation to burial diagenesis in the Miocene Monterey Formation, Arroyo Burro Beach, Santa Barbara, California. In: Eichhubl. P. (Ed.), Diagenesis, Deformation, and Fluid Flow in the Miocene Monterey Formation of Coastal California. SEPM Pacific Section Special Publication 83, pp.15–36.

Ellis, M. A., Laubach, S. E., Eichhubl, P., Olson, J. E., and Hargrove, P., 2012, Fracture development and diagenesis of Torridon Group Applecross Formation, near An Teallach, NW Scotland: millennia of brittle deformation resilience?: Journal of the Geological Society, v. 169, no. 3, p. 297-310.

Engelder, T., Fischer, M.P., and Gross, M.R., 1993, Geological aspects of fracture mechanics: Boulder, Colorado, Geological Society of America.

Engelder, T., and Geiser, P., 1980, On the use of regional joint sets as trajectories of paleostress fields during the development of the Appalachian Plateau, New York: Journal of Geophysical Research: Solid Earth, v. 85, no. B11, p. 6319-6341.

Flodin, E., and Aydin, A., 2004, Faults with asymmetric damage zones in sandstone, Valley of Fire State Park, southern Nevada: Journal of Structural Geology, v. 26, no. 5, p. 983-988.

Fall, A., Eichhubl, P., Cumella, S. P., Bodnar, R. J., Laubach, S. E., and Becker, S. P., 2012, Testing the basin-centered gas accumulation model using fluid inclusion observations: Southern Piceance Basin, Colorado: AAPG bulletin, v. 96, no. 12, p. 2297-2318.

Gale, J. F. W., R. H. Lander, R. M. Reed, and S. E. Laubach, 2010, Modeling fracture porosity evolution in dolostone: Journal of Structural Geology, v. 32, p. 1201-1211.

Gale, J. F., Reed, R. M., and Holder, J., 2007, Natural fractures in the Barnett Shale and their importance for hydraulic fracture treatments: AAPG bulletin, v. 91, no. 4, p. 603-622.

Geertsma, J., and Klerk, F.D., 1969, A Rapid Method of Predicting Width and Extent of Hydraulically Induced Fractures: Journal of Petroleum Technology, v. 21, p. 1571–1581.

Goldstein, R. H., and T. J. Reynolds, 1994, Systematics of fluid inclusions in diagenetic minerals: SEPM (Society for Sedimentary Geology) Short Course 31, 199 p.

Goodier, J. N. & Field, F. A. 1963. Plastic energy dissipation in crack propagation. In: Vermilye, J.M., and Scholz, C.H., 1995, Relation between vein length and aperture: Journal of Structural Geology, v. 17, p. 423–434, doi: 10.1016/0191-8141(94)00058-8.

Gomez, L., 2007, Characterization of the Spatial Arrangement of Opening-Mode Fractures [Doctor of Philosophy: The University of Texas at Austin.

Griffith, A. A., 1921, The phenomena of rupture and flow in solids: Philosophical transactions of the royal society of london. Series A, containing papers of a mathematical or physical character, v. 221, p. 163-198.

Gudmundsson, A., 1987, Geometry, formation and development of tectonic fractures on the Reykjanes Peninsula, southwest Iceland: Tectonophysics, v. 139, p. 295–308, doi: 10.1016/0040-1951(87)90103-x.

Gudmundsson, A., 2011, Rock fractures in geological processes, Cambridge University Press.

Gudmundsson, A., Kusumoto, S., Simmenes, T.H., Philipp, S.L., Larsen, B., and Lotveit, I.F., 2012, Effects of overpressure variations on fracture apertures and fluid transport: Tectonophysics, v. 581, p. 220–230, doi: 10.1016/j.tecto.2012.05.003.

Guscott, S. C., and Burley, S. D., 1993, A systematic approach to reconstructing palaeofluid evolution from fluid inclusions in authigenic quartz overgrowths: Geofluids, v. 93, p. 323-328.

Helgeson, D. E., and Aydin, A., 1991, Characteristics of joint propagation across layer interfaces in sedimentary rocks: Journal of Structural Geology, v. 13, no. 8, p. 897-911.

Holland, M., and Urai, J. L., 2010, Evolution of anastomosing crack–seal vein networks in limestones: Insight from an exhumed high-pressure cell, Jabal Shams, Oman Mountains: Journal of Structural Geology, v. 32, no. 9, p. 1279-1290.

Hooker, J. N., Gale, J. F. W., Gomez, L. A., Laubach, S. E., Marrett, R., and Reed, R. M., 2009, Aperture-size scaling variations in a low-strain opening-mode fracture set, Cozzette Sandstone, Colorado: Journal of Structural Geology, v. 31, no. 7, p. 707-718.

Hooker, J. N., Laubach, S. E., and Marrett, R., 2013, Fracture-aperture size—frequency, spatial distribution, and growth processes in strata-bounded and non-strata-bounded fractures, Cambrian Mesón Group, NW Argentina: Journal of Structural Geology, v. 54, p. 54-71.

Ingraffea, A.R., 1989, Theory of crack initiation and propagation in rock, in Fracture mechanics of rock, London, Academic Press, p. 71–110.

Irwin, G. R., 1957, Analysis of stresses and strains near the end of a crack traversing a plate: Spie Milestone series MS, v. 137, no. 167-170, p. 16.

Jaeger, J.C., Cook, N.G.W., and Zimmerman, R.W., 2007, Fundamentals of rock mechanics: Malden, MA, Blackwell Pub.

Jin, Z. H., and Sun, C. T., 2005, Cohesive Fracture Model Based on Necking: International Journal of Fracture, v. 134, no. 2, p. 91-108.

Kanninen, M. F., and Popelar,, A., 1985, Advanced Fracture Mechanics, American Society of Mechanical Engineers.

Kanninen, M. F., Mukherjee, A. K., Rosenfield, A. R., and Hahn, G. T., 1969, The Speed of Ductile-Crack Propagation and the Dynamics of Flow in Metals, in Lindholm, U. S., ed., Mechanical Behavior of Materials under Dynamic Loads: Symposium Held in San Antonio, Texas, September 6-8, 1967: Berlin, Heidelberg, Springer Berlin Heidelberg, p. 96-133.

Karunaratne, B.S.B., and Lewis, M.H., 1980, High-temperature fracture and diffusional deformation mechanisms in Si-Al-O-N ceramics: J Mater Sci Journal of Materials Science, v. 15, p. 449–462.

Klimczak, C., Schultz, R.A., Parashar, R., and Reeves, D.M., 2010, Cubic law with aperture-length correlation: implications for network scale fluid flow: Hydrogeol J Hydrogeology Journal, v. 18, p. 851–862, doi: 10.1007/s10040-009-0572-6.

Knipe, R. J., 1977, The application of high voltage electron microscopy to the study of deformation mechanisms in low grade metamorphic rocks, Imperial College (University of London), London.

Knipe, R., 1989, Deformation mechanisms—recognition from natural tectonites: Journal of Structural Geology, v. 11, no. 1, p. 127-146.

Kusumoto, S., and Gudmundsson, A., 2014, Displacement and stress fields around rock fractures opened by irregular overpressure variations: Frontiers in Earth Science, v. 2, no. 7.

Kusumoto, S., Gudmundsson, A., Simmenes, T. H., Geshi, N., and Philipp, S. L., 2013, Inverse modeling for estimating fluid-overpressure distributions and stress intensity factors from an arbitrary open-fracture geometry: Journal of Structural Geology, v. 46, p. 92-98.

Lacazette, A., and Engelder, T., 1992, Chapter 12 Fluid-driven Cyclic Propagation of a Joint in the Ithaca Siltstone, Appalachian Basin, New York, in Brian, E., and Teng-fong, W., eds., International Geophysics, Volume Volume 51, Academic Press, p. 297-323.

Lander, R. H., and Laubach, S. E., 2014, Insights into rates of fracture growth and sealing from a model for quartz cementation in fractured sandstones: Geological Society of America Bulletin.

Laubach, S. E., R. H. Lander, L. M. Bonnell, J. E. Olson, and R. M. Reed, 2004a, Opening histories of fractures in sandstone: Geological Society, London, Special Publications, v. 231, p. 1-9.

Laubach, S. E., R. M. Reed, J. E. Olson, R. H. Lander, and L. M. Bonnell, 2004b, Coevolution of crack-seal texture and fracture porosity in sedimentary rocks: cathodoluminescence observations of regional fractures: Journal of Structural Geology, v. 26, p. 967-982.

Lawton, T.F., 1980, Petrography and structure of the Little Cottonwood stock and metamorphic aureole, central Wasatch Mountains, Utah [thesis].

Lloyd, G. E., and Knipe, R. J., 1992, Deformation mechanisms accommodating faulting of quartzite under upper crustal conditions: Journal of Structural Geology, v. 14, no. 2, p. 127-143.

McConaughy, D. T., and Engelder, T., 2001, Joint initiation in bedded clastic rocks: Journal of Structural Geology, v. 23, no. 2–3, p. 203-221.

McKee, E.H., and Conrad, J.E., 1996, A tale of 10 plutons—Revisited: Age of granitic rocks in the White Mountains, California and Nevada: Geological Society of America Bulletin, 108. 1515.

Meredith, P., and Atkinson, B., 1985, Fracture toughness and subcritical crack growth during high-temperature tensile deformation of Westerly granite and Black gabbro: Physics of the Earth and Planetary Interiors, v. 39, p. 33–51.

Michalske, T.A., and Freiman, S.W., 1982, A molecular interpretation of stress corrosion in silica: Nature, v. 295, p. 511–512.

Michalske, T.A., and Freiman, S.W., 1983, A Molecular Mechanism for Stress Corrosion in Vitreous Silica: Journal of the American Ceramic Society J American Ceramic Society, v. 66, p. 284–288.

Miller, J.S., 1996, Pb/U crystallization age of the Papoose Flat pluton, White-Inyo Mountains, California: Geological Society of America Abstracts with Programs, 28. 91.

Moore, J.N., and Fritsche, A.E., 1976, Depositional environments of Lower Paleozoic rocks in the White Inyo Mountains, Inyo County, California: (papers prepared for presentation at the 1976 Annual Fall field trip of the Pacific Section of the Society of economic paleontologists and mineralogists; Big Pine - Calif., October 16, 1976): Pacific coast paleogeography symposium 1, 1977): Los Angeles - Calif.

Morgan, S.S., and Law, R.D., 1998, An Overview of Paleozoic-Mesozoic Structures Developed in the Central White-Inyo Range, Eastern California: International Geology Review, v. 40, p. 245–256.

Myers, R., and Aydin, A., 2004, The evolution of faults formed by shearing across joint zones in sandstone: Journal of Structural Geology, v. 26, no. 5, p. 947-966.

National Research Council, 1996, Rock fractures and fluid flow: contemporary understanding and applications: Washington, D.C., National Academy Press, p.551

Nara, Y., Koike, K., Yoneda, T., and Kaneko, K., 2006, Relation between subcritical crack growth behavior and crack paths in granite: International Journal of Rock Mechanics and Mining Sciences, v. 43, p. 1256–1261.

Nelson, C.A., 1966, Geologic map of the Blanco Mountain quadrangle, Inyo and Mono counties, California: U.S. Geological Survey map

Nelson, C.A., and Durham, J.W., 1966, Guidebook for field trip to Precambrian-Cambrian succession White-Inyo Mountains, California: Los Angeles, University of California.

Nelson, C.A., Hall, C.A., and Ernst, W.G., 1991, Geologic of the White-Inyo Range, in Natural history of the White-Inyo Range, eastern California, Berkeley, University of California Press, p. 42–54.

Olson, J. E., 2003, Sublinear scaling of fracture aperture versus length: An exception or the rule?: Journal of Geophysical Research: Solid Earth, v. 108, no. B9, p. n/a-n/a.

Olson, J. E., 2007, Fracture aperture, length and pattern geometry development under biaxial loading: a numerical study with applications to natural, cross-jointed systems: Geological Society, London, Special Publications, v. 289, no. 1, p. 123-142.

Peacock, D. C. P., 2001, The temporal relationship between joints and faults: Journal of Structural Geology, v. 23, no. 2–3, p. 329-341.

Petit, J.-P., and Mattauer, M., 1995, Palaeostress superimposition deduced from mesoscale structures in limestone: the Matelles exposure, Languedoc, France: Journal of Structural Geology, v. 17, no. 2, p. 245-256.

Pollard, D.D. and Aydin, A.A., 1988, Progress in understanding jointing over the past century: Geological Society of America Bulletin, v. 100, p. 1181-1204.

Pollard, D.D., and Segall, P., 1987, Theoretical Displacements and Stresses near Fractures in Rock: With Applications to Faults, Joints, Veins, Dikes, and Solution Surfaces, in Fracture Mechanics of Rock, Academic Press geology series, San Diego, CA, Academic Press INC., p. 277–349.

Riedel, H., 1987, Fracture at high temperatures, Springer, 6-8 p.

Ramsay, J. G., 1980, The Crack-Seal Mechanism of Rock Deformation: Nature, v. 284, p. 135-139.

Ramsay, J. G. & Huber, M. I. 1987. The Techniques of Modern Structural Geology, Volume 2: Folds and Fractures. Academic Press, London. In Lloyd, G. E., and Knipe, R. J., 1992, Deformation mechanisms accommodating faulting of quartzite under upper crustal conditions: Journal of Structural Geology, v. 14, no. 2, p. 127-143.

Rutter, E., and Elliott, D., 1976, The kinetics of rock deformation by pressure solution [and discussion]: Philosophical Transactions of the Royal Society of London A: Mathematical, Physical and Engineering Sciences, v. 283, no. 1312, p. 203-219.

Sakaguchi, K., Tomono, J., Okumura, K., Ogawa, Y., and Matsuki, K., 2008, Asperity Height and Aperture of an Artificial Tensile Fracture of Metric Size: Rock Mechanics and Rock Engineering, v. 41, no. 2, p. 325-341.

Savalli, L., and Engelder, T., 2005, Mechanisms controlling rupture shape during subcritical growth of joints in layered rocks: Geological Society of America Bulletin, v. 117, no. 3-4, p. 436-449.

Schaeffer, B. J., Liu, H. W., and Ke, J. S., 1971, Deformation and the strip necking zone in a cracked steel sheet: Experimental Mechanics, v. 11, no. 4, p. 172-175.

Shen, B., Stephansson, O., Einstein, H. H., and Ghahreman, B., 1995, Coalescence of fractures under shear stresses in experiments: Journal of Geophysical Research-All Series-, v. 100, p. 5975-5975.

Shimizu, I., 1995, Kinetics of pressure solution creep in quartz: theoretical considerations: Tectonophysics, v. 245, no. 3, p. 121-134.

Sibson, R.H., 1998, Brittle failure mode plots for compressional and extensional tectonic regimes: Journal of Structural Geology, v. 20, p. 655–660.

Signor, P.W., Mount, J.F., and Onken, B.R., 1987, A Pre-Trilobite Shelly Fauna from the White-Inyo Region of Eastern California and Western Nevada: Journal of Paleontology, v. 61, p. 425–438.

Sneddon, I.N., 1946, The Distribution of Stress in the Neighbourhood of a Crack in an Elastic Solid: Proceedings of the Royal Society A: Mathematical, Physical and Engineering Sciences, v. 187, p. 229–260, doi: 10.1098/rspa.1946.0077.

Snow, D. T., 1970, The frequency and apertures of fractures in rock, in Proceedings International journal of Rock mechanics and Mining sciences & Geomechanics Abstracts, Volume 7, Elsevier, p. 23-40.

Snow, J.K., and Wernicke, B.P., 2000, Cenozoic tectonism in the central Basin and Range: Magnitude, rate, and distribution of upper crustal strain: American Journal of Science, v. 300, p. 659–719.

Stevens, C.H., and Greene, D.C., 1999, Stratigraphy, depositional history, and tectonic evolution of Paleozoic continental-margin rocks in roof pendants of the eastern Sierra Nevada, California: Geological Society of America Bulletin, v. 111, p. 919–933.

Stevens, C.H., Stone, P., Dunne, G.C., Greene, D.C., Walker, J.D., and Swanson, B.J., 1997, Paleozoic and Mesozoic Evolution of East-Central California: International Geology Review, v. 39, p. 788–829.

Stevens, C.H., and Stone, P., 2002, Correlation of Permian and Triassic deformations in the western Great Basin and eastern Sierra Nevada: Evidence from the northern Inyo Mountains near Tinemaha Reservoir, east-central California: Geological Society of America Bulletin, v. 114, p. 1210–1221.

Stockli, D.F., Dumitru, T.A., Mcwilliams, M.O., and Farley, K.A., 2003, Cenozoic tectonic evolution of the White Mountains, California and Nevada: Geological Society of America Bulletin, v. 115, p. 788–816.

Sun, C. T., and Jin, Z. H., 2012, Chapter 7 - Elastic-Plastic Fracture Criteria, Fracture Mechanics: Boston, Academic Press, p. 171-187.

Swain, M., and Hagan, J., 1978, Some observations of overlapping interacting cracks: Engineering Fracture Mechanics, v. 10, no. 2, p. 299-304.

Tian, H., Kempka, T., Yu, S., and Ziegler, M., 2016, Mechanical Properties of Sandstones Exposed to High Temperature: Rock Mechanics and Rock Engineering, v. 49, no. 1, p. 321-327.

Tsang, Y.W., and Witherspoon, P.A., 1981, Hydromechanical behavior of a deformable rock fracture subject to normal stress: J. Geophys. Res. Journal of Geophysical Research: Solid Earth, v. 86, p. 9287–9298, doi: 10.1029/jb086ib10p09287.

Twiss, R.J., and Moores, E.M., 2007, Structural geology: New York, NY, W.H. Freeman. 38 p.

Ukar, E., and Laubach, S. E., Syn- and postkinematic cement textures in fractured carbonate rocks: Insights from advanced cathodoluminescence imaging: Tectonophysics.

Vermilye, J.M., and Scholz, C.H., 1995, Relation between vein length and aperture: Journal of Structural Geology, v. 17, p. 423–434, doi: 10.1016/0191-8141(94)00058-8.

Walsh, J., 1981, Effect of pore pressure and confining pressure on fracture permeability: International Journal of Rock Mechanics and Mining Sciences & Geomechanics Abstracts, v. 18, p. 429–435, doi: 10.1016/0148-9062(81)90006-1.

Wei, R.P.-ying, 2010, Fracture mechanics: integration of mechanics, materials science, and chemistry: Cambridge, Cambridge University Press. 14-16 p.

Weinberger, R., 2001, Joint nucleation in layered rocks with non-uniform distribution of cavities: Journal of Structural Geology, v. 23, no. 8, p. 1241-1254.

Weisstein, Eric W., 2016, "Lamé Curve." From MathWorld--A Wolfram Web Resource. http://mathworld.wolfram.com/LameCurve.html

Welch, T.C., 2000, The structural setting and significance of the Poleta Canyon thrust in the White Mtns., Inyo Co., eastern California: Geological Society of America Abstracts with Programs, 32 A-. 232. In Coleman, D.S., Briggs, S., Glazner, A.F., and Northrup, C., 2003, Timing of plutonism and deformation in the White Mountains of eastern California: Geological Society of America Bulletin, v. 115, p. 48–57.

Wells, A. A., Unstable crack propagation in metals: cleavage and fast fracture, in Proceedings Proceedings of the crack propagation symposium, 1961, Volume 1.

Yukutake, H., 1992, Fracture nucleation process in intact rocks: Tectonophysics, v. 211, no. 1, p. 247-257.

Zoback, M.D., 2010, Reservoir geomechanics / Mark D. Zoback: Cambridge, Cambridge University Press.

Vita

Natchanan Doungkaew grew up in a small town in the rural area of Uttaradit, Thailand. She was awarded and has been receiving the Royal Thai Government's Development and Promotion of Science and Technology Talents Project (DPST) scholarship since she was 15. During her last year of high school, she applied for another scholarship to pursue her bachelor's and doctoral degree in the United States, and was selected as one of the two scholars from hundreds of students. Her research interest lies in computer science and field geology, which led her to do internships in structural geology at Thailand's Department of Mineral Resources, and in seismology at Chiang Mai Seismic Center, the largest seismic center in Thailand, in the summer before her junior year. She pursued her interest in computational work further when she participated in Stanford University's SURGE program in the next summer, where she learned how to create an attenuation map of Yellowstone from ambient seismic noise. She graduated from Wesleyan University with honors for her senior thesis.

Natchanan was accepted to the Jackson School of Geosciences (JSG) graduate program at the University of Texas at Austin as part of the Fracture Research and Application Consortium (FRAC) at the Bureau of Economic Geology. She presented her work at the Annual FRAC Conference, the American Geophysical Union Annual Convention, and the JSG Annual Research Symposium. She received Ronald K. DeFord Field Scholarships and the GSA Graduate Student Research Grant during her graduate school career.

Permanent email: natchd@utexas.edu

This thesis was typed by the author